Chem. Rev. **2002,** *102,* 679–725

Ordered Anion Adlayers on Metal Electrode Surfaces

O. M. Magnussen*

Abteilung Oberflächenchemie und Katalyse, Universität Ulm, 89069 Ulm, Germany

Received May 18, 2001

Contents

I. Introduction

In this paper the structure and phase behavior of anion adlayers at the metal−electrolyte interface and their influence on the metal substrate structure and on electrochemical reactions are reviewed. The interface between a metal and an electrolyte solution is characterized by the presence of an electric double layer formed by an electronic charge on the metal surface and an opposite ionic charge in the adjacent solution. Ionic species with strongly bound solvation shells, such as most cations, F^-, ClO_4^-, and PF_6^-, interact with the electrode surface by purely electrostatic forces, and consequently, the excess ion surface concentration at a given electrode potential is independent of the chemical nature of the ionic species. In contrast, weakly solvated ions, e.g., SO_4^{2-}, Cl^-, Br^-, I^- and most other anions, can strip part of their solvation shell and form a direct chemical bond with the metal surface, resulting in an ionic surface concentration that exceeds that given by pure electrostatic interactions. This effect was first observed in early studies of the electrochemical double layer on Hg electrodes[1,2] and is generally known as specific adsorption. The surface coverage of specifically adsorbed ions can be considerably larger than in the case of nonspecific adsorption, where the

Olaf M. Magnussen was born in Niebüll, Germany, in 1963. He received a diploma in physics from Ludwig-Maximilians-University, Munich, in 1989 and his Ph.D. from University Ulm in 1993, where he studied electrochemical systems by in situ scanning tunneling microscopy in the surface chemistry group of Prof. R. J. Behm. From 1993 to 1995 he was a postdoctoral fellow at Brookhaven National Laboratory with Dr. B. M. Ocko, where he worked on synchrotron X-ray scattering studies of solid–liquid interfaces and free liquid surfaces. He returned to the group of Prof. Behm in 1996 as a research assistant and obtained his habilitation in 2000. In 2001 he joined the Physics Department of University Kiel as a full Professor. His research interests include surface electrochemisty, electrochemical deposition and nanostructure formation, corrosion and corrosion inhibition, electrocatalysis, surface phase transitions, and dynamic phenomena at interfaces.

---

* New adress: Institut für Experimentelle und Angewandte Physik, Universität Kiel, Olshausenstrasse 40, 24098 Kiel, Germany.

10.1021/cr000069p CCC: $39.75

coverage is typically below 0.1−0.2 monolayer (ML). As a result, specifically adsorbed anion species can form close-packed, ordered adlayer structures on electrode surfaces, which are the major topic of this review.

It has been realized for a long time that the presence of specifically adsorbed anions can significantly affect the electrochemical reactivity of a metal electrode, a phenomenon of considerable practical implications in galvanic deposition, etching, corrosion science, and electrocatalysis. The most obvious effect—the direct participation of the anions in the electrode reaction—occurs, for example, in the electrochemical deposition and dissolution of metals in the presence of anions that form complexes with the metal ions.[3] In this case the deposition/dissolution reaction typically involves the formation of an adsorbed intermediate, which can have pronounced influence on the reaction kinetics even in the case of weak complexing interactions. Furthermore, even if the strongly chemisorbed anions are confined to a single (preadsorbed) monolayer on the electrode surface and not present in the bulk electrolyte, they may significantly influence continuous faradayic reactions, as demonstrated for the iodine-catalyzed dissolution of Pd in halide-free electrolyte.[4−6] On the other hand, the reverse effect can occur, namely, a blocking of reaction sites by specifically adsorbed anions, resulting in a reduced reaction rate. Examples for this effect are the inhibition of Fe dissolution by halides[7,8] and the effect of halides and sulfate on the oxygen reduction on Pt and Au.[9−15] In addition, as already noted by Frumkin,[16] the presence of specifically adsorbed species alters the potential distribution in the double layer, which also affects the kinetics of electrochemical reactions. In general, all these effects were—in particular in the case of solid electrodes—understood only qualitatively and phenomenologically. Detailed data on the anion adlayer structure and its influence on the electrochemical reactivity are therefore of central importance to clarify the underlying microscopic mechanisms of these reactions.

Early studies of the specific adsorption of anions focused on thermodynamic data obtained from electrochemical and surface tension measurements on liquid Hg electrodes.[1,2,17,18] Since the specific adsorption of anions on Hg is particularly weak, the anion surface densities are considerably below saturation in the entire double layer potential range. Hence, for a long time the prevalent picture of electrochemical interfaces involved a disordered anion adlayer of partly hydrated species. Similar electrochemical studies on solid (usually polycrystalline) metal electrodes were originally hampered by several experimental and conceptual problems, of which the most significantly were the heterogeneity of these surfaces, the lack of structural characterization, and contamination problems. Extensive double layer studies on high-quality single crystal electrodes by cyclic voltammetry and capacitance measurements started to emerge only around 1970 (see ref 19 and references therein). These studies revealed a typically much stronger specific adsorption of anions as on liquid Hg, suggesting that high-density anion adlayers are likely on most metals. In particular, voltammograms of well-defined electrodes in electrolytes containing specifically adsorbing anions revealed sharp spikes, which were interpreted as phase transitions in the anion adlayer.[20−22] As an example, a cyclic voltammogram of Au(111) in sulfuric acid solution is shown in Figure 1, where spikes at 0.75 V (D3/D3′), corresponding to the formation of an ordered sulfate adlayer, are visible (the broader peaks D1/D1′ at 0.25 V and D2/D2′ around 0.45 V correspond to the anion-induced lifting of the Au surface reconstruction and sulfate adsorption, respectively). The extensive electrochemical data and classical and modern models of the electric double layer were described in detail in previous reviews.[19,23−25]

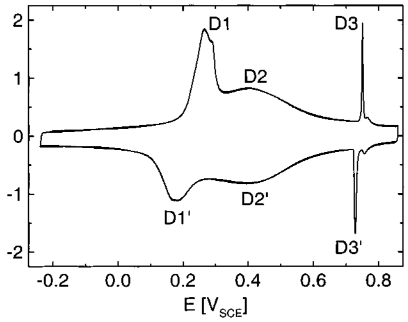

Figure 1. Cyclic voltammogram of Au(111) in 100 mM H_2SO_4 solution (potential sweep rate 10 mV/s). The sharp current spikes at 0.75 V (D3/D3′) indicate a phase transition in the sulfate adlayer.

Direct studies of the microscopic structure of electrochemical interfaces were for a long time severely limited by the lack of suitable, surface sensitive techniques, which mostly require vacuum conditions. Consequently, structural data on the electric double layer were first obtained in ex situ experiments, where the electrode was emersed in a controlled way from the electrolyte and then studied under ultrahigh vacuum (UHV) conditions using electron diffraction and photoemission techniques.[26−30] In studies of strongly specific adsorbing anions, various ordered adsorbate superstructures were observed by this method, with the structure and anion coverage depending on the emersion potential.[29] Although ex situ measurements continue to be a valuable tool for the study of strongly bound anions, they are more difficult to apply to weakly adsorbed species such as sulfate or chloride, where improper emersion may cause serious artifacts.[30,31]

Over the past decade the results of novel experimental and theoretical methods have begun to reshape our picture of anion adsorption. A major contribution has come from in situ structure sensitive techniques, in particular, scanning probe microscopy and X-ray scattering and spectroscopy using synchrotron radiation, which allow direct studies of the electrochemical interface on the atomic and nanometer scale. These methods not only provided detailed data on the structure of ordered anion adlayers as a function of the potential, but also revealed anion-induced changes in the electrode substrate structure and the influence of anions on surface dynamics and reactivity. In addition, the adsorption geometry of molecular adsorbates and the changes in the electronic properties of metal electrodes induced by anion adsorption have been extensively studied by established and novel in situ spectroscopic techniques. These results by structure sensitive probes have been supplemented by adsorption isotherms and detailed thermodynamic data for single crystalline surfaces, obtained by traditional electrochemical, radiochemical, and microgravimetric methods. Finally, considerable progress has also been made in the theoretical description and computer simulations of the electrochemical interface, including anion adsorption. From these different, synergetic approaches, a detailed picture of the complex interface structure in the presence of specifically adsorbing anions and its role in electrochemical reactions is emerging.

Although a detailed description of modern techniques for studying electrochemical interfaces is beyond the scope of this review, it is important to assess the advantages and limitations of the individual techniques in the study of anion adsorption. This review will therefore begin with a brief evaluation of the employed methods. Then the structure and phase behavior of specifically adsorbed anion adlayers on solid metal surfaces will be described, with particular emphasis on the ordered structures formed in the regime of high surface coverages. Here we will first discuss halide adlayers, the simplest type of anion species, starting with an analysis of the thermodynamic data and chemical interactions in the adlayer. Then an overview on the current structural data on ordered halide adlayers will be given to outline some general effects and trends. Using selected examples of structures and structural phase transitions in halide adlayers it will be shown how the observed adlayer structures can be understood as a result of the competing adsorbate–adsorbate and adsorbate–substrate interactions. In addition, the close correspondence between adlayers formed by electrochemical halide adsorption and by gas phase adsorption of halogens will be demonstrated. Subsequently, adlayers formed by other simple anions will be discussed, namely, sulfide and hydroxide; the pseudohalides cyanide and thiocyanide, where the observed structures closely resemble those of the halides; and the oxyanion sulfate, which exhibits a more complex adlayer structure. Strong specific adsorption involves the presence of an excess surface concentration of counterions, which can result in the formation of ordered, mixed layers of anions and cations, an effect that is also briefly discussed. We then turn our attention to the influence of anions on the surface structure and reactivity of metal electrodes. Here first examples of anion-induced reconstruction and surface restructuring processes are presented before finally the influence of ordered anion adlayers on the mechanisms and dynamics of bulk metal deposition and dissolution, organic adsorption, electrocatalytic reactions, and outer-sphere electron-transfer reactions is described. The paper concludes with an outlook on the future prospects and remaining challenges in the study of specific anion adsorption.

II. Experimental Methods

A. Scanning Probe Microscopies

Scanning tunneling microscopy (STM) and atomic force microscopy (AFM) have become highly popular over the last 2 decades due to their ability to directly resolve the local surface structure and morphology with up to atomic resolution. The application of these techniques for in situ studies of electrochemical interfaces has been extensively described in several reviews[32-36] and will only be briefly treated here, with an emphasis on the study of anion adlayers. Indeed, the in situ observation of an ordered iodine adlayer on Pt(111) by Yau et al.[37] was one of the first examples of atomic resolution imaging in an electrochemical environment and has considerably promoted the interest of the electrochemical community in scanning probe methods. In addition to providing in situ data on the adlayer lattice structure, the local character and high resolution of these techniques offer the opportunity to study the defect structure of adlattice and substrate, e.g., domain boundaries, vacancies, and steps, which often gives considerable insight into the adsorption geometry and interactions within the adlayer. Furthermore, time-resolved measurements allow investigations of dynamic processes, such as phase transitions, equilibrium fluctuations, or local surface reactions. The unique possibility to study the local structure and reactivity with up to atomic resolution has significantly contributed to the popularity of in situ scanning probe techniques.

For a realistic assessment of the data obtained, however, the limitations of STM/AFM should not be overlooked. First, due to thermal drift effects and calibration errors, the experimental errors in lattice distances and angles measured in high-resolution STM and AFM images are usually a few tenths of an angstrom and a few degrees, respectively. An exact determination of the structure of high-order commensurate or incommensurate adlattices is therefore often difficult. A higher precision can be obtained (i) by direct subsequent imaging of both adlattice and substrate, either via potential-induced desorption of the adsorbate[38,39] or via variation of the tunneling parameters,[31,37,40-43] or (ii) for high-order commensurate or incommensurate structures by analysis of the Moiré pattern resulting from the mismatch of adsorbate and substrate lattice.[44-46] Second, due to the small area probed in the measurements, reproducibility and statistical relevance are of major importance, in particular since coexistence of different structural phases is possible for strongly bound adsorbates.[47,48] Third, in the interpretation of high-resolution STM data, one should be aware that—in contrast to AFM—STM does not probe the position of the ion cores but the electronic structure. Hence, the bumps and shapes visible in the STM image or, even more, their apparent heights do not necessarily reflect the actual atomic positions, in particular for molecular adsorbates and coadsorbate structures. Detailed experimental studies under UHV conditions as well as theoretical approaches have shown that contributions to the STM images come from the adsorbate as well as the underlying substrate, both perturbed by their mutual interaction.[49,50] In addition, the images can be substantially influenced by the geometric and electronic structure of the STM tip. The complex structures at electrochemical interfaces can therefore not be reliably determined by STM alone, but complementary techniques are required.

B. X-ray Scattering and Spectroscopy

High-precision structural data on electrochemically adsorbed adlayers can be obtained by in situ surface X-ray scattering (SXS) and X-ray spectroscopy studies using synchrotron radiation.[51−54] To minimize adsorption losses, these measurements are usually performed in a thin-layer geometry, where the electrolyte thickness is confined to several microns by a thin plastic window. Particularly fruitful for elucidating the structure and phase behavior of ordered adlayers on electrode surfaces have been X-ray diffraction measurements under grazing incident angles (GIXD), which allow determination of the lattice parameters with picometer precision and, via quantitative analysis of peak intensities and peak widths, provide data on adsorption sites and average domain sizes. In addition, the surface normal structure of ordered as well as disordered adlayers, e.g., the average adsorbate density, the distance between ad- and surface layer, and the influence of the adsorbate on the substrate lattice spacing, can be probed in the same experiment via measurements of the specular and the nonspecular crystal truncation rods of the substrate. Due to its unsurpassed precision and quality, the structural information obtained by in situ X-ray scattering techniques will be preferentially used in the discussion of the structure of close-packed anion adlayers. Unfortunately, SXS measurements of adsorbates with low atomic number Z are severely hampered by the Z^2 dependence of the scattered intensity and the high background, resulting from scattering at the bulk electrolyte and the plastic window. The lowest Z anion adsorbate where an ordered adlayer structure has been observed up to now by GIXD is Cl[55] (with a signal-to-background ratio of 1:4 for first-order peaks); attempts to obtain diffraction peaks for an ordered sulfate adlayer of known structure were unsuccessful.[56]

In situ structural data on adsorbate−adsorbate and adsorbate−substrate bond lengths can in principle be obtained also by X-ray spectroscopy, such as surface extended X-ray absorption fine structure (EXAFS)[57] or X-ray standing wave (XSW) techniques,[58] which are based on changes in the X-ray absorption or fluorescence due to electronic interference effects between neighboring atoms (EXAFS) or spatial modulations of the X-ray field intensity at the interface (XSW). These methods were frequently employed for the study of halogen adlayers under UHV conditions. Studies of electrochemical interfaces, however, have been largely limited to metal deposits and oxides and—with a single exception[59]—only in this context were data on anion (co)adsorption obtained.[57,60−62] This is related to problems with the position of the relevant adsorption edges and background caused by the bulk electrolyte.

C. Optical Spectroscopy

Spectroscopic methods, such as electroreflectance, ellipsometry, and Raman spectroscopy, belong to the oldest and most established in situ techniques. In particular, they probe the electronic structure and hence provide insight into the chemical bond between adsorbate and substrate. The latter also holds true for infrared adsorption spectroscopy, the most widely used in situ optical spectroscopic method.[63−65] IR spectroscopy has been especially useful for studies of molecular adsorbates, i.e., in the case of anionic adsorbates cyanide, thiocyanide, and oxyanions, where it can provide data on the local adsorption geometry. Conventionally, these studies are performed in thin-layer geometry, using difference or modulation techniques to remove the contributions of the bulk electrolyte. Higher sensitivity and even a surface-enhancement effect can be obtained in attenuated total reflection (ATR) experiments,[66] although the interpretation of these data for metal (thin-film) electrodes is still under debate (see section IV.C).

More recently, the nonlinear optical methods of second harmonic generation (SHG) and sum frequency generation (SFG) have been applied to electrochemical interfaces.[67] These methods are intrinsically surface-sensitive and hence well-suited for in situ studies. SHG gives data on the electronic structure and symmetry of the electrode surface, but the interpretation relies heavily on theory. SFG allows vibrational spectroscopy of adsorbates at electrochemical interfaces; however, up to now it has not been employed heavily due to the rather demanding experimental setup. Nevertheless, the first SHG data on anion adlayers were recently reported.[68−74]

D. Macroscopic Measurements

Important complementary results come from traditional electrochemical studies on single-crystal electrodes, e.g., by chronocoulometry or potential step experiments, which provide detailed thermodynamic and kinetic data on anion adsorption. Similar data can be obtained by several other in situ techniques that measure changes in macroscopic properties associated with anion adsorption. For example, radioactive labeling techniques[75] have been used to obtain adsorption isotherms as well as information on dynamic effects, such as the exchange between adlayer and solution, and mass changes due to adsorption processes have been measured by electrochemical quartz crystal microbalance.[76−78] All these techniques have in common that they measure integral properties, such as the total surface excess of the chemisorbed species, and hence are insensitive to the adlayer structure.

E. Studies under UHV Conditions

As already mentioned, studies of anion adlayers under UHV conditions are an attractive alternative due to the great variety of available surface-sensitive techniques. Two different approaches are possible: First, UHV techniques can be used for ex situ studies of emersed electrodes.[27−30] Despite the problems with the transfer of weakly bound adsorbates mentioned above, these measurements still provide important insight into structure, chemical composition, and electronic properties of anion adlayers, especially if complemented by in situ studies. Second, the electrochemical double layer can be simulated by preparing well-defined adlayers via gas-phase dosing of ions and solvent species on clean metal surfaces.[79−82] It has been demonstrated that the adlayers prepared by this method closely reflect the inner part of the electrochemical double layer. For close-packed adlayers of strongly bound adsorbates such as halides, where the solvent is largely expelled from the metal surface, even gas-phase dosing of the anion species (e.g., halogens) alone, i.e., without solvent codosing, leads to similar structures as those found in in situ electrochemical studies (see below), suggesting a close similarity of the adlayer energetics in both environment.

F. Theory and Simulation

Theoretical studies of specifically adsorbed anions have focused on halide adsorption at metal surfaces, using various theoretical methods. The halide−metal interaction was studied by cluster model calculations, employing first semiempirical and, more recently, ab initio quantum chemical methods, such as Hartree−Fock or density functional theory (see refs 25 and 83−88 and references therein). These studies generally neglect solvation effects, adsorbate−adsorbate interactions, and metal surface charge and hence most precisely describe the situation at the metal−vacuum interface in the zero-coverage limit. Nevertheless, they provide valuable data on the nature of the chemical bond between adsorbate and substrate atoms and on qualitative chemical trends. An alternative approach is to model the electrochemical interface by computer simulation techniques. Modeling of the role of the solvent is possible by molecular dynamics simulations, which allow the study of the ion and solvent distribution near the interface.[89−96] Here the major problems are associated with the construction of the ion−metal interaction potentials from quantum chemical calculations. In addition, phase transitions in adlayers on electrode surfaces have been studied by statistical models[97,98] and Monte Carlo simulations.[99−101]

III. Halide Adlayers

A. Thermodynamics

Halides are by far the most extensively studied class of specifically adsorbed anions. This is not only due to the structural simplicity of these monatomic, monovalent anions but also due to their abundance in natural and technological environments. The degree of specific adsorption increases in the order $F^- < Cl^- < Br^- < I^-$, reflecting the decreasing energy of solvation of these species,[18] with F^- being nonspecifically or only weakly specifically adsorbed. This is illustrated in Figure 2, using the results of a detailed chronocoulometric study by Lipkowski et al. on the energetics of halides and sulfate on Au(111).[102] Clearly, both the Gibbs free energy of adsorption ΔG (Figure 2c) and the anion surface concentration Γ (Figure 2b) increase in this order at any given potential. The adsorption isotherms, which were also supported by electrochemical quartz microbalance studies,[78] exhibit three different regimes, characterized by different slopes in the $\Gamma(E)$ and $\Delta G(E)$ curves. Specific anion adsorption starts on the negatively charged surface, where the anion surface concentration changes only slowly with potential. At potentials slightly positive of the potential of zero charge (pzc), a steep rise in $\Gamma(E)$ is observed, followed by a third regime of slow increase, where the adlayer packing

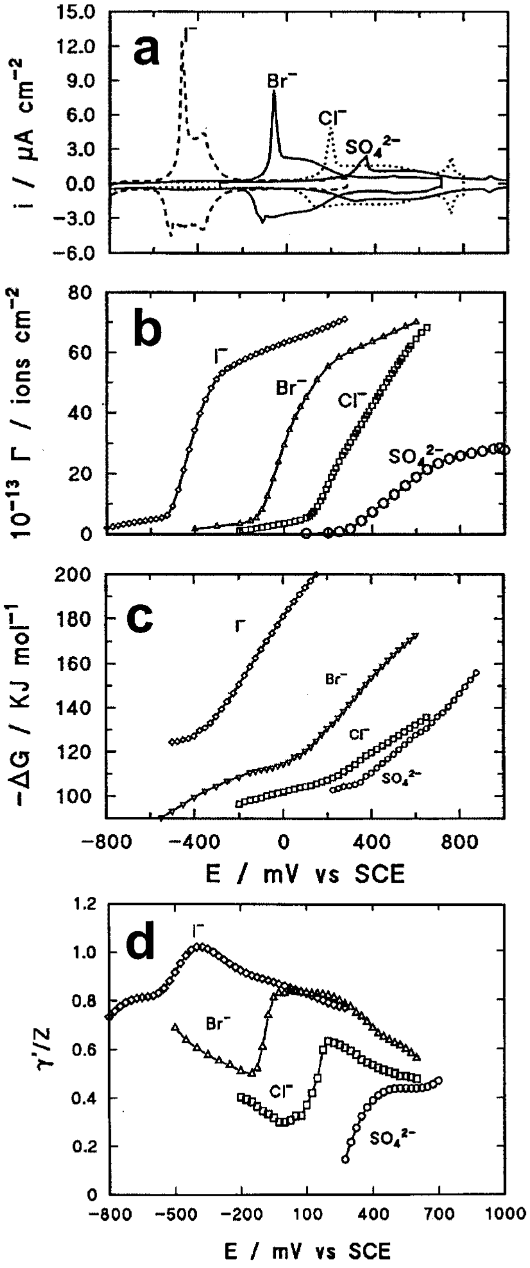

Figure 2. Electrochemical and thermodynamic data on halide and sulfate adsorption on Au(111) obtained by chronocoulometry. (a) Cyclic voltammograms, (b) excess surface concentration, (c) Gibbs energy of adsorption (standard state: $\Gamma = 1$ ion cm^{-2} and $c = 1$ mol dm^{-3} for surface and bulk species, respectively), and (d) electrosorption valencies as a function of potential. (Reprinted with permission from ref 102. Copyright 1998 Elsevier Science Ltd.)

densities are close to saturation. As will be shown below, ordered adlayer structures are formed in this high-coverage regime. For Au(111), the pronounced increase in slope at anion surface concentrations of about 8×10^{-13} cm^{-2}, which also manifests in pronounced peaks in the corresponding cyclic voltammograms (Figure 2a), is accompanied by lifting of the Au reconstruction.[103-111] This change in the substrate structure results in a small cathodic shift of the pzc,[103,109] which may further contribute to the high slope in this potential range. The general shape of this curve, however, is found also for other (unreconstructed) substrates, as shown by similar studies on Ag(111) by Foresti et al.,[112] Ag(100) by Wandlowski et al.,[113] and Pt(111) by Li and Lipkowski.[114]

The formation of a chemical bond during specific adsorption obviously involves a redistribution of the electronic charge from the anion toward the electrode surface, an effect known as partial charge transfer.[115] A more precise definition in quantum mechanical terms is to associate the partial charge with the amount of filling of the orbital resonances of the adsorbate.[116] Frequently, the electrosorption valency, $\gamma = -1/F(\partial\sigma_M/\partial\Gamma)_E = 1/F(\partial\mu/\partial E)_\Gamma$, i.e., the flow of charge σ_M to the electrode per adsorbed ion at constant electrode potential E, has been employed as a measure of partial charge.[117,118] However, the electrosorption valency is a thermodynamic quantity and, hence, only measures the amount of charge uptake, but not its microscopic distribution in the interface region.[119] In fact, γ can correspond equally well to a discharge of the ion or to an additional opposite charge on the metal to screen the ionic charge. For this reason little information can be gained on the nature of the anion−metal bond from electrochemical measurements alone (for a recent discussion, see also refs 102 and 119). A simple model to disentangle the various contributions to γ, based on comparison with known chemical and geometrical parameters of the adsorbate and solvent species, was suggested in the early work by Schultze et al.[117,119,120] The electrosorption valencies for halides and sulfate on Au(111) (Figure 2d)[102] show a pronounced potential dependence, which again reflects that of the adsorption isotherms: γ is low in the low-coverage regime negative of the pzc, approaches a maximum in the range of strongly increasing anion coverage, and slowly decays again in the range of saturation coverages. It is noted that the absolute values of the electrosorption valency slightly depend on the employed method, although the general potential dependence is similar.[112,121] Interestingly, a quite different behavior is found if the electrosorption valencies are calculated not from electrochemical data but from the local coverages θ in the ordered adlayer phases, obtained from in situ structure-sensitive techniques. Here the adsorption isotherms for halides on Au and Ag electrodes always shift by ≈60 mV per decade of halide bulk concentration (see below),[46,55,56,122,123] corresponding to an electrosorption valency close to 1, independent of halide species and potential. This suggests that the halide anions in the ordered adlayer are to a large extent discharged. In addition, also the surface concentrations measured by chronocoulometry are usually 5−15% higher than those calculated from the structural data. The latter is usually attributed to an increase in the real electrode surface area in the coulometric experiments due to surface roughness, which, however, cannot explain the difference in electrosorption valency. An alternative explanation, which could account for both of these discrepancies between the electrochemical and the structural data, might be the coexistence of the chemisorbed (largely discharged) halides in the ordered adlayer with a second, predominantly electrostatically bound (i.e., charged) halide species. Due to the high anion density in the ordered adlayer phases, this second type of halide would have to reside at defects or on top of the ordered layer. Indeed, X-ray reflectivity measurements of Au(111)−I by Ocko et al. are supportive of a second iodide adlayer with a coverage that is about 5% of that in the underlying ordered layer.[122]

The changes in the electrosorption valency can be interpreted in terms of the adsorbate-induced surface dipole formed due to the polarity of the adsorbate−metal bond.[116] This treatment is completely analogous to the calculation of the surface dipole of an adsorbate at the solid−vacuum interface from the induced change in work function. The advantage of this approach is that it does not require assumptions on the charge distribution at the interface and allows a direct comparison of halide adlayers in both environments. In general, the dipole moments obtained for electrochemically adsorbed species are smaller than in UHV, due to the contribution of the solvent dipole moments, which tend to orient in the opposite direction. Since this solvent effect depends on the degree of hydration, these differences should be largest around the pzc, but less pronounced in the high coverage regime, where the solvent is largely expelled from the surface. Indeed, the surface dipole moments of −0.3 D for Cl^- and −0.25 D for Br^- obtained by Lipkowski et al. in the range of saturation coverages[102,121] are only slightly smaller than those obtained for ordered halogen adlayers on Au in UHV (−0.33 D for Cl^- [124] and −0.30 D for Br^- [125]). The similar polarity of the surface bond in the close-packed adlayers at the solid−electrolyte and solid−vacuum interface suggests that also the interactions, which govern the adlayer structure, should be similar. This is supported by the close agreement of the adlayer structure in both environments (see below). In contrast, an order of magnitude smaller electrochemical surface dipoles are found close to the pzc, where the solvent contribution is expected to be dominant. The effect of solvation on the surface dipole as well as the close relationship between work function shift and potential drop in the inner double layer was explicitly shown in a combined UHV and electrochemical study by Sass et al.[79-81] (for a detailed discussion, see also refs 24 and 82).

B. Halide–Metal Interactions

More direct information on the interactions between chemisorbed halides or halogens and the metal substrate can be obtained from the results of structure-sensitive and spectroscopic techniques. The halide−metal bond lengths in the ordered adlayer phases were studied by EXAFS, XSW, and LEED under UHV conditions[126−139] and by in situ X-ray reflectivity measurements[108,122,140−142] and in situ EXAFS[59] for electrochemically adsorbed adlayers. Usually distances close to the sum of the covalent radius of the halide and the metallic radius of the substrate atoms were found, indicating that the bond is largely covalent. This was also concluded in a surface-enhanced Raman spectroscopy study of polycrystalline Au and Ag electrodes by Gao et al. on the basis of the surface−halide stretching frequencies.[143] In addition, an increasingly covalent character in the order $Cl^- < Br^- < I^-$ and a more covalent bond on Au than on Ag was inferred in that study. Halide-induced changes in the electronic structure of Au and Ag single-crystal electrodes were studied by Franke et al. using electroreflectance spectroscopy.[144,145] These metals exhibit surface states that are strongly localized at the metal−electrolyte interface and hence can be used to probe the electric field and electronic states at the interface. Energy shifts, attenuation up to complete quenching, as well as splitting of the surface states were observed, with pronounced differences for different halide species and substrates in the entire range of adsorption, reflecting the different strength of the interaction. In contrast, recent measurements by interference second harmonic generation spectroscopy by Pettinger et al. indicated characteristic differences between the different halide species only in the range of the close-packed adlayers, whereas at lower surface concentrations the signal depended only on the electrode charge.[102,121,146] This was interpreted in terms of an increased mixing of the electronic states of the adsorbate with the d band of the Au(111) substrate in the presence of the high-density adlayer phases. Photoemission studies of dense halogen adlayers under UHV conditions also find a strong binding of the halogen p orbitals to the s and d bands of the metal as well as hybridization of the $p_{x,y}$ halogen orbitals, resulting in a two-dimensional band structure.[147] In addition, a decrease in the halogen core level binding energies with increasing halogen coverage was observed, which was attributed to a weakening of the halogen−metal bond due to increasing adatom−adatom interactions.[147] All these results are supportive of a substantial covalent contribution to the halide−metal bond.

Theoretical investigations of the adsorption geometry, binding energy, and bond ionicity of halides or halogens on metal surfaces were performed using semiempirical methods (see references in ref 86) and ab initio quantum chemical calculations using small clusters[83−87,148,149] The currently most advanced studies, employing density functional theory to include electronic exchange and correlation effects and using clusters of up to 25 metal atoms, were reported by Ignaczak and Gomez for halides on (100)-type Au, Ag, and Cu surfaces[86] and by Koper and van Santen for halogens on (111)-type Ag, Pt, and Hg surfaces.[87] Both found similar bond lengths as in the experimental studies and an increase in adsorption energy in the order I < Br < Cl < F, i.e., in the same order as found at the metal−vacuum interface. The observation of an opposite trend at the electrochemical interface was attributed to the important contribution of solvation, which was not considered in these studies, and to the different reference state (halogens or halides, respectively). Hence, the results correspond most closely to the gas phase adsorption of halogens in the limit of zero coverage. Furthermore, the partial charge on the adsorbate obtained in these studies increased from iodine to fluorine, i.e., according to the experimentally observed trend. Regarding the adsorption strength on different substrates only qualitative and relative comparisons are meaningful, since the binding energies depend strongly on the cluster size. Here an increase in the order Cu ≤ Ag < Au[86] and Pt ≤ Hg < Ag[87] was observed for Cl, Br, and I adsorbed in hollow sites. According to a density-of-states analysis, these trends can be understood by the increasing interaction with the metal d band with higher d band energy or higher halogen electron affinity EA(X).[87] The particularly low halogen adsorption energy on Pt was attributed to the high Pt work function Φ_M, which results in a smaller partial charge of the adsorbate and consequently in a lower electrostatic interaction.[87] Since the adsorption energies of halogens $\Delta E_b(X)$ and halides $\Delta E_b(X^-)$ are related by $\Delta E_b(X^-) = \Delta E_b(X) + EA(X) + \Phi_M$ according to a simple thermodynamic cycle,[150] the halide adsorption energies on Pt are actually higher than on Hg and close to those on Au. In addition, the differences in adsorption energy for different binding sites were investigated by Ignaczak and Gomez.[86] In accordance with the experimental results, the fourfold hollow site was the preferred binding site for all three metals, and the metal−halide bond distances were close to the experimental values. The energetic differences between adsorption in hollow sites and in bridge or top sites, respectively, are considerably smaller than the adsorption energy and increase with decreasing halide diameter and in the order Au < Ag ≤ Cu, i.e., in opposite order as $\Delta E_b(X^-)$. As will be shown in the following sections, these trends in the corrugation potential, i.e., in the spatial modulation of the adsorbate−substrate interaction, can be correlated with the observed structural phase behavior of the halide adlayers on these metals. A better description of the close-packed ordered adlayers as well as a better treatment of charged surfaces should be possible by density functional theory calculations of periodic surfaces. This approach was used by Kramar et al.[151] for the study of a $c(2 \times 2)$ Cl adlayer on a Ag(100) slab. Their results indicate a transfer of s-like charge from Ag surface atoms to the halogen adsorbate and covalent bonds between Cl and neighboring Ag surface atoms via the Cl $p_{x,y}$ orbitals. The observed changes in the surface electronic structure are in qualitative agreement with the electroreflectance experiments by Franke et al.[144]

The effect of the solvent has been predominantly studied by computer simulations. Using molecular dynamics, the distribution of ions and solvent molecules in the interface region was studied by Glosli and Philpott[89−93] as well as by Spohr.[94,95] In these simulations both ions and solvent molecules are arranged in layers, caused by the discreteness of the atomic and molecular species and by packing effects. At the pzc or at positive electrode charges a high surface concentration of halide anions in direct contact with the electrode surface was found, even if a specific chemical interaction was not directly included, whereas the alkali cations were always separated from the metal by a water layer. This illustrates how the different strength of hydration for these ions affects the adsorption behavior and directly confirms the assumptions of classical double layer theory. Furthermore, the studies indicated that the electrostatic field at the interface is dominated by the potential gradient associated with the water dipoles, in particular in the range of low surface concentrations of specifically adsorbed ions.[93,95] Very recently, a first ab initio quantum chemical study of hydrated halide adsorption was reported by Kairys and Head for the case of fluoride and iodide adsorption on the (111) surface of Al clusters.[152] For negatively charged clusters a strong repulsion between water molecules and the Al(111) surface was found for distances <3.0 Å, based on which an explanation for the stronger specific adsorption of I as compared to F was proposed. According to the authors, water molecules in the hydration shell of adsorbed I are sufficiently separated from the metal surface due to the large atomic size of this adsorbate. In contrast, water bound to the small F adsorbate would be drawn into the region of repulsive interaction and therefore destabilized, resulting in an effective weakening of the Al−F bond.

In addition, various groups have employed computer simulations to calculate the free energy of halide anions as a function of its distance from the surface (“potential of mean force”), a quantity that plays an important role in the kinetics of adsorption.[94,153−157] It was shown that the maximum of this curve, which corresponds to the activation energy in phenomenological rate theory, is determined by the desolvation of the anion; however, the construction of the metal−ion interaction potential in these studies is difficult and not unambiguous. All simulation studies up to now focused on the regime of low to moderate anion coverages and are only of limited value for the modeling of the metal−halide interaction in the range of high positive surface charges and large anion surface concentrations, where the solvent is largely displaced from the metal surface. The effect of the residual anion solvation by solvent molecules on top of the halide adlayer, as well as the anion dynamic in these adlayers, is therefore not understood at present.

C. In Situ Results on Halide Adlayer Structure

For Cl^-, Br^-, and I^-, ordered adlayer structures have been observed in in situ studies on single-crystal electrode surfaces of the fcc metals Au,[15,38,40,40,45,46,55,122,158−170] Ag,[15,56,113,123,171−177] Cu,[31,178−185,185,185−188] Pt,[14,15,36,37,48,140,142,189−200] Pd,[201,202] Rh,[203] and Ni.[204] The results of these studies are summarized in Table 1 and will be briefly presented in this chapter in a bird eye perspective, before we commence with a detailed discussion of the adlayer structure using specific examples. For better comparison, both the halide coverage θ relative to the density of substrate surface atoms as well as the corresponding absolute halide surface density Γ are given in Table 1. Here and in the following text, the nomenclature of the original literature, which often somewhat incorrectly employs a simplified Woods notation, is used for convenience.

In general, the results obtained by various groups and different techniques are in good agreement. The variations in the measured lattice parameters can be attributed largely to the limited precision of scanning probe microscopy. The latter is also responsible for the tentative assignment of specific commensurate structures, in particular in older STM/AFM studies, to adlayer phases that later were shown by diffraction methods to exhibit incommensurate structures. Similarly, the small deviations from hexagonal lattices, which occur for uniaxially incommensurate phases, were often not detected by STM/AFM. We will therefore preferentially use the results of diffraction techniques in the detailed discussion of the structural phase behavior. Furthermore, good agreement is also found between the local coverages $\Gamma(E)$ obtained from the structural data and those obtained from a thermodynamic analysis of chronocoulometric measurements,[102,112,114,121,205−207] apart from the 5−15% higher values (see section III.A). An example for the complementary nature of scanning probe microscopy and diffraction results is given in Figure 3, where the diffraction pattern, the corresponding real space adlayer structure, the first, second, and third-order SXS diffraction peaks as well as in situ STM data of the rotated-hexagonal Br adlayer on Au(111) are shown. The adlattice spacing (a_{Br}) and rotation (ϕ) can be obtained alternatively from the reciprocal space position and angular splitting of the diffraction peaks (Figure 3a,c) or directly from the STM image (Figure 3d, part B). A direct comparison of the coverage θ, calculated from the in situ SXS, in situ STM, and chronocoulometric data for Au(111)−Br, illustrates the good agreement of the different experimental techniques (Figure 4).

Ordered halide adlayers are only observed above a critical potential, E_0, located in the regime of high anion coverages ($\theta \geq {}^1/_3$ ML); at lower potentials, the anion adlayer is disordered. The ordered structures form instantaneously on the entire surface after the potential increases above E_0. Coexistence with the disordered phase was never observed, indicating that the ordered phases are stabilized exclusively by repulsive adsorbate−adsorbate interactions. The potential range of the ordered phases depends on the potential of zero charge of the metal surface and on the strength of the metal−halide interaction. For more reactive metals, where the pzc is very negative, the anion adlayer often is ordered within the entire double layer potential range. The potentials of ordered adlayer formation and of phase transitions between different ordered adlayer phases as well as the entire adsorption isotherm $\theta(E)$ obtained in the SXS measurements shift by ≈60 mV per decade of halide bulk concentration (see Figure 4).[46,55,56,122,123,165] At the upper end the double layer potential regime is limited by the onset of halide-induced metal

Table 1. In Situ Data on Halide Adlayer Structures

		electrolyte	structure	θ	Γ (10^{14} cm^{-2})	technique
Au(111)	Cl	10−100 mM NaCl	aligned hex	0.508−0.527	7.05−7.31	SXS[55]
	Br	10 mM NaBr	$(\sqrt{3} \times \sqrt{3})$R30°	$^1/_3$	4.6	STM[40]
			rotated hex	0.41	5.7	
		1−100 mM NaBr	rotated hex	0.462−0.515	6.43−7.12	SXS/STM[46,55]
	I	10 mM NaI	$(\sqrt{3} \times \sqrt{3})$R30°	$^1/_3$	4.6	STM[40]
			(3×3)	$^4/_9$	5.8	
		100 mM $HClO_4$ + 0.5 mM KI	$(\sqrt{3} \times \sqrt{3})$R30°	$^1/_3$	4.6	STM[38,158]
			$(5 \times \sqrt{3})$	$^2/_5$	5.5	
			(7×7)R21.8°	0.44	6.1	
		100 mM $HClO_4$[a]	$(5 \times \sqrt{3})$	$^2/_5$	5.5	STM[159]
			(7×7)R21.8°	0.44	6.1	
		10−100 mM KI	$c(p \times \sqrt{3})$	0.367−0.410	5.11−5.71	SXS[122]
			rotated hex	0.417−0.446	5.80−6.21	
		1 mM KI	$(\sqrt{3} \times \sqrt{3})$R30°	$^1/_3$	4.6	STM/LEED[45,162,163]
			$c(p \times \sqrt{3})$	0.33−0.41	4.65.7	
			rotated hex	0.41−0.45	5.7−6.2	
Au(100)	Cl	50 mM NaCl	$c(\sqrt{2} \times 2\sqrt{2})$R45°	$^1/_2$	6.01	SXS[168]
			$c(\sqrt{2} \times p)$R45°	0.553−0.575	6.64−6.91	
		100 mM H_2SO_4 + 1 mM HCl	$c(\sqrt{2} \times p)$R45°	0.5−0.62	6.0−7.4	STM[169]
	Br	50 mM NaBr	$c(\sqrt{2} \times 2\sqrt{2})$R45°	$^1/_2$	6.01	SXS[164,165]
			$c(\sqrt{2} \times p)$R45°	0.500−0.565	6.01−6.79	
		100 mM H_2SO_4 + 1 mM HBr	$c(\sqrt{2} \times 2\sqrt{2})$R45°	$^1/_2$	6.0	STM[169]
			$c(\sqrt{2} \times p)$R45°	0.5−0.57	6.0−6.8	
	I	10 mM KI	$c(p \times 2\sqrt{2})$R45°	0.46−0.49	5.5−5.9	STM[160]
			$c(\sqrt{2} \times 2\sqrt{2})$R45°	$^1/_2$	6.01	
			rotated hex	0.5	6.01	
		50 mM NaI	$c(p \times 2\sqrt{2})$R45°	0.455−0.468	5.46−5.62	SXS[168]
			rotated pseudohex			
			$c(\sqrt{2} \times 2\sqrt{2})$R45°	$^1/_2$	6.01	
Au(110)	Br	50 mM $HClO_4$ + 10 mM KBr	(1×3)	$^2/_3$	5.66	STM[170]
			(1×4)	$^3/_4$	6.37	
			rotated pseudohex	$^3/_4$	6.37	
	I	10 mM CsI	$c(2 \times 4)$[b]	$^1/_4$	2.12	STM[161]
			rotated pseudohex	0.62−0.65	5.27−5.52	
			(3×2)	$^2/_3$	5.66	
		10−100 mM CsI	$c(2 \times 4)$[b]	$^3/_8$	3.19	SXS[166]
		10−100 mM LiI, KI, NaI	$c(2 \times p)$[b]	0.390−0.416	3.31−3.53	SXS[166]
		10 mM KI, 10 mM KI + 90 mM KF	$c(2 \times p)$[b]	0.390−0.416	3.31−3.53	SXS[167]
			rotated pseudohex	0.62−0.66	5.27−5.61	
			$c(p \times 2)$	0.68−0.71	5.78−6.03	
			$c(p \times 1)$	0.62−0.81	5.27−6.88	
Ag(111)	Cl	10 mM KCl	aligned hex	0.53	7.33	STM[171]
		10−100 mM NaCl + 100 mM $HClO_4$	aligned hex	0.523−0.535	7.23−7.40	SXS[56]
	Br	10 mM KBr	$(\sqrt{7} \times \sqrt{7})$R19.1°	$^3/_7$	5.9	STM[172]
		0.1 mM KBr + 10 mM KF, 2 mM HBr	(3×3)	$^4/_9$	6.1	AFM[173]
		10 mM NaBr + 100 mM $HClO_4$	(7×7)	0.510	7.05	SXS[56,123]
	I	0.1 mM KI +	$(\sqrt{3} \times \sqrt{3})$R30°	$^1/_3$	4.57	STM[172]
		10 mM NaF	(8×8)	0.391	5.46	
		0.1 mM KI + 10 mM KF + 1.5 mM HF	$(\sqrt{3} \times \sqrt{3})$R30°	$^1/_3$	4.57	AFM[173]
		10−100 mM NaI, 10 mM NaI + 90 mM NaF	$(\sqrt{3} \times \sqrt{3})$R30°	$^1/_3$	4.57	SXS[56,123]
			$c(p \times \sqrt{3})$	0.355−0.400	4.91−5.54	
			$(5 \times \sqrt{3})$	$^2/_5$	5.54	
			rotated hex	0.417−0.435	5.77−6.02	
		0.1 mM HI	$(\sqrt{3} \times \sqrt{3})$R30°	$^1/_3$	4.57	STM/LEED[174]
			$c(p \times \sqrt{3})$	0.33−0.38	4.57−5.26	
			rotated hex	0.41	5.67	
		0.1 mM KI + KOH (pH 10)	$(\sqrt{3} \times \sqrt{3}R - 30°)$	0.29	4.01	STM/LEED[174]
			$(\sqrt{3}p \times \sqrt{3}R - 30°)$	0.29−0.33	4.01−4.57	
			$(\sqrt{3} \times \sqrt{3})$R30°	$^1/_3$	4.57	
			rotated hex	0.45	6.23	
Ag(100)	Cl	50 mM NaCl + NaOH (pH 10)	$c(2 \times 2)$	$^1/_2$	6.0	SXS[175,176]
	Br	50 mM NaBr + NaOH (pH 10)	$c(2 \times 2)$	$^1/_2$	6.0	SXS[113,175,176]
	I	100 mM $HClO_4$[a]	$c(2 \times 2)$	$^1/_2$	6.0	STM[177]
		50 mM KI + NaOH (pH 10)	$c(2 \times 2)$	$^1/_2$	6.0	SXS[175,176]
Cu(111)	Cl	110 mM HCl, 110 mM KCl	$(6\sqrt{3} \times 6\sqrt{3})$R30°	0.454	8.0	STM[178]
		10 mM HCl	$(\sqrt{3} \times \sqrt{3})$R30°	$^1/_3$	5.9	STM[31,184]
		0.1 mM HCl + 10 mM $HClO_4$	$c(p \times \sqrt{3})$	0.395−0.405	7.00−7.16	STM/LEED[185]
	Br	0.1 mM KBr + 10 mM $HClO_4$	$c(p \times \sqrt{3})$	0.355−0.385	6.27−6.80	STM/LEED[185]
	I	0.1 mM KI + 10 mM $HClO_4$	$(\sqrt{3} \times \sqrt{3})$R30°	$^1/_3$	5.9	STM/LEED[185]
Cu(100)	Cl	10 mM HCl	$c(2 \times 2)$	$^1/_2$	7.7	STM[179]
		110 mM HCl	$c(2 \times 2)$	$^1/_2$	7.7	STM[181,186]
		10 mM HCl	$c(2 \times 2)$	$^1/_2$	7.7	STM[182,183,187]
	Br	10 mM HBr	$c(2 \times 2)$	$^1/_2$	7.7	STM[188]

Table 1 (Continued)

		electrolyte	structure	θ	Γ (10^{14} cm^{-2})	technique
Cu(110)	Cl	1 mM HCl + 3 mM $HClO_4$	aligned pseudohex	0.84	9.1	AFM[180]
		100 mM $HClO_4$ + 1 mM HCl	(4 × 1)	$^3/_4$	8.1	STM[280]
		100 mM HCl	(4 × 1)	$^3/_4$	8.1	STM[281]
			(5 × 1)	$^4/_5$	8.7	
	Br	100 mM $HClO_4$ + 1 mM KBr	$c(2 \times 2)$	$^1/_2$	6.1	STM[280]
	I	100 mM $HClO_4$ + 1 mM KI	$c(2 \times 2)$	$^1/_2$	6.1	STM[280]
Pt(111)	Cl	10 mM KCl + 100 mM $HClO_4$		0.4−0.6	6.0−9.0	SXS[142]
	Br	10 mM KBr + 100 mM $HClO_4$	aligned hex	0.443−0.509	6.64−7.63	SXS[140]
		10 mM KBr + 100 mM $HClO_4$	(3 × 3)	$^4/_9$	6.66	SXS[142]
			aligned hex (7 × 7)	0.510	7.65	
		3 mM KBr + 10 mM $HClO_4$	aligned hex	$\leq ^4/_9$	≤6.66	STM[197]
			(3 × 3)	$^4/_9$	6.66	
		20 mM KBr + 100 mM $HClO_4$	(3 × 3)	$^4/_9$	6.66	SXS[14,15]
	I	100 mM $HClO_4$[a]	$(\sqrt{3} \times \sqrt{3})R30°$	$^1/_3$	5.00	STM[37]
			$(\sqrt{7} \times \sqrt{7})R19.1°$	$^3/_7$	6.43	
		0.1 mM KI + 0.1 mM $HClO_4$ + 10 mM $NaClO_4$[a]	(3 × 3)	$^4/_9$	6.66	STM[48,191,192]
		1 M $HClO_4$[a]	$(\sqrt{7} \times \sqrt{7})R19.1°$	$^3/_7$	6.43	STM[193,198,199]
		50 mM H_2SO_4 + 1 mM KI	(3 × 3)	$^4/_9$	6.66	
		10 mM KI + 100 M $HClO_4$	$(\sqrt{7} \times \sqrt{7})R19.1°$	$^3/_7$	6.43	SXS[123]
			(3 × 3)	$^4/_9$	6.66	
		10 mM KI + 100 M $HClO_4$	$(\sqrt{7} \times \sqrt{7})R19.1°$	$^3/_7$	6.43	SXS[142]
			(3 × 3)	$^4/_9$	6.66	
Pt(100)	Br	2.25 mM KBr + 50 mM H_2SO_4[a]	aligned pseudohex	0.42	5.5	STM[194]
		0.08 mM KBr + 100 mM $HClO_4$		0.35−0.4	4.5−5.2	SXS[141]
	I	1 M $HClO_4$[a]	$c(2 \times 2)$	$^1/_2$	6.49	STM[189]
			$(\sqrt{2} \times 5\sqrt{2})R45°$	$^3/_5$	7.79	
		0.1 mM KI + 0.1 mM $HclO_4$ + 10 mM $NaClO_4$[a]	$(\sqrt{2} \times 5\sqrt{2})R45°$	$^3/_5$	7.79	STM[48,190,191]
		0.1 mM KI + 0.1 mM $HclO_4$ + 10 mM $NaClO_4$[a]	$c(2 \times 2)$	$^1/_2$	6.49	STM[192]
			$(\sqrt{2} \times 5\sqrt{2})R45°$	$^3/_5$	7.79	
		$HClO_4$[a]	$(\sqrt{2} \times 5\sqrt{2})R45°$	$^3/_5$	7.79	STM[36]
Pt(110)	Br	2 mM KBr + 50 mM H_2SO_4	$(7 \times p)$			STM[194]
	Br	10 mM KBr + 100 mM $HClO_4$	(6 × 2)	$^2/_3$	6.12	STM[200]
	I	50 mM H_2SO_4[a]	(4 × 1)	$^3/_4$	6.89	STM[195]
		1 M $HClO_4$[a]	(2 × 1)	$^1/_2$	4.59	STM[196]
Pd(111)	I	50 mM H_2SO_4[a]	$(\sqrt{3} \times \sqrt{3})R30°$	$^1/_3$	5.09	STM[201]
Pd(100)	I	50 mM H_2SO_4,[a] 1 mM KI + 50 mM H_2SO_4	$c(2 \times 2)$	$^1/_2$	6.61	STM[201,202]
Rh(111)	I	100 mM $HClO_4$[a]	$(\sqrt{3} \times \sqrt{3})R30°$	$^1/_3$	5.323	STM[203]
Ni(111)	I	1 mM KI + 10 mM HF	$(\sqrt{3} \times \sqrt{3})R30°$	$^1/_3$	6.20	STM[204]

[a] Halide species preadsorbed prior to immersion in electrolyte. [b] Mixed alkali−halide adlayer.

dissolution, bulk halide formation, or—in the case of iodide—polyiodide formation. Although the dense halide adlayers are maintained on the surface during metal dissolution, at least in the range of low dissolution rates (see section VII.A), high-resolution STM/AFM or SXS studies are usually more difficult in the presence of these processes.

On the hexagonally ordered (111) surfaces of fcc metals, halides form predominantly close-packed hexagonal adlayer structures, reflecting the isotropic adsorbate−adsorbate interactions. At saturation coverages, the adlattice spacings are typically slightly above the halide van der Waals diameters.[208] For halide adlayers on the coinage metal surfaces Cu(111), Ag(111), and particularly Au(111), often incommensurate structures with lattice spacings that decrease with increasing potential were found (see, for example, Figures 3 and 4). This potential-induced compression of the adlattice—usually termed electrocompression—will be discussed in detail in section III.F. Notable exceptions are Cu(111)−I, where a simple $(\sqrt{3} \times \sqrt{3})R30°$ structure is formed according to an STM study by Inukai et al.[185] and Ag(111)−Br,[56,123,172,173] where different high-order commensurate structures were reported by several groups. A particular rich phase behavior was observed for iodide adlayers on Au(111) and Ag(111), where a sequence of disordered, low-order commensurate (C), uniaxial incommensurate (UIC), and two-dimensional incommensurate (IC) adlayer phases was observed with increasing potential by Ocko et al.[56,122,123] (see section III.D). On the (111) surfaces of transition metals, well-ordered adlayers always seem to exhibit commensurate structures, indicating a stronger preference for energetically favorable adsorption sites. The only reported exception is Pt(111)−Br, where Lucas et al. found indications for more compressed incommensurate or high-order commensurate structures with large unit cells; however, the adlayer in this case was poorly ordered.[142]

Halide adlayers on fcc(100) surfaces exhibit a stronger tendency toward commensurate structures, with a predominant occurrence of simple $c(2 \times 2)$ adlattices. This reflects the higher substrate corrugation potential on the more open, square (100) lattice. Incommensurate phases are only observed on Au(100), corresponding to the trend observed on the (111) surfaces. Only a few studies of halides on fcc(110) surfaces exist, which in general find pseudohexagonal adlayers, where the anions are adsorbed in the atomic rails along the $[1\bar{1}0]$ direction. Again a notable

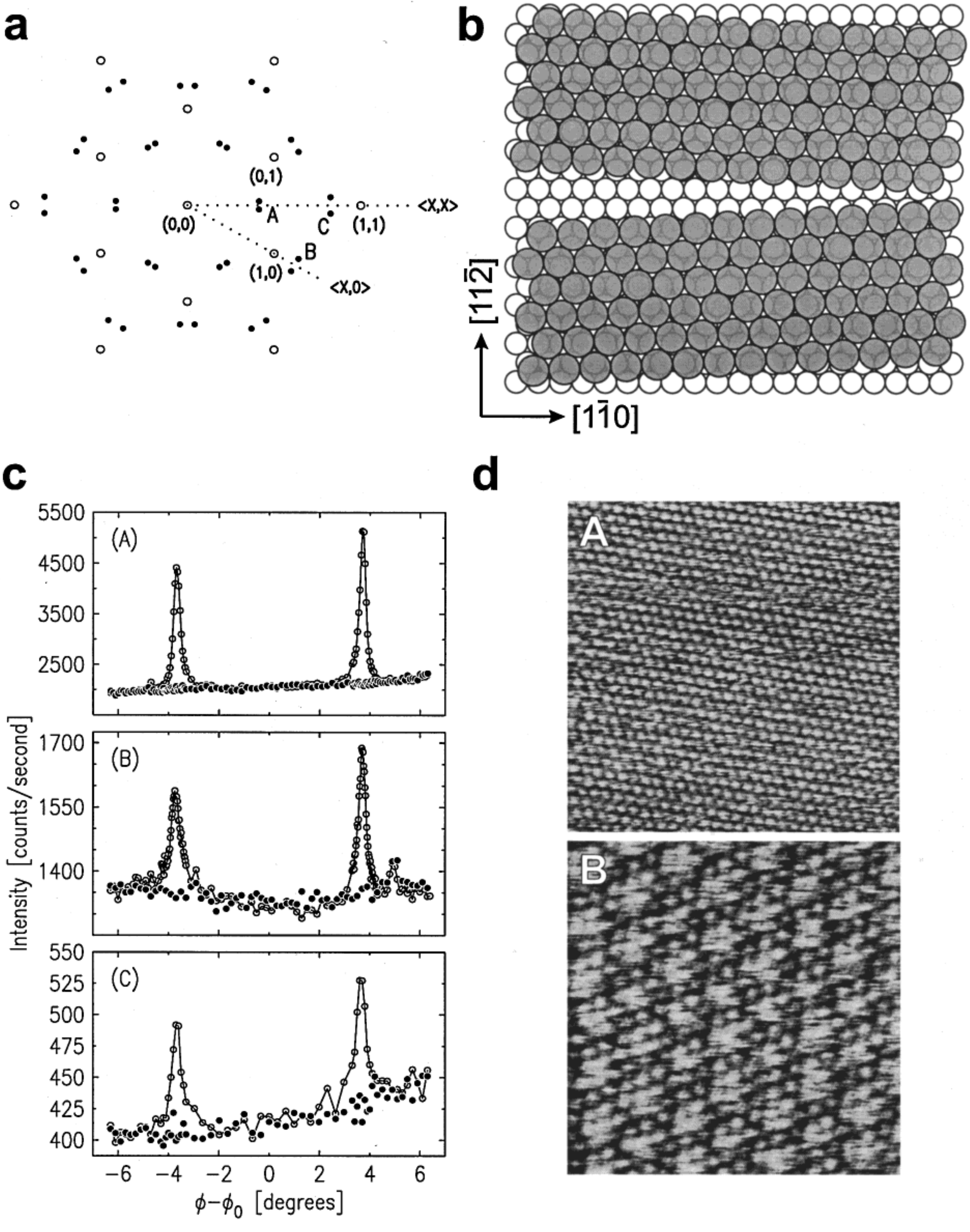

Figure 3. In situ SXS and in situ STM data for the Br adlayer on Au(111). (a) X-ray diffraction pattern, (b) corresponding adlayer structure, (c) azimuthal SXS scans through the first (A), second (B), and third (C) order diffraction peaks at 0.2 V (filled circles) and 0.6 V (open circles) in 100 mM $HClO_4$ + 10 mM NaBr, and (d) STM images obtained at 0.44 V (A) and 0.74 V (B) in 100 mM $HClO_4$ + 1 mM NaBr (80 × 80 Å^2). Both SXS and STM indicate a disordered adlayer at the negative and a rotated-hexagonal Br adlayer at the positive potential. (Reprinted with permission from ref 46. Copyright 1996 American Chemical Society.)

exception is Au(110), where an rotated incommensurate phase was observed for the iodide adlayer by Gao et al.[161] and Wang et al.[167] No ordered halide adlayers have been reported up to now for higher index surfaces or on hcp or bcc metals.

For completeness sake, it should be mentioned that at high positive potentials, where the two-dimensional adlayers are replaced by bulk phases, very different surface structures can be found. Gao and Weaver[38,39] observed under these conditions that the hexagonal-rotated iodide adlayer on Au(111) is replaced by a polyiodide phase. In this phase, the iodine atoms are arranged in chains with an atomic spacing of about 2.9 Å along the chain. The chains form a

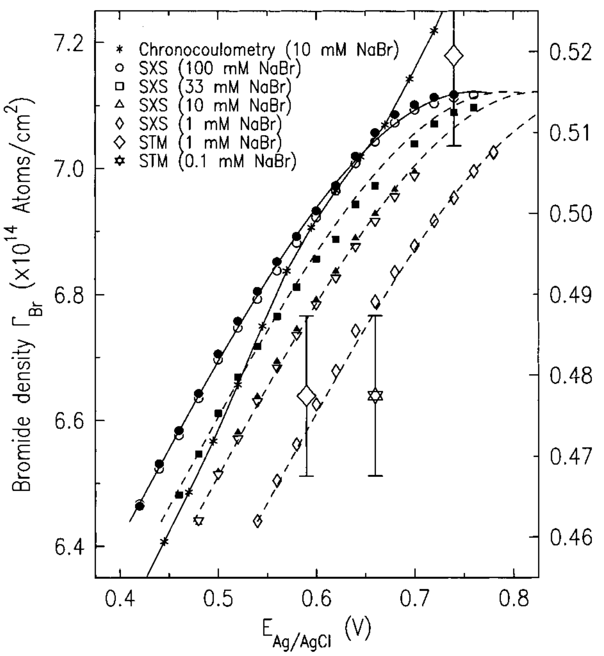

Figure 4. Surface concentration Γ and coverage θ obtained by in situ SXS, in situ STM, and chronocoulometry[205] for the incommensurate, compressible Br adlayer on Au(111). Open and filled symbols in the SXS data correspond to the positive and negative direction of the potential sweep, respectively. (Reprinted with permission from ref 46. Copyright 1996 American Chemical Society.)

disordered, hexagonal network on the Au surface and are preferentially aligned along the [1$\bar{1}$0] direction of the substrate, which was attributed to the close match of the interchain iodine−iodine and the Au lattice spacing. Furthermore, ex situ STM studies by Schott and White[209,210] on Ag(111) samples quenched in hot, concentrated acid halide solutions revealed unusual double row atomic structures, which might be interpreted as thin epitaxial Ag halide films. All these bulklike phases differ quite strongly from the two-dimensional adlayer phases found in the double layer regime and will not be discussed in more detail in this work.

The structure and phase behavior of halide adlayers at the electrochemical interface is very similar to that of adlayers formed by the (dissociative) adsorption of halogens from the gas phase.[**125−137**,147,211−242] This is particularly well illustrated by the results for iodine adsorption on Ag(111) and Au(111), where the same complex series of adlayer phases as in the electrochemical environment was observed.[126−129,211,216,217] The most pronounced differences are found at low coverages. Here relatively open commensurate structures, such as ($\sqrt{3} \times \sqrt{3}$)R30° for Ag(111)−Cl,[213] Ag(111)−Br,[214] Au(111)−Cl,[124] and Au(111)−I [216] as well as $c(2 \times 4)$ for Pt(100)−I,[243] were observed in the UHV studies, but not in the corresponding electrochemical systems. These differences can be related to solvation effects at the electrochemical interface (see above), which are most pronounced in the low-coverage regime. A second point concerns the high coverage regime, which can be limited at the solid−liquid interface by electrochemical reactions (e.g. metal dissolution) that do not occur under UHV conditions. For example, only a ($\sqrt{3} \times \sqrt{3}$)R30° structure is observed for electrochemical iodide adsorption on Cu(111) prior to Cu dissolution,[185] whereas a uniaxial compressed phase was reported at high coverages in the corresponding UHV system.[240,241]

Overall, the chemisorbed halide (or halogen) adlayers, in particular those on coinage metal surfaces, exhibit a structural phase behavior that closely resembles that of classical two-dimensional systems, such as physisorbed noble gases on graphite and metal surfaces.[244−248] This will be shown explicitly in the following subsections, where specific effects and systems are considered in detail. An advantage of the electrochemical environment as compared to the solid−vacuum interface is that the adlayers are close to equilibrium, as can be seen from the excellent agreement of the lattice parameters obtained in the positive and in the negative potential sweep (see Figure 4). Since the free energy of adsorption and hence the corresponding adlayer structure can be directly controlled via the electrode potential, metal electrodes in halide solutions are interesting model systems for fundamental studies of phase transitions in two dimensions.

D. Halide Adlayer Phases on Ag(111) and Au(111)

On the hexagonal close-packed (111) faces of fcc metals, the corrugation potential is particularly weak and of comparable order as the lateral interactions between the halide adsorbates in high-density adlayers. Consequently, adsorbate−adsorbate and adsorbate−substrate interactions equally influence the adlayer structure, resulting in a complex adlayer phase behavior.[244−248] If the average adlayer lattice spacing (a_{ad}) is different from that of the substrate (a_s), the resulting structure is a compromise between a simple commensurate structure (Figure 5a), which minimizes the interface energy resulting from the corrugation in the adsorption energy, and a uniformly compressed incommensurate phase (Figure 5b), favored by the elastic lateral interactions in the adlayer. In a simple one-dimensional model, originally proposed by Frenkel and Kontorowa[249] and Frank and van der Merwe,[250] the lowest energy state

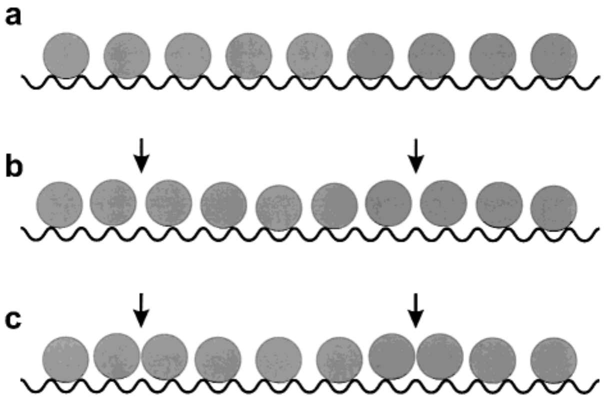

Figure 5. Schematic models of (a) simple commensurate, (b) uniformly compressed, and (c) domain-wall adlayer structures (the adsorbate coverage in panels b and c is identical). The positions of the maxima of the Moiré pattern in part b and of the domain walls in part c are indicated by arrows.

corresponds to a system of commensurate regions separated by domain walls (also called solitons or misfit dislocations), in which the adsorbates are displaced from the preferred substrate sites (Figure 5c). The spacing and width of these domain walls are determined by the lattice mismatch a_{ad}/a_s and by the ratio of corrugation potential and lateral interaction energy, respectively. For two-dimensional structures, the symmetry of the adlattice depends on the energy associated with the crossing of the domain walls:[251] if the wall crossing energy is positive, i.e., the walls repel each other, the walls arrange in periodically spaced, parallel lines, resulting in uniaxially incommensurate phases ("striped phases"). In contrast, for a negative wall energy, i.e., attractive interactions, a hexagonal arrangement of the domain walls is observed. In the limit of sharp domain walls this results in the formation of ordered dislocation networks, a prime example of which is the Au(111) reconstruction.[252] Such domain-wall structures are restricted to small mismatches, where the average adlayer spacings are close to that in the commensurate structure and hence commonly called weakly incommensurate phases. It should be noted that the experimental observation of these dislocation structures is often difficult, in particular if the domain walls are broad or their positions undergo strong entropic fluctuations. With increasing compression of the adlattice, the domain wall spacing decreases and the domain walls increasingly overlap, approaching a structure close to a uniformly compressed adlayer (often called a "floating two-dimensional solid"). In this regime the adlayer symmetry, i.e., the occurrence of striped or hexagonal phases, is better rationalized by the competing tendencies of the adsorbates to arrange on the one hand isotropically on the surface and to avoid on the other hand energetically unfavorable adsorption sites (see below). For uniformly compressed incommensurate phases as well as dislocation structures, the displacement of adsorbates from the commensurate positions can result in a long-range vertical modulation ("Moiré pattern") of the adlayer, which often can be directly observed by STM[38,40,45,46,158,162,163,169,174,253,254] (see, for example, Figure 3d, part B).

The whole sequence of possible adlayer structures is illustrated by the system Ag(111)−I, where ordered phases are observed over a wide range of potentials and surface coverages, due to the strong adsorption and high polarizability of the iodide adsorbate. Starting at the most negative potentials, where the halide adlayer is disordered, a commensurate $(\sqrt{3} \times \sqrt{3})$R30° (Figure 6a, A), an uniaxial-incommensurate $c(p \times \sqrt{3})$ (Figure 6a, part B), and an incommensurate rotated-hexagonal structure (Figure 6a, part C) were found with increasing potential in a SXS study by Magnussen et al.[56,123] as well by Yamada et al. using STM and ex situ LEED,[174] with the coverage θ increasing from $^1/_3$ in the commensurate phase to 0.442 at the most positive potentials. The $c(p \times \sqrt{3})$ structure is obtained by a uniaxial compression of the $(\sqrt{3} \times \sqrt{3})$R30° adlattice along the $[1\bar{1}0]$ direction of the Ag substrate, resulting in a centered rectangular unit cell with unit cell vectors of length $\sqrt{3}$ along the commensurate direction and of length p perpendicular to that. In this structure, the iodide atoms reside on three-fold hollow, bridge, or intermediate sites; top sites are not occupied. With increasing potential p decreases and the coverage θ, which is equal to p^{-1}, increases. The incommensurability is measured by the uniaxial lattice mismatch relative to the $(\sqrt{3} \times \sqrt{3})$R30° phase, which is $\epsilon = 1 - p/3$. From the absence of satellite peaks in the SXS data—expected for sharp domain walls[255]—it was concluded that the $c(p \times \sqrt{3})$ phase is better described as a uniformly compressed structure.[56,123] This is supported by the STM observations of Yamada et al.,[174] where a uniform adatom spacing was reported, as well as by the large lattice mismatch ϵ (see below), which is inconsistent with a weakly incommensurate phase. Finally, a completely incommensurate adlayer is attained in the rotated-hexagonal phase. Here $\theta = |a_{Ag}/a_I|^2$, where a_I is the potential-dependent nearest neighbor spacing in the hexagonal iodide adlattice and $a_{Ag} = 2.889$ Å is the Ag−Ag spacing. The rotation angle between adsorbate and substrate lattice is in

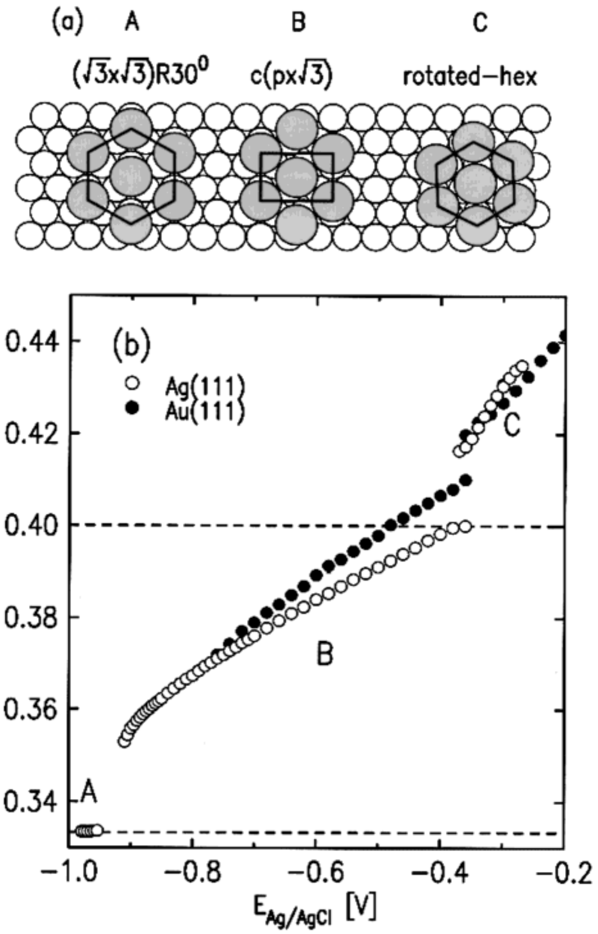

Figure 6. (a) Structure of iodide adlayers on Ag(111) and Au(111) as deduced from in situ SXS. From the left to the right are shown the commensurate $(\sqrt{3} \times \sqrt{3})$R30° (A), the uniaxial-incommensurate $c(p \times \sqrt{3})$ (B), and the incommensurate rotated-hexagonal (C) phases. (b) The potential-dependence of the iodide coverage θ obtained from the SXS data in electrolyte containing 100 mM I^-. The potential scale of the Au(111) data has been shifted negatively by 0.5 V to facilitate the comparison with the Ag(111) data. (Reprinted with permission from ref 123. Copyright 1996 Elsevier Science Ltd.)

Table 2. Structural Parameters of Halide Adlayers on the (111) Surfaces of the Noble Metals[a]

			$\partial\Gamma/\partial E$ (10^{14} cm^{-2} V^{-1})	$a_X(E_0)$ (Å)	$a_X(E_{max})$ (Å)	$a_X(E_0)/a_{X,vdW}$[b]	$a_X(E_{max})/a_{X,vdW}$[b]	$\sqrt{3}a_{Me}/a_{X,vdW}$[b]
Au(111)	Cl	IC	2.41 ± 0.15	4.03	3.95	1.15	1.12	1.42
	Br	IC	2.95 ± 0.07	4.24	4.03	1.15	1.09	1.35
	I	UIC	1.30 ± 0.02	4.62	4.32	1.17 (1.20[c])	1.09 (1.14[c])	1.26
		IC	1.98 ± 0.02	4.47	4.33	1.13	1.09	
Ag(111)	Cl	IC	2.84 ± 0.5	4.00	3.95	1.14	1.12	1.42
	Br	HOC		4.04		1.09		1.35
	I	C		5.00		1.27		1.26
		UIC[d]	1.04 ± 0.03	4.8	4.39	1.21 (1.22[c])	1.11 (1.15[c])	
		IC	3.26 ± 0.05	4.48	4.38	1.13	1.11	
Cu(111)	Cl[e]	UIC	0.9	3.9	3.87	1.11 (1.16[c])	1.10 (1.14[c])	1.26
	Br	UIC	2.9	4.2	3.99	1.14 (1.16[c])	1.08 (1.11[c])	1.20
	I	C		4.43		1.12		1.12

[a] Electrocompression, nearest neighbor spacing (a_X) at the potential of phase formation (E_0) and at the positive potential limit of the ordered phase (E_{max}), and ratios of the spacings a_X to the halide van der Waals diameters $a_{X,vdW}$ for simple commensurate (C), high-order commensurate (HOC), uniaxial-incommensurate (UIC), and incommensurate (IC) halide adlayer phases (data taken from refs 37, 46, 55, 56, 122, 123, 185, 201, 203, and 204). In addition, the mismatch of $a_{X,vdW}$ and the $(\sqrt{3} \times \sqrt{3})R30°$ lattice spacing for the metal−halide system is given. [b] Halide van der Waals diameters $a_{X,vdW}$ of 3.52, 3.70, and 3.96 Å were used for Cl, Br, and I, respectively.[208] [c] Calculated using the average spacing given by $a_{Me}/\sqrt{\theta}$. [d] Determined in the potential range −0.8 to −0.4 $V_{Ag/AgCl}$, where the electrocompression is approximately constant. A considerably higher (nonlinear) compression is found close to the C−UIC transition. [e] Results of the in situ STM/ex situ LEED study by Inukai et al.;[185] different structures were reported in the in situ STM studies of Suggs and Bard[178] and Kruft et al.[31,184]

the range of 1° to 2.5° and varies as a function of the potential.[56,123]

In Figure 6b the potential dependence of the iodide phase behavior on the Ag(111) surface is summarized in a plot of the coverage obtained from the SXS data. The commensurate $(\sqrt{3} \times \sqrt{3})R30°$ phase is only stable in a small, ≈40 mV wide potential regime. In this range the intensity of the corresponding diffraction peaks first continuously increases, reaches a peak, and immediately decreases again, parallel to the emergence of diffraction peaks corresponding to the $c(p \times \sqrt{3})$ structure. Hence, the $(\sqrt{3} \times \sqrt{3})R30°$ phase apparently is only formed transiently in a range where the iodide coverage, which continuously varies with potential, is close to $^1/_3$. In contrast, the $c(p \times \sqrt{3})$ phase, where the iodide adlattice density can continuously vary with potential, is found in a 0.56 V wide potential range, with θ increasing from about 0.355 to 0.40. This corresponds to a change in the iodide nearest neighbor spacing from 4.8 to 4.39 Å (see Table 2) and in the incommensurability ϵ from 0.06 to 0.17. At lower ϵ, precise determination of the adlayer structure is hampered by the overlap of the diffraction peaks corresponding to the three symmetry equivalent domains of the $c(p \times \sqrt{3})$ phase, which cannot easily be separated. Qualitatively, the SXS data indicates a discontinuous change in ϵ and a first order $(\sqrt{3} \times \sqrt{3})R30° \leftrightarrow c(p \times \sqrt{3})$ phase transition.[56] At the most positive potential, the $c(p \times \sqrt{3})$ phase corresponds to a $(5 \times \sqrt{3})$ high-order commensurate structure, where half of the iodide atoms reside on hollow sites and the others on bridge sites. Upon further potential increase, the $(5 \times \sqrt{3})$ phase vanishes and the rotated-hexagonal phase is formed in a first-order phase transition. Due to the removal of the uniaxial distortion, the initial nearest neighbor spacing in the new phase is 4.59 Å, i.e., 5% larger than in the $(5 \times \sqrt{3})$ phase, despite its higher coverage of $\theta = 0.417$. The rotated-hexagonal adlattice is continuously compressed with increasing potential up to the upper limit of the double layer regime, where bulk AgI formation commences.

Very similar structures, i.e., a $(\sqrt{3} \times \sqrt{3})R30°$ phase for $\theta = {}^1/_3$, followed by incommensurate phases up to $\theta = 0.48$, were observed for iodine adsorption on Ag(111) surfaces in ultrahigh vacuum.[126,128,129,211,216,217] Although an unambiguous structural assignment of the incommensurate phases was not possible, the observed LEED pattern is in good agreement with the peak positions in the in situ SXS data. In particular, also in UHV a continuous shift in the diffraction positions with iodine dosage was observed, indicating a compressible adlayer.

The observed phase sequence is an elegant example of the stepwise loss of commensuration within two distinct phase transformations with increasing coverage. This sequence was also predicted by Bak et al.[251] using Landau theory and Kardar[256] using a generalized three-state Potts model. Application of these models to the Ag(111)−I system seems doubtful, however, since in both weakly incommensurate phases were assumed. A better approach seems to be a treatment in terms of a uniformly compressed adlayer, where the structures are rationalized on the basis of the competition between the spatially modulated adsorbate−substrate interaction and packing constraints due to repulsive adsorbate−adsorbate interactions. In the uniaxial-incommensurate phase, the adsorbates reside in rows defined by the bridge and hollow sites of the Ag substrate, and this configuration has a lower interfacial energy than the rotated-hexagonal phase, where some of the adsorbates must occupy energetically unfavorable top sites. However, the uniaxial-incommensurate phase is slightly distorted from the hexagonal configuration, and this distortion increases the adsorbate−adsorbate elastic interaction energy. With increasing potential the distortion increases up to a critical coverage, where the energy associated with the adlattice distortion exceeds the energy gain due to the lower interface energy, resulting in a transition into the incommensurate, rotated-hexagonal phase.

It is instructive to compare the phase behavior of Ag(111)−I with that of iodide on the Au(111) surface, which exhibits an almost identical substrate geometry due to the very similar lattice spacing (a_{Au} = 2.885 Å). Both incommensurate phases—the $c(p \times \sqrt{3})$ and the rotated-hexagonal phase—were observed for Au(111)−I by Gao and Weaver[38] as well as Haiss et al.[158] using in situ STM, Ocko et al. using in situ SXS,[122] and Yamada et al. using in situ STM/ex situ LEED.[45,162,163] The commensurate $(\sqrt{3} \times \sqrt{3})$R30° phase was found by STM and LEED,[38,40,45,158,162,163] but not in the SXS measurements.[122] This might suggests that this structure only exists as a short-range ordered phase. As for Ag(111)−I, the absence of satellite peaks and the considerable incommensurability imply that the adlayer in the $c(p \times \sqrt{3})$ phase is a uniformly compressed rather than a domain-wall structure, which is supported also by the in situ STM observations.[38,45,162,163] However, a recent ex situ STM study of iodide adlayers formed by adsorption from methanol solution by Huang et al.[254] observed—albeit rarely—a uniaxial dislocation network structure with superheavy domain walls, suggesting that the presence of the electrolyte may promote the relaxation of the domain walls to a more uniformly compressed structure. The potential-dependent coverage in the incommensurate phases, obtained from the SXS data, is included in Figure 6b. For better comparison, the potential scale for the data on Au(111)−I was shifted by −0.5 V, to correct for the difference in pzc of Ag and Au. Obviously, the adlayer phase behavior on the two substrates is quite similar. In the $c(p \times \sqrt{3})$ phase the minimum and maximum coverage and the electrocompressibility $d\theta/dE$ are slightly larger on Au than on Ag. Interestingly, the $c(p \times \sqrt{3})$ phase on Au does not lock in into the commensurate $(5 \times \sqrt{3})$ structure but is continuously compressed at coverages around 0.40. This, as well as the absence of a well-ordered $(\sqrt{3} \times \sqrt{3})$R30° phase indicate a reduced tendency toward commensurate structures, which can be rationalized by a weaker substrate corrugation potential on Au(111) as compared to Ag(111). A similar trend in the corrugation potentials is found in the density functional calculations of Ignaczak and Gomez.[86] Almost identical isotherms $\theta(E)$ are observed in the rotated-hexagonal phase, suggesting that substrate effects are minimal within this phase, as expected for incommensurate, “floating” structures.

In addition, the iodide adlayer structure may be influenced by the solution pH, as reported in the STM/LEED study of Ag(111)−I by Yamada et al.[174] Here the sequence of adlayer structures found in alkaline KOH solution differed from those obtained in acidic or neutral electrolyte. With increasing potential first a square $(\sqrt{3} \times \sqrt{3})$ phase, followed by a continuous transition to the $(\sqrt{3} \times \sqrt{3})$R30° structure, and finally a direct transition to the rotated-hexagonal adlayer without an intermediate $c(p \times \sqrt{3})$ phase was observed in the alkaline electrolyte. On the basis of parallel Auger electron spectroscopy measurements, which revealed a significant potassium signal at potentials negative of the potential regime of the rotated-hexagonal phase, this behavior was attributed to the influence of potassium coadsorption on the adlayer structure.[174] Indeed, the rather open structures—in particular the square adlayer phase found at the most negative potentials—resemble the mixed alkali iodide phases observed on Au(110) (see section V).

E. Adlayer Phases in Other fcc (111)-Halide Systems

Each of the other metal(111)−halide systems exhibits only one type of these adlayer phases, i.e., either a commensurate, a uniaxial-incommensurate, or an incommensurate structure (summarized in Table 2). Particularly notable is the rare occurrence of the simple commensurate $(\sqrt{3} \times \sqrt{3})$R30° superstructure in the electrochemical environment. Formation of this structure should in principle be possible for all halide−metal systems, since the lattice mismatch $a_{\mathrm{X,vdW}}/a_{\mathrm{Me}}$—estimated from the halide van der Waals diameter and the substrate spacing—is always in the range 1.3−1.7. Indeed, $(\sqrt{3} \times \sqrt{3})$R30° phases were commonly observed on fcc(111) surfaces for halogen adlayers under UHV conditions. The absence of the $(\sqrt{3} \times \sqrt{3})$R30° phase for electrochemically adsorbed halides is particularly noticeable on noble metal electrodes, where this structure is only found for Ag(111)−I,[56,123,174] Cu(111)−I,[185] and possibly Cu(111)−Cl.[31,184] For the Cu(111)−I system, the mismatch is particularly large, due to the small Cu lattice spacing, and actually close to $\sqrt{3}$; i.e., the $(\sqrt{3} \times \sqrt{3})$R30° structure corresponds already to an iodide adlayer at saturation density.[185] This is different for the other halide adlayers on Au(111), Ag(111), and Cu(111), which all have saturation packing densities that are considerably higher than those in the $(\sqrt{3} \times \sqrt{3})$R30° structure (see Table 1). Consequently, the $(\sqrt{3} \times \sqrt{3})$R30° structure in these systems corresponds to a more open arrangement of the adsorbates, which in electrochemical environment is apparently less favorable than a disordered, 2D liquidlike structure. To understand this phenomenon, we first consider the adlayer ordering in the limit of negligible substrate corrugation. In this case ordering is expected only above a critical adsorbate density (see below). For corrugated substrates the driving force for $(\sqrt{3} \times \sqrt{3})$R30° formation depends both on the effective adsorbate diameter, which is determined by the adsorbate−adsorbate interactions and which controls the intrinsic ordering of the adlayer, and on the corrugation amplitude, which determines the tendency of the adsorbates to lock in commensurate positions. Both of these factors could be substantially altered at the electrochemical interface as compared to the metal−vacuum interface, e.g., due to partial shielding by solvent molecules or due to the strong electric fields in the electrochemical double layer. In addition, dynamic effects, such as exchange with the solution, might enhance the tendency toward disordered or only locally ordered adlayers. These arguments also explain the observation of $(\sqrt{3} \times \sqrt{3})$R30° iodide phases on (111)-oriented electrode surfaces of the transition metals Pt,[37] Pd,[201] Rh,[203] and Ni.[204] First, these metals exhibit significantly smaller lattice spacings, resulting in a rather high packing density for the large iodide adsorbate, and second the substrate corrugation is more pro-

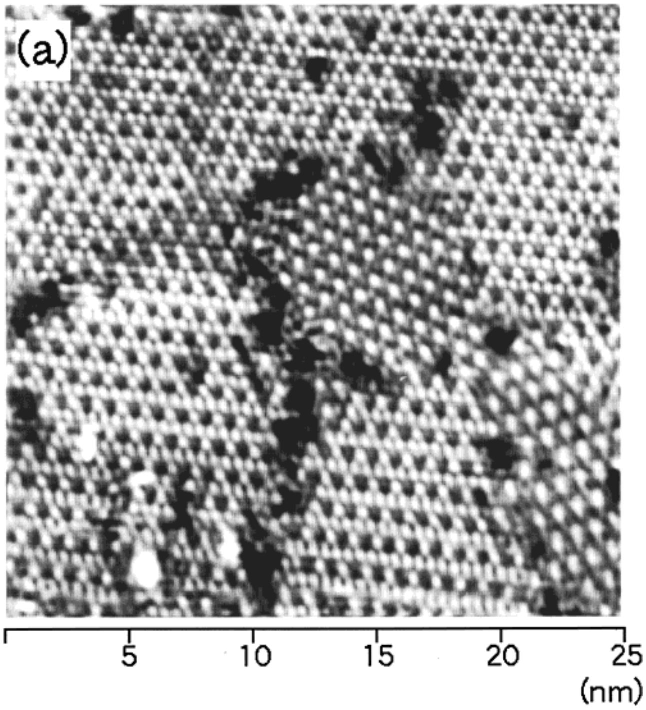

Figure 7. In situ STM image of the iodide adlayer on Pt(111) in 50 mM $H_2SO_4 + 1$ mM KI at 0.15 V versus RHE (250×250 Å^2), showing the coexistence of $(\sqrt{7} \times \sqrt{7})$R21.8° and (3×3) domains. (Reprinted with permission from ref 199. Copyright 1998 American Chemical Society.)

nounced, as indicated by the absence of incommensurate phases and the low mobility in the adlayer (see below).

Higher packing densities require an at least partial displacement of the adsorbates from the preferred hollow sites, resulting in high-order commensurate, incommensurate, or uniaxial-incommensurate structures. High-order commensurate phases, where a fraction of the adsorbates still occupies low-energy sites, are favored by large corrugation potentials and commonly observed for halides on transition metals, whereas incommensurate phases are preferred on substrates with weak corrugation potentials, in particular, noble metal surfaces. An exception is the formation of a high-order commensurate rather than an incommensurate, compressible Br adlayer on Ag(111), which was also observed for Br adlayers formed by gas-phase adsorption.[214] In view of the IC phases found for Cl and I on Ag(111), this behavior is currently not completely understood. The observation of unusually strong SXS peak intensities for Ag(111)–Br suggests that this structure may involve reconstruction of the Ag substrate[56] (see section VI.A) It is noteworthy that the potential-dependence of the adlattice spacing is difficult to study in this system, since the ordered adlayer is restricted to a small potential range of ≈50 mV negative to the onset of AgBr formation.

In contrast to the highly reversible adlayer phase behavior found on noble metal surfaces, the structure of halide adlayers on transition metal surfaces is strongly affected by kinetic effects. For example, studies of Pt(111)–I by SXS,[123,142] STM,[37,199] and ex situ methods[270,271] reported the coexistence of two high-order commensurate phases—a $(\sqrt{7} \times \sqrt{7})$R21.8° phase with $\theta = {}^3/_7$ and a (3×3) phase with $\theta = {}^4/_9$—over a wide potential range (Figure 7). As shown by Inukai et al.,[199] immersion of freshly prepared Pt(111) electrodes at negative or positive potentials results in an almost 100% coverage by the $(\sqrt{7} \times \sqrt{7})$R21.8° or (3×3) phase, respectively, but the phase transitions between these structures are apparently strongly hindered. The latter is probably caused by a pronounced corrugation potential for the iodide adsorbate on the Pt(111) surface, as indicated by the very low adsorbate mobility in this system and by the high defect density and small domain size, which are in strong contrast to the highly ordered halide adlayers found on Au and Ag surfaces.[199] Similar kinetic effects may explain the high-density disordered or poorly ordered adlayer phases of Cl and Br on Pt(111) observed by Lucas et al. using SXS[142] as well as the observation of different, coexisting (3×3) structures by Tanaka et al.[197] Furthermore, Müller et al.[204] found a pronounced hysteresis in potential for the formation and dissolution of the $(\sqrt{3} \times \sqrt{3})$R30° iodide adlayer phase on Ni(111). All these observations indicate that on transition metal surfaces the kinetics of adlayer formation strongly affects the potential-dependent halide adlayers structure, which causes severe problems in establishing the equilibrium phase behavior on these metals.

F. Potential-Dependent Structure of Incommensurate Adlayers on fcc (111) Surfaces

In the incommensurate phases the onset of ordering is determined by packing constraints in the adlayer, as illustrated in Table 2, where the lattice parameters of halides on Au(111), Ag(111), and Cu(111) obtained by diffraction techniques are summarized. For a better comparison of the different halide species, we additionally give the ratio of the lattice spacing a_X to the halide van der Waals diameter $a_{X,vdW}$ (obtained from crystallographic data on tetrahalides[208]), which was chosen somewhat arbitrarily as a measure of the intrinsic size of the halide adsorbates. Taking the halide size into account, all hexagonal-incommensurate phases as well as the only weakly distorted uniaxial-incommensurate phase of Br on Cu(111) form at similar packing densities, independent of whether the phase is formed in a disorder–order or a UIC–IC transition. More precisely, all transitions into IC phases occur at average nearest neighbor spacings $a_X(E_0)$, which are 13%–15% larger than $a_{X,vdW}$. This is in good agreement with Monte Carlo simulations of a two-dimensional system of particles interacting via a Lennard-Jones potential, where order–disorder transitions were found at average nearest neighbor spacings, which are 12%–19% larger than the van der Waals diameter.[244] For the formation of UIC phases with pronounced adlattice distortion, a wider range of critical adlayer densities $a_X(E_0)$ is found. This is expected, since the structure is in this case not only determined by packing constraints but also by the strength of the corrugation potential.

The symmetry of the incommensurate phase (UIC or hexagonal) is controlled by the competing contributions of the interface energy and the elastic energy associated with the distortion of the hexagonal lattice (see above). Uniaxial-incommensurate structures are only stable if the distortions are below a critical limit and consequently should only be observed if the mismatch between the commensurate spacing $\sqrt{3}a_{\mathrm{Me}}$ and the intrinsic diameter of the halide adsorbate is sufficiently small at the onset of ordering. This is supported by the structural data (see Table 2), according to which uniaxial-incommensurate phases are only observed below a critical ratio $\sqrt{3}a_{\mathrm{Me}}/a_{\mathrm{X,vdW}}$, whereas at higher ratios the disordered adlayer orders directly in the hexagonal-incommensurate structure. With the above choice of $a_{\mathrm{X,vdW}}$ this critical ratio is $\sqrt{1.3}$, which may provide a rule of thumb for estimating the adlayer structure. Using this criterion, a direct disorder-IC transition would also be expected for Cl and Br on Pt(111). Indeed, the series of HOC phases found for Pt(111)−Br[142,194,197,257] and the close-packed, disordered adlayer structure for Pt(111)−Cl[142] may be understood as frustrated IC phases, where the pronounced corrugation potential enforces the local occupation of commensurate sites and a continuous electrocompression in the form of a well-ordered adlattice is kinetically hindered (see below). The transition of the UIC iodide adlayer phases on Au(111) and Ag(111) to a hexagonal IC structure can be explained by similar packing constraints in the adlayer: it occurs on both surfaces at an adlayer density where the iodide nearest neighbor spacing in the UIC $c(p \times \sqrt{3})$ phase is identical to the minimum spacing $a_{\mathrm{X}}(E_{\max})$ in the IC phase.[122,123,176] In a simple physical picture, the adsorbates are expelled from the rows defined by the substrate atoms due to the hard-core repulsion of the ions.

The orientation of the adlayer in the hexagonal-incommensurate phase exhibits a complex behavior, which is not fully understood. The adlayer is either aligned with the $[11\bar{2}]$ direction of the substrate, i.e., has the same orientation as the commensurate $(\sqrt{3} \times \sqrt{3})$R30° phase (Au(111)−Cl[46] and Ag(111)−Cl[56]), or is rotated relative to this direction by an angle $\phi < 5°$, which continuously varies with the adlayer density (Au(111)−Br[46,55], Au(111)−I,[122] and Ag(111)−I[56]). This epitaxial rotation is a well-known phenomenon in adlayer systems and heteroepitaxial growth[246,258,259] and was first studied theoretically by Novaco and McTague.[260,261] They showed that for an infinite incommensurate adlayer a rotation from a high-symmetry, commensurate orientation is energetically preferred if the transverse strain in the adlayer is sufficiently lower than the longitudinal strain. In this case the total adlayer energy is minimized at a nonzero angle due to the presence of periodic lateral distortions of the adsorbate lattice ("static distortion waves"). The Novaco−McTague theory predicts an analytical relationship between the rotation angle ϕ and the incommensurability $\epsilon = \sqrt{3}\theta$ in the rotated hexagonal phase, which is approximately linear for moderate misfits and which can be used to determine the ratio of transverse to longitudinal sound velocities c_t/c_l. An alternative model based on finite-size effects was proposed by Grey and Bohr.[262] Assuming that the adlayer islands have energetically preferred edges along high-symmetry directions, the adlayer orientation can be explained by a simple symmetry principle. Both models provide reasonable descriptions of the rotation of the iodide adlayers on Au(111)[122] and Ag(111).[56] They can also account for the presence of aligned-hexagonal structures for Au(111)−Cl and Ag(111)−Cl, which in the framework of the Novaco−McTague theory indicate a ratio $c_t/c_l < 1.35$ in these adlayers.[260,261] In contrast, both models fail to explain the rotation of the Br adlayer on Au(111), where ϕ decreases with ϵ and depends on halide concentration and the history of the potential changes.[46] This behavior, as well as other more complex phenomena, e.g., the coexistence of two rotated phases with a difference in ϕ of 0.2° for Au(111)−I,[122] may be attributed to a crossover between different contributions (i.e., finite-size or elastic distortion effects) or to the influence of surface heterogeneities, such as impurities or substrate steps. In general, the adlayer energy as a function of rotation angle ϕ exhibits only weak, broad minima,[261,262] so that the adlayer orientation is easily affected by kinetic effects.

The phase behavior of halide adlayers closely resembles that of adlayers formed by physisorbed rare gases[246,263−265] as well as alkali metals[258] on substrate surfaces with hexagonal symmetry. In particular, the same phase sequence as for the Ag(111)−I phase was observed by Kern et al. for Xe adlayers on Pt(111) using He diffraction.[265] This illustrates that major aspects of the general adlayer phase behavior can be understood solely from geometrical constraints and the relative strength of the adsorbate−adsorbate and adsorbate−substrate interaction, independent of the chemical nature of the system. On the other hand, the chemical interactions in the adlayer have a pronounced influence on physical properties such as the two-dimensional compressibility. Accordingly, the electrocompression of the halide adlayers is a function of halide species, substrate, and adlayer phase (see Table 2). The lateral compressibility $\kappa_{2\mathrm{D}}$ of the adlayer can be calculated via $\kappa_{2\mathrm{D}} = (\gamma e_0)^{-1}\ \partial A/\partial E$, where γ is the electrosorption valency and $A = \Gamma^{-1}$ the area per iodide adsorbate.[122,266−268] From the diffraction data halide adlayer compressibilities in the range 1.8−6.9 and 4.47−9.4 Å^2 eV^{-1} are obtained for the UIC and the IC phases, respectively, assuming an electrosorption valency $\gamma = -1$. This is higher than the compressibility of electrochemically deposited metallic monolayers ($\kappa_{2\mathrm{D}} \approx 1−2$ Å^2 eV^{-1} [266−268]) but significantly lower than that of physisorbed noble gas adlayers ($\kappa_{2\mathrm{D}} \approx 10−30$ Å^2 eV^{-1} [246,263−265]).

Up to now only a few attempt have been made to quantitatively describe the electrocompression of the halide adlayers. In comparison to metal and noble gas adlayers, where the compressibility can be explained by the free-electron model[266−268] and models employing Lennard-Jones pair potentials,[263,264] respectively, the halide−halide interaction is considerably more complex and consequently cannot be described by these simple models.[55,122] Ocko and Wandlowski[176] proposed a model where Lennard-Jones and repulsive dipole−dipole interactions were considered and found that the experimental data could only be described by assuming unreasonably high dipole moments. More recently, Wang et al.[269] presented a more detailed physical model for the electrocompression of halides on Au(111). Here substrate-mediated indirect interactions, electrostatic interactions, Lennard-Jones interactions, interactions between the induced dipole moments, and nonadditive three-body interactions were taken into account by employing empirical approximations. The calculated $\theta(E)$ curves were in reasonable agreement with the experimental data. According to this study the lateral interactions in the halide adlayer are strongly repulsive and dominated by the substrate-mediated interaction.

G. Halide Adlayer Phases on fcc (100) Surfaces

On the (100) and (110) surfaces of the fcc metals the symmetry of the substrate differs from the intrinsic symmetry of the halide adlayers. Following the reasoning of the previous section, the adlayer should adopt the substrate symmetry if the adsorbate–metal interactions are dominant, i.e., the corrugation potential is high, whereas a hexagonal packing should be favored if the adsorbate–adsorbate interactions are dominant. We will first consider halide adlayers on (100) surfaces, where the lattice is square and the preferred adsorption sites are the four-fold hollow sites. Due to the higher coordination, halide adsorbates are more strongly bound in these sites than in the three-fold hollow sites on (111) surfaces, whereas the adsorption energy on bridge sites should be similar on both surfaces. Consequently, the corrugation potential is enhanced on (100) as compared to (111) surfaces, promoting the formation of simple commensurate structures. For halide adlayers in an electrochemical environment, the only stable low-order commensurate phase is the $c(2 \times 2)$ structure (Figure 8a), which was found on all studied (100) metal surfaces but Au(100).[113,175−177,179,181−183,186−189,192,201,202] Commensurate phases with lower adlayer density, such as primitive (2×2) or $c(2 \times 4)$ phases with $\theta = {}^1/_4$, were never observed at the electrochemical interface and only rarely reported in studies under UHV conditions.[243] As indicated by theoretical studies,[272,273] ordering in these low-density phases would only be possible at low temperatures, whereas at room temperature it is prevented due to entropic effects. The $c(2 \times 2)$ structure, on the other hand, corresponds to a high halide density and in fact for many halide–metal systems to a close-packed adlayer. This is a consequence of the halide–metal lattice mismatch, which is typically close to $\sqrt{2}$ for the studied systems. Furthermore, the smaller halides Cl^- and Br^-, where the adlayer density in the $c(2 \times 2)$ phase can be up to 20% below the saturation value (as estimated from the maximum density on the corresponding (111) surface), experience a higher corrugation potential,[86] which favors commensurate ordering. Hence, the abundance of $c(2 \times 2)$ halide adlayer phases on (100) surfaces is not surprising.

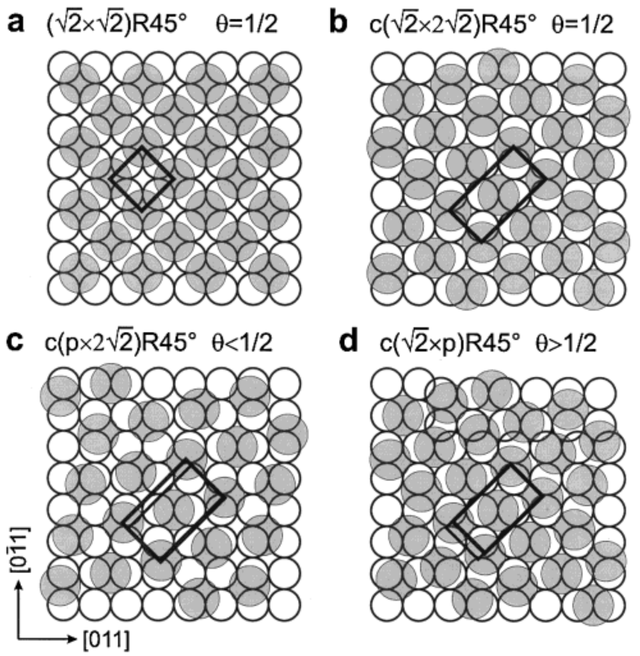

Figure 8. Adlayer phases on (100) surfaces. (a) $(\sqrt{2} \times \sqrt{2})$-R45° or $c(2 \times 2)$, (b) $c(\sqrt{2} \times 2\sqrt{2})$R45°, (c) $c(p \times 2\sqrt{2})$R45°, and (d) $c(\sqrt{2} \times p)$R45° structures. The adlayer unit cells are indicated by thick solid lines; for parts c and d, also the $c(\sqrt{2} \times 2\sqrt{2})$R45° unit cell is indicated for comparison (thin solid line).

Although the commensurate $c(2 \times 2)$ phase, where all adsorbates can occupy the preferred hollow sites, minimizes the interface energy between halide adlayer and metal, the resulting square adlattice is energetically unfavorable in terms of the adsorbate–adsorbate interactions. A prime example for illustrating the competing contributions of lateral interactions and corrugation potential is halide adlayers on the structurally isomorphic Au(100) and Ag(100) surfaces, which were studied in detail by Ocko et al. using in situ SXS.[164,168,175,175,176] On Ag(100) the $c(2 \times 2)$ structure is the only ordered adlayer phase formed by Cl, Br, and I.[175−177] In contrast, at the same coverage $\theta = {}^1/_2$ a more isotropic, quasihexagonal $c(\sqrt{2} \times 2\sqrt{2})$R45° structure is found for all three halides on Au(100) (Figure 8b).[160,164,165,168,169,176] The $c(\sqrt{2} \times 2\sqrt{2})$R45° structure can be obtained from the $c(2 \times 2)$ structure by antiphase shifting of the of the adsorbate rows along the [001] direction (i.e., every second row is shifted by $\sqrt{2}a_{Me}$), which results in a slightly distorted hexagonal arrangement of the halide adsorbates. These structural differences indicate that the corrugation potential for halides on Au(100) is weaker than on Ag(100), resulting in an adlayer structure dominated by the repulsive interactions between the halide adsorbates. Similar trends were found for halide adlayers on Au(111) and Ag(111) (see section III.D), as well as in the corrugation potentials extracted from the calculations of Ignaczak and Gomes.[86] A crystallographic analysis of the X-ray peak intensities[164,165] suggests a registry of the $c(\sqrt{2} \times 2\sqrt{2})$R45° adlayer as in Figure 8b, where all adsorbates reside in bridge sites, rather than the alternative possibility of a mixed occupation of top and hollow sites (obtained by shifting the adlayer in Figure 8b by $a_{Me}/2$ in the [011] direction). This is also supported by the in situ STM studies by Gao et al. [160] and Cuesta and Kolb,[169] where no differences in the apparent height of the two halide adsorbates in the $c(\sqrt{2} \times 2\sqrt{2})$R45° unit cell were observed.

The lateral elastic energy of the adlayer can be further lowered by reducing the residual distortion present in the $c(\sqrt{2} \times 2\sqrt{2})$R45° phase. This is possible either by a uniaxial expansion of the adlayer along the "$\sqrt{2}$" direction, resulting in a $c(p \times 2\sqrt{2})$R45° structure (Figure 8c), or by a uniaxial compression along the "$2\sqrt{2}$" direction, corresponding to a $c(\sqrt{2} \times p)$R45° structure (Figure 8d). In both of these uniaxial-incommensurate structures, the halide adatoms reside on the rails of the substrate lattice defined by the bridge sites, i.e., between the bridge and hollow sites. It is likely that the adatoms are not perfectly aligned with these rails but are locally distorted toward the hollow sites. Since the interface energies in these phases should be comparable to that in the $c(\sqrt{2} \times 2\sqrt{2})$R45° phase, the $c(p \times 2\sqrt{2})$R45° or $c(\sqrt{2} \times p)$R45° structure should be energetically favorable for halide coverages below or above $^1/_2$, respectively.

The transition from the $c(\sqrt{2} \times 2\sqrt{2})$R45° to the more densely packed $c(\sqrt{2} \times p)$R45° phase is observed for the two smaller halides, Cl and Br.[123,164,165,168,169] As on Au(111), the disorder–order and the transitions between the two ordered phases manifest in sharp spikes in the voltammograms. This is illustrated in Figure 9a for the case of Br. Also shown is the corresponding potential-dependent intensity of one of the first-order $c(\sqrt{2} \times 2\sqrt{2})$R45° diffraction peaks, which visualizes the good agreement between the peaks and the formation (peak P2) and disappearance (peak P3) of the $c(\sqrt{2} \times 2\sqrt{2})$R45° phase (peak P1 results from the lifting of the Au reconstruction). A more detailed discussion of the $c(\sqrt{2} \times 2\sqrt{2})\text{R45°} \rightarrow c(\sqrt{2} \times p)$R45° transition is given in section III.I.

The potential-dependent phase behavior and coverage of halide adlayers on Au(100) is summarized in Figure 9b. In the $c(\sqrt{2} \times p)$R45° phase the incommensurability $\epsilon = 2\sqrt{2}/p - 1$ continuously varies from 0 (commensurate $c(\sqrt{2} \times 2\sqrt{2})$R45° phase) to 0.13 and 0.15 for Au(100)–Br and Au(100)–Cl, respectively, at the upper end of the double layer potential regime. Accordingly, the coverage $\theta = \sqrt{2}/p$ increases from $^1/_2$ to about 0.565 and 0.575, respectively (Figure 9b). The nearest neighbor spacing in the $c(\sqrt{2} \times p)$R45° structure is always the commensurate spacing $\sqrt{2}a_{\text{Me}} = 4.078$ Å; however, the next-nearest neighbor spacing decreases from 4.56 Å in the commensurate phase to 4.14 Å for Br and 4.09 Å for Cl, resulting in an almost undistorted hexagonal lattice at the most positive potentials. For both halides, the adlayer electrocompressibilities in the $c(\sqrt{2} \times p)$R45° phase at incommensurabilities $\epsilon > 0.07$, i.e., far away from the $c(\sqrt{2} \times 2\sqrt{2})\text{R45°} \leftrightarrow c(\sqrt{2} \times p)$R45° phase transition, are similar to that in the rotated-hexagonal phases on Au(111),[123] suggesting that the halide–substrate interactions are similar on both surfaces, despite the different substrate symmetry. This supports our view that the halide compressibilities are largely determined by the adsorbate–adsorbate interactions. As for the incommensurate phases on (111) surfaces, the absence of satellite peaks in the SXS data indicates a uniformly compressed adlayer rather than a domain-wall structure.

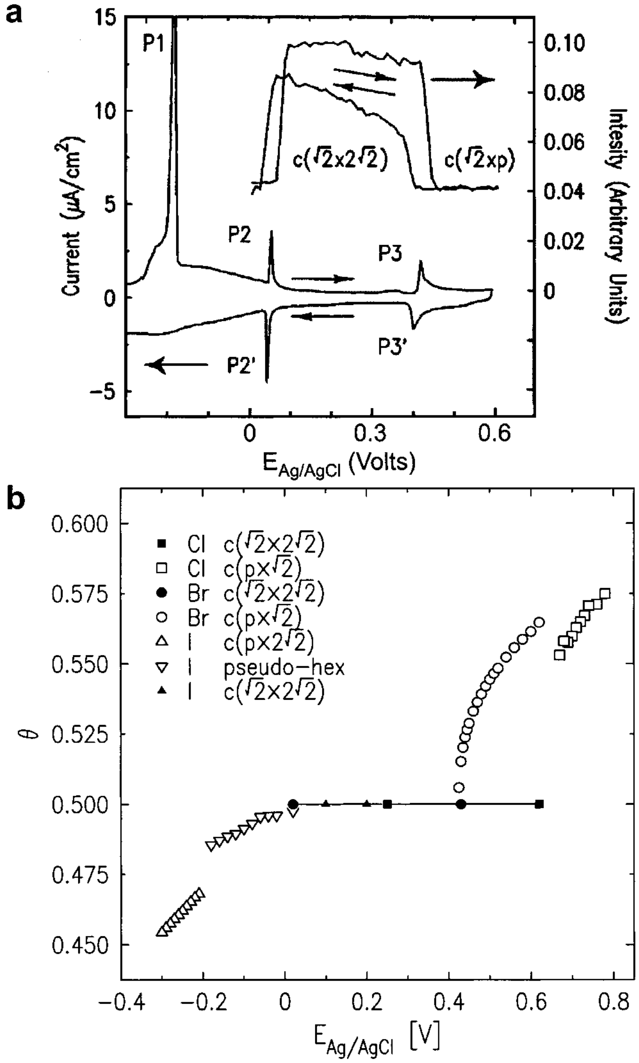

Figure 9. (a) Cyclic voltammogram (10 mV/s) and corresponding X-ray intensity at (0,1) versus potential curve (inset, 1 mV/s) of Au(100) in 50 mM NaBr (reprinted with permission from ref 164. Copyright 1996 American Physical Society). (b) The potential-dependence of the halide coverage θ on Au(100) obtained from in situ SXS data in 50 mM NaCl (circles), NaBr (squares), and NaI (triangles).[168] For the $c(\sqrt{2} \times 2\sqrt{2})$R45° phase, where the $\theta(E)$ curves of the different halide species overlap, the symbols mark the upper and lower limit of the potential regime.

A different phase behavior is found for iodide on Au(100), where the first ordered phase observed by STM[160] and SXS[168] upon increasing the potential from the regime of the disordered adlayer is a $c(p \times 2\sqrt{2})$R45° structure. This phase has an initial value of $p = 1.554$, corresponding to a coverage $\theta = 1/\sqrt{2}p = 0.455$ (see Figure 9b), an incommensurability $\epsilon = \sqrt{2}p - 1 = -0.090$, and nearest and next-nearest neighbor spacings of 4.48 and 4.66 Å. Hence, this phase is close to a hexagonal adlattice and considerably less distorted than the $c(\sqrt{2} \times 2\sqrt{2})$R45° phase. In accordance with the arguments presented above, the presence of the $c(p \times 2\sqrt{2})$R45° structure for Au(100)–I can be attributed to the structure-determining role of the adsorbate−adsorbate interactions and the larger size of the adsorbate, which promotes ordering at $\theta < {}^1/_2$. With increasing potential, the $c(p \times 2\sqrt{2})$R45° is uniaxially compressed, resulting in an increasing lattice distortion. In this potential range discrepancies between the STM and the SXS data concerning the adlayer phase behavior exist. According to the STM results by Gao et al.,[160] the adlayer is continuously compressed until the $c(\sqrt{2} \times 2\sqrt{2})$R45° phase is approached. Upon further potential increase, a pseudohexagonal phase emerges, where the adlayer is rotated by an angle $\phi \approx 5°$ from the "$\sqrt{2}$" direction. In contrast, in the SXS study by Wang et al.[168] the $c(p \times 2\sqrt{2})$R45° phase is only found down to $p = 1.511$ ($\theta = 0.468$), where the halide adlattice spacings are 4.36 and 4.63 Å, and then is replaced in a first-order phase transition by a rotated pseudohexagonal phase with an initial coverage $\theta = 0.485$ (see Figure 9b), rotation angle $\phi = 3.5°$, and adlattice spacings of 4.35 and 4.54 Å. The diffraction peaks in the quasihexagonal phase change continuously and finally approach the peak positions of the commensurate $c(\sqrt{2} \times 2\sqrt{2})$R45° phase. Interestingly, both the STM and the SXS data indicate that the quasihexagonal phase is a domain wall structure. This is evidenced by the observation of a rather regular arrangement of domain walls oriented along well-defined directions in the STM images (Figure 10a) as well as by the presence of satellite peaks in the SXS scans (Figure 10b). Hence, the results of STM and SXS are in agreement with the exception of the differences in the potential regime of the adlayer phases. The latter may result from coexistence of the quasihexagonal and the $c(\sqrt{2} \times 2\sqrt{2})$R45° phases over a wider potential range due to kinetic hindrance of the phase transition, an effect that has been observed for a number of iodide adlayer systems (see section III.F).

Apart from the phases on Au(100), only few halide adlayer structures different from the $c(2 \times 2)$ phase were reported up to now. The best studied example is the $c(\sqrt{2} \times 5\sqrt{2})$R45° phase found in ex situ LEED studies by Wieckowski et al.[274] and Lu et al.[275] and in in situ STM studies by Vitus et al.[189] and Vogel et al.[48,190−192] for Pt(100)−I, prepared by cooling of annealed Pt crystals in iodine vapor. This structure, which can be rationalized as a $c(\sqrt{2} \times p)$R45° phase with $p = 5\sqrt{2}/3$, exhibits a surprisingly small nearest neighbor spacing of $a_\mathrm{I} = 3.81$ Å, which is smaller than the iodine van der Waals diameter. Possible explanations for this are a reduced effective diameter of iodine on Pt as compared to noble metal surfaces, due to the less ionic bond and correspondingly smaller surface dipole[87] as well as a pronounced buckling of the adlayer, as indeed indicated by the STM observations.[48,189−192] It should be noted that the $c(\sqrt{2} \times 5\sqrt{2})$R45° phase is only obtained by gas-phase dosing at elevated temperatures, whereas adlayers formed by electrochemical adsorption are apparently disordered and have about 30% smaller saturation coverages.[276] Furthermore, for Pt(100)−Br, ex situ STM studies by Bittner et al.[194] and Orts et al.[277] and in situ SXS results by Markovic[141] indicate densely packed, disordered adlayers with a locally quasihexagonal arrangement of the adsorbates. Analogous to the discussion of the halide adlayers on Pt(111), this behavior can be rationalized by kinetic limitations caused by the pronounced corrugation potential.

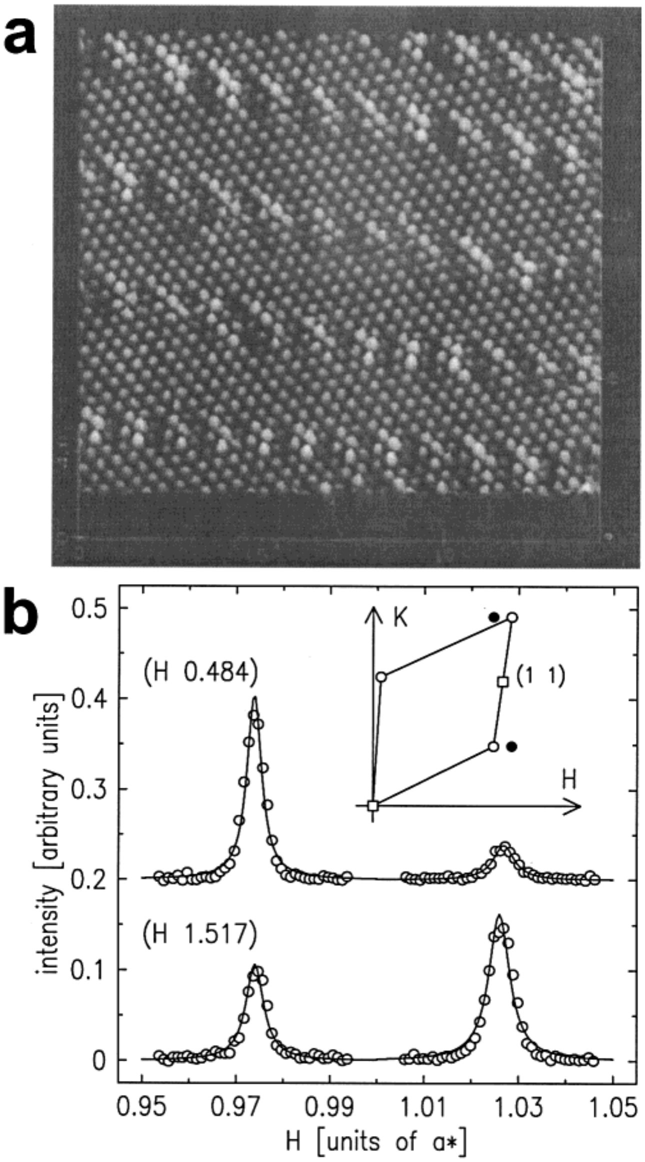

Figure 10. Structure of the rotated pseudohexagonal iodide adlayer on Au(100). (a) In situ STM image recorded at 0.2 V_{SCE} in 10 mM KI showing the domain wall structure (reprinted from ref 160. Copyright 1994 American Chemical Society). (b) X-ray diffraction pattern and SXS scans through the peaks at $(1 \pm \Delta H, {}^1/_2 - \Delta K)$ obtained at −0.1 $V_{Ag/AgCl}$ in 50 mM NaI.[168] In the diffraction pattern substrate peaks (open squares), first- and second-order adlattice peaks (open circles) and satellite peaks (closed circles), as well as the unit cell (solid line), are indicated (for clarity only one domain of the adlayer is shown).

H. Halide Adlayer Phases on fcc (110) Surfaces

We now turn to the discussion of halide adlayer phases on (110) surfaces, where only a few selected systems have been studied so far. On this surface the corrugation potential is highly asymmetric, with a very weak corrugation along the atomic rails in the $[1\bar{1}0]$ direction but a high corrugation in the perpendicular [001] direction. Consequently, adlayer struc-

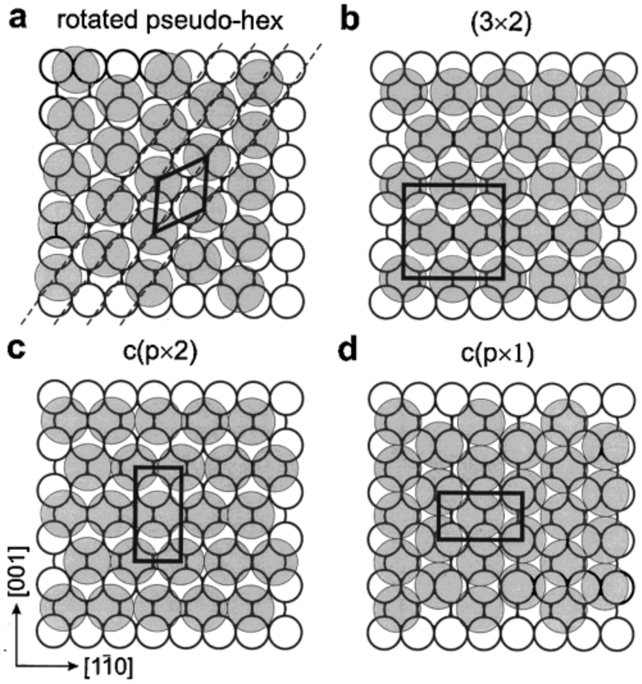

Figure 11. Iodide adlayer phases on Au(110) surfaces: (a) rotated pseudohexagonal, (b) (3 × 2), (c) $c(p \times 2)$, and (d) $c(p \times 1)$ structure. (Adapted from refs 161 and 167.)

tures should be preferred where the adsorbates reside in the atomic rails, in particular since the spacing between these rails ($\sqrt{2}a_{Me}$) is in good agreement with the intrinsic size of the halides.

Again, the most complex phase behavior is found on Au electrodes, as shown in extensive in situ studies of Au(110)−I by Gao and Weaver using STM[161,278,279] and Wang et al. using SXS.[166,167] Here, ordered phases were observed at potentials as negative as −0.6 V vs Ag/AgCl (in 10 mM KI), which were attributed to the formation of mixed alkali−halide adlayers and are discussed in section V. The formation of purely anionic, ordered adlayers commences at ≈300 mV more positive potentials, where a rotated pseudohexagonal structure with nearest and next-nearest neighbor spacings of 4.6−4.4 and 4.7 Å is observed (Figure 11a).[161,167] According to the SXS data, the iodide adsorbates in this phase are arranged along the rows in the [1$\bar{1}$2] direction defined by the bridge sites of the substrate (indicated in Figure 11a by dashed lines), which allows the adsorbates to avoid the unfavorable top sites. Along these rows the adsorbates occupy alternately sites on top and between the atomic rails of the substrate, in good agreement with the height modulation observed in the STM images.[161] With increasing potential, the adlayer is uniaxially compressed along the [1$\bar{1}$2] direction. This behavior resembles the uniaxial-incommensurate phases on Au(100); however, due to the different adsorbate spacing along the major directions of the indicated primitive unit cell (solid lines), the pseudohexagonal adlayer on Au(110) cannot be described by a centered-rectangular structure. A true centered-rectangular structure, where the adsorbates are aligned with the atomic rails of the substrate, emerges upon further potential increase. This phase was first attributed by STM to a commensurate (3 × 2) structure (Figure 11b)[161] but later identified by SXS as a uniaxial-incommensurate $c(p \times 2)$ phase, with a potential-dependent nearest neighbor spacing pa_{Me} between 4.2 and 4.08 Å.[167] At even more positive potentials (0.05 V vs Ag/AgCl in 10 mM KI), a second uniaxial-incommensurate phase—a $c(p \times 1)$ structure (Figure 11d)—is found by SXS, which exhibits an even higher iodide packing density and a much smaller distortion with respect to a hexagonal adlattice than the $c(p \times 2)$ phase.[167] The STM images show in the same potential regime the formation of periodic, stringlike features, which are rotated by ≈30° relative to the [1$\bar{1}$0] direction,[161] i.e., oriented parallel to one of the close-packed directions in the $c(p \times 1)$ structure (see Figure 11d). This suggests that these strings are connected with the $c(p \times 1)$ phase, although the adlayer structure within the strings could not be resolved. Even at very low potential scan rates, the pseudohexagonal and the $c(p \times 2)$ phase as well as the $c(p \times 2)$ and the $c(p \times 1)$ phase coexist over a wide potential range, indicating that the (first-order) phase transitions between these phases are strongly kinetically hindered.[167]

For Au(110)−Br, very different structures were recently reported in an in situ STM study by Zou et al.[170] In contrast to the (quasi)hexagonal iodide adlayers, a (3 × 1) and, at more positive potentials, a (4 × 1) superstructure with a rectangular atomic arrangement are commonly observed, where the bromide adsorbates are located in the substrate atomic rails along the [1$\bar{1}$0] direction and aligned in form of close-packed rows in the perpendicular [001] direction. This structural difference was attributed to the different adsorbate diameter, which for Br (but not for I) is slightly smaller than the substrate lattice distance along [001] and therefore allows this type of arrangement. The minimum Br nearest neighbor spacing is 3.85 Å, i.e., smaller than on Au(111) and Au(100), which can be rationalized by the higher coordination of the adsorbate with Au substrate atoms on the (110) surface. Parallel to the rectangular structure also a pseudohexagonal (4 × 1) structure was found, where the close-packed rows along [001] are maintained but rotated by ≈20° from the [1$\bar{1}$0] axis. Apparently, the more unfavorable adsorbate−substrate interaction in this arrangement can be compensated by the less pronounced lateral repulsion, resulting from the larger adsorbate−adsorbate spacing.

Structural studies of halide adlayers on other fcc(110) electrode surfaces currently exist only for Cu and Pt substrates. In situ AFM observations of Cu(110)−Cl by LaGraff and Gewirth[180] found a close-packed, quasihexagonal adlattice, resembling the $c(p \times 1)$ structure. More recently, in situ STM results on the halide adlayer structure on Cu(110) were reported by Wan et al.[280] as well as Li et al.[281] For Cu(110)−Cl, the authors observed a (4 × 1)[280,281] and a (5 × 1) phase[281] with a very similar arrangement of the adsorbates as that reported by LaGraff and Gewirth;[180] however, Wan et al. suggested on the basis of the height modulation in the STM images a different structure, involving a Cl-induced reconstruction with a Cu coverage of $^{1}/_{2}$ in the topmost Cu layer[280] (see section VI.A). At more negative potentials, the adlayer disordered and the (1 × 1) lattice of the Cu(110) surface was observed.[280,281] For Br and I adlayers on Cu(110) $c(2 \times 2)$ phases were found.[280] In the few studies of halide adlayers on Pt(110), the observed adlayers were usually more disordered, similar to Pt(111) surfaces. For Pt(110)−I, ex situ LEED and in situ STM studies by Bittner et al.,[195] Albers,[276] and DeSimone[196] reported structures where the adsorbates were occupying the substrate rails and exhibited a (4 × 1)[195,276] or (2 × 1)[196] symmetry. STM observations of bromide adlayer on Pt(110) by Bittner et al.[194] and Orts et al.[200] indicated a 2- or 3-fold periodicity in [001] and a 6- or 7-fold periodicity in [1$\bar{1}$0] direction and were interpreted in terms of a distorted hexagonal structure.

Finally, it is noteworthy that on Au electrodes, where the adlayer structure is least constrained by commensurate effects, the surface concentrations $\Gamma(E)$ of bromide and iodide adlayers on the three low-index surfaces are almost identical, if the differences in pzc are taken into account.[123,160,167,176] In addition, also the values of the electrocompression in the incommensurate phases are very similar and the onset of adlayer ordering occurs within 5% at the same surface concentration $\Gamma(E)$, indicating that it is largely governed by packing constraints. Hence, the lateral adsorbate−adsorbate interactions are—at least at these high adlayer densities—apparently identical on all three surfaces and only weakly affected by the substrate symmetry.

I. Phase Transitions in Halide Adlayers

Adlayers at electrochemical interfaces are interesting model systems for the study of two-dimensional phase transitions, since the chemical potential of the adsorbate can be directly controlled through the applied electrode potential. On well-defined, smooth single crystal electrodes, these transitions in the adlayer usually manifest as sharp spikes in the cyclic voltammograms and double layer capacity, which can be rationalized by the corresponding changes in anion coverage and double layer structure. In general, the hysteresis between the transition potentials obtained in the anodic and the cathodic potential scans is small ($\leq$ 30 mV), indicating that the transitions occur close to equilibrium. The hysteresis in the voltammograms and in the SXS measurements, where much lower potential sweep rates are used, is similar and apparently an intrinsic property of the system, possibly resulting from pinning effects or changes in the substrate morphology. Even larger hysteresis is typically observed in nonelectrochemical systems. Most of the phase transitions between ordered halide adlayers are first-order, i.e., involve phase coexistence and proceed via a nucleation and growth mechanism. More interesting from the point of view of statistical mechanics are second-order phase transitions, which can be described by a continuous order parameter and exhibit universality, i.e., the critical behavior is determined solely by symmetry and dimensionality. In the following we will consider two examples of such continuous phase transitions: the disorder−order transition for Ag(100)−Br and the C−UIC transition for Au(100)−Br.

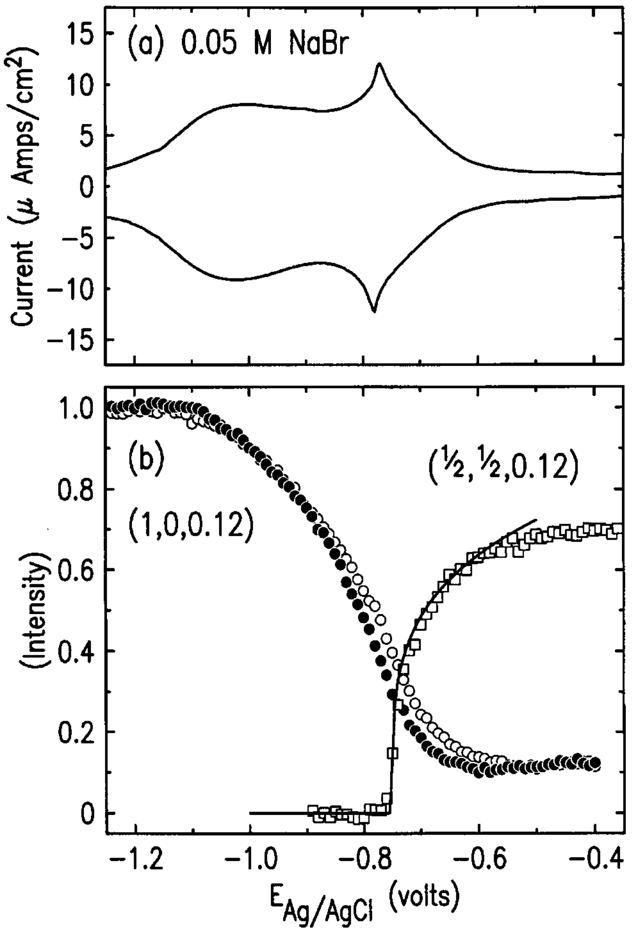

Figure 12. (a) Cyclic voltammogram (10 mV/s) and (b) background-subtracted, normalized X-ray intensity at ($^{1}/_{2}$, $^{1}/_{2}$, 0.12) and (1, 0, 0.12) (1 mV/s) for Ag(100) in 50 mM NaBr. The solid line is a power-law fit to the ($^{1}/_{2}$, $^{1}/_{2}$, 0.12) signal with exponent $2\beta = 0.25$. (Reprinted with permission from ref 175. Copyright 1997 American Physical Society.)

The disorder−order transition in an adsorbate layer corresponds to the formation of a phase with long-range positional order from one with short-range order. For weak substrate corrugation potentials, the disordered phase is close to an ideal two-dimensional liquid, and the onset of order occurs at a critical average adatom distance a_X (see section III.F). In this case the transition can be described by the Kosterlitz−Thouless theory of melting or related models.[244,248,282] In contrast, for pronounced corrugation potentials, the disordered phase is described by a lattice gas, where the adsorbates occupy preferred sites on the substrate. A particular simple and well-studied case is order−disorder transitions in lattice gas systems on square substrates, which are isomorphic to the two-dimensional Ising spin model.[247] Recently, Ocko et al.[113,175] demonstrated in a combined study by in situ SXS and electrochemical measurements the existence of a lattice gas phase for Br on Ag(100) and an Ising behavior for the disorder−order transition into the $c(2 \times 2)$ phase. In Figure 12 the cyclic voltammogram, the potential-dependent X-ray intensity at ($^{1}/_{2}$, $^{1}/_{2}$, 0.12), i.e., at the first-order diffraction peak of the $c(2 \times 2)$ phase, and the intensity at (1, 0, 0.12), which reflects the occupation of the four-fold hollow sites of the Ag substrate, are reproduced. Obviously, the position of the sharp peak in the voltammogram at −0.76 V correlates well with the onset of $c(2 \times 2)$ order. For potentials >-0.76 V, the intensity at ($^1/_2$, $^1/_2$, 0.12), which measures the order parameter squared,[247] increases according to $(E - E_c)^{2\beta}$ with the critical exponent $\beta = {}^1/_8$, in agreement with the predictions of the Ising model. The same power law behavior was found for Ag(100)−Cl, both in an electrochemical environment[113,175] and under UHV conditions, where the chemical potential was inferred from the coverage.[220] The intensity at (1, 0, 0.12) slowly decreases between −1.2 and −0.6 V, i.e., in the potential range of the broad adsorption peak in the voltammogram. Its continuous variation even in the range of the phase transition indicates a continuous change in coverage, supportive of a second-order transition. Comparison of the Br coverage in hollow sites θ_x obtained from the SXS data with the total coverage θ_e from parallel chronocoulometric measurements revealed a good agreement in the fully ordered adlayer, but lower values of θ_x at intermediate coverages, which was attributed to significant lateral displacement of the adsorbates from the hollow sites at low coverages.[175] Interestingly, recent surface resistance measurements of Br adsorption on Ag(100) thin film electrodes by Hanewinkel et al.[283] observed a similar potential dependence as that of θ_x. To explain this behavior, it was assumed that only bromide in the hollow sites exchange electrons with the substrate. The order−disorder transition occurs at $\theta_x = 0.25$ and $\theta_e = 0.35$,[175] with the latter value being in good agreement with the critical coverage of 0.368 obtained from simulations[284,285] and comparable to that of 0.394 found for Ag(100)−Cl under UHV conditions.[220,222] In addition, Ocko et al. estimated a repulsive interaction energy of 110 meV between Br adsorbates on next-nearest neighbor sites from the adsorption isotherm using a mean field approximation.[175] A more detailed treatment was provided by Koper[101] and Mitchell et al.,[273,286] who performed Monte Carlo simulations for a lattice gas model. From fits of the Ag(100)−Br adsorption isotherm it was concluded that the dominant contribution is the long-range electrostatic interaction but that also additional short-range repulsion between nearest neighbor sites has to be included. These simulations quantitatively reproduced the electrochemical data and provided an excellent description of the critical properties of this phase transition.

As a second example we discuss the transition between the commensurate $c(\sqrt{2} \times 2\sqrt{2})$R45° and the uniaxial-incommensurate $c(\sqrt{2} \times p)$R45° phase in the bromide adlayer on Au(100).[164,165] Here the order parameter is the incommensurability $\epsilon = 2\sqrt{2}/p - 1$, which increases continuously from zero in the phase transition (Figure 13b). The data are well-described by a power law with an exponent $\beta = 0.4$ (dashed and solid lines). The electrochemical current can be approximated as $i = i_0(E - E_c)^{\beta-1} + i_1$, where the first term reflects the change in Br coverage and the second a constant capacitive double layer charging, which provides an excellent fit (solid line) to the unusual, asymmetric shape of the corresponding peak in the voltammogram (Figure 13a). The measured exponent $\beta = 0.4$ is smaller than the theoretical value of $\beta = {}^1/_2$, predicted by Pokrofsky and Talapov[287] within a domain wall model. This model, however, should only be valid for small ϵ, where the domain walls are well-separated. Unfortunately, the experimental precision is too low to quantitatively extract the exponent close to the transition. Indeed, a good fit for this range is also obtained using an exponent $\beta = {}^1/_2$. At higher incommensurabilities the Br coverage is not determined by the proximity to the C−UIC phase transition, but rather by the compressibility of the Br adlayer (see section III.F), which may explain the deviations in the exponent. The widths of the X-ray diffraction peaks in the incommensurate direction scale quadratically with the wave-vector components in this direction and increase continuously by an order of magnitude as the C−UIC transition is approached from the UIC side.[164] This behavior is consistent with “cumulative disorder” in the $c(\sqrt{2} \times p)$R45° phase, where the positional uncertainty between two adsorbates is proportional to the square root of their separation along the incommensurate direction[288] and may result from random pinning effects.

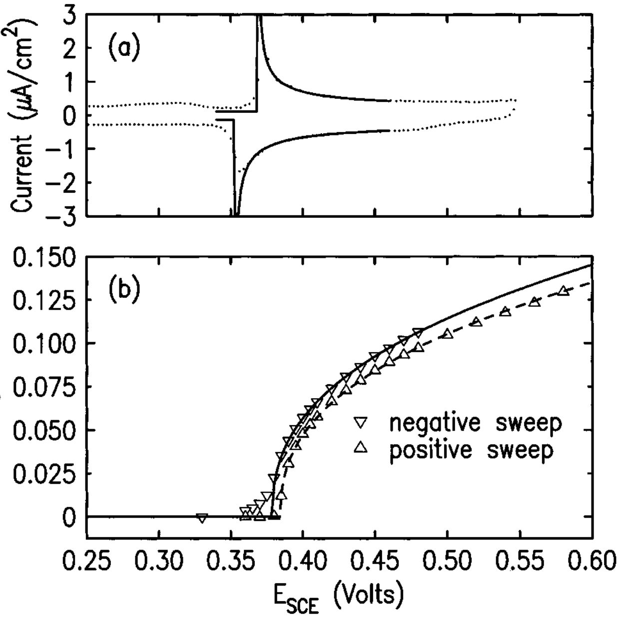

Figure 13. (a) Cyclic voltammogram (dashed line, 10 mV/s) and (b) corresponding incommensurability ϵ as a function of the applied potential of Au(100) in 50 mM NaBr. The solid line is a power-law fit to the incommensurability with $\beta = 0.4$. (Reprinted with permission from ref 164. Copyright 1996 American Physical Society.)

The kinetics of the phase transitions in the Br adlayer on Au(100) was studied by electrochemical potential-step experiments.[165] For the disorder ↔ $c(\sqrt{2} \times 2\sqrt{2})$R45° transition the current transients indicated in both directions an instantaneous nucleation and growth of the new phase coupled with Br adsorption/desorption. The situation is less clear for the transition between the commensurate and incommensurate phase, where a maximum in the transients indicative of nucleation and growth was found only in the $c(\sqrt{2} \times p)$R45° → $c(\sqrt{2} \times 2\sqrt{2})$R45° transition, but not in the reverse direction. The latter may be related to the considerable disorder found in the $c(\sqrt{2} \times 2\sqrt{2})$R45° phase when it was formed from the incommensurate phase.[164] It should be mentioned that in the electrochemical measurements of the $c(\sqrt{2} \times p)$R45° → $c(\sqrt{2} \times 2\sqrt{2})$R45° transition the potential was always stepped into the potential regime of high incommensurability, i.e., in the uniformly compressed adlayer phase. It hence does not allow conclusions on the second-order character of the phase transition in the range of the weakly incommensurate phase. Finally, a similar kinetic study of phase transitions in the halide adlayers on Ag(111) by Innocenti et al. [289] also indicated a diffusion-controlled adsorption, followed by progressive nucleation and growth.

IV. Adlayers of Molecular Anions

A. Hydroxide and Sulfide

Hydroxide adsorption is involved in oxygen evolution and electrooxidation—reactions of substantial importance in electrochemistry—and in this context has been studied extensively on numerous electrode surfaces by electrochemical and spectroscopic methods. A review of these results is beyond the scope of the present paper and can be found elsewhere.[19,290,291] A dedicated study of OH adsorption on well-defined Au(111) surfaces obtained by chronocoulometry and in situ FTIR spectroscopy was recently published by Chen and Lipkowski.[292] Here a three-stage process was found, where with increasing potential first a low coverage polar bound OH adspecies was formed, followed by a region of rapid increase in coverage up to $^1/_3$ and a concomitant decrease in the polarity of the surface bond (electrosorption valency $\gamma \approx 1$), until finally a surface oxide is formed at the most positive potentials. Spectroscopic evidence for strongly specifically adsorbed OH species was also found on other metal electrode surfaces, such as Cu(111).[293] In agreement with these results, recent density functional calculations of the interaction of OH and O with the (111) surfaces of various noble and transition metals by Koper and van Santen [294] indicated a largely ionic bond, a preferred adsorption in threefold hollow sites, and a charge transfer toward the metal in the presence of a positive potential. The trends in the OH adsorption energy on different metals could be explained by a reduced covalent interaction and a weaker Pauli repulsion with the metal d electrons for OH as compared to O.

Considering their important role in electrochemical reactions, remarkably little direct structural data on OH or O adsorbate layers exist. In most systems, no ordered superstructures were observed by STM/AFM, indicating that the adlayers are either disordered and highly mobile or adopt a (1 × 1) structure. This may be facilitated by the small size of the adsorbate as well as the rather covalent OH bonding, resulting in weaker repulsive dipole−dipole interactions at positive potentials. In situ AFM observations of oxygen or hydroxide adlayers with nonpseudomorphic structures were reported by the group of Gewirth for Cu(100) and Cu(110) in acidic H_2SO_4 and $HClO_4$ solution.[180,295,296] For Cu(100) a $c(2 \times 2)$ adlayer was found,[295] which however could not be observed in a later in situ STM study by Vogt et al.[186] For Cu(110), (2 × 1) and (3 × 1) structures were reported, where the adsorbates formed chains along the [001] direction and were located on top of the close-packed atomic rows of the Cu substrate.[180,296] It was suggested that these chainlike structures correspond to an oxygen-induced Cu surface reconstruction, similar to that found in STM observations of oxygen adsorption on Cu(110) under UHV conditions.[297] For Cu(111) in NaOH solution a rather open hexagonal adlayer structure was observed in an in situ STM study by Maurice et al.,[298] which was attributed to a (2 × 2) hydroxide adlayer on top of a reconstructed Cu surface (see section VI.A) with a resulting OH coverage of ≈0.2 ML. In addition, the structure of OH adlayers on Pt(111), prepared by coadsorption of O with H_2O or H, was recently studied under UHV conditions by low-temperature STM, LEED, and electron energy loss spectroscopy by Bedürftig et al.,[299,300] revealing a $(\sqrt{3} \times \sqrt{3})$R30° and a (3 × 3) phase for temperatures below 200 K (at higher temperatures redecomposition to H_2O and O occurs). In both phases the OH coverage is $^2/_3$ ML and the hydroxide adopts a well-defined geometry, where it is adsorbed in an on-top position on the Pt atoms, tilted with respect to the surface normal, and forms hydrogen bonds to neighboring OH adsorbates. It was suggested that the main difference between the two ordered phases is the arrangement of the H bond, which was proposed to be circular for the (3 × 3) and random for the $(\sqrt{3} \times \sqrt{3})$R30° phase.[299] Since the order in the OH adlayer was shown to depend strongly on the preparation conditions, it is currently not clear whether similar ordered phases also exist at room temperature at the electrochemical interface, although a similar local adsorption geometry seems plausible.

The adsorption of sulfide was preferentially studied in alkaline solution, where HS^- is the predominant species. It is generally accepted that with increasing potential first an HS_{ad}^- or HS_{ad} species and then a strongly chemisorbed adlayer of largely discharged S_{ad} is formed (refs 77 and 301 and references therein). In these adlayer phases HS most likely is adsorbed in hollow sites, according to ab initio calculations for (111) and (100) oriented Au and Ag clusters.[302] At even higher potentials, electrochemical oxidation of the adsorbate occurs, resulting in polysulfide species. On the basis of surface-enhanced Raman measurements on Au, the formation of S_8 rings and open-chain polymers was suggested by Gao et al.[301] Only a few studies of sulfide adsorption on single-crystalline electrode surfaces have been reported up to now. Gao et al.[303] investigated the S adlayer structure on Au(111) by in situ STM. In the potential regime of the monomer S adsorbate a simple $(\sqrt{3} \times \sqrt{3})$R30° structure was observed. Upon electrooxidation, a complex ordered structure formed by rectangular rings with nearest neighbor spacings of 2.6 Å in the rings and 4.8 Å between neighboring atoms in adjacent rings and structurally similar, more disordered structures were observed. On the basis of the small spacing within the rings, these structures were attributed to a close-packed arrangement of S_8 rings, which due to epitaxial effects are distorted with respect to bulk phase polysulfur.[303] Similar results were obtained by McCarley et al. using ex situ STM[304] and in a recent in situ STM study by Andreasen et al.[305] The latter also investigated the mechanism of the $S_8 \rightarrow (\sqrt{3} \times \sqrt{3})R30^\circ$ phase transition and suggested a model involving the formation of rectangular tetramer intermediates during this transition. In addition, evidence for Au steps decoration by S_{ad} after desorption of the $(\sqrt{3} \times \sqrt{3})R30^\circ$ phase was found at negative potentials.[305] Sulfide adsorption on Ag(111) was studied in detail by the group of Guidelli using in situ STM and electrochemical methods.[112,289,306] Here a $(\sqrt{3} \times \sqrt{3})R30^\circ$ phase was found, followed at higher potentials by a $(\sqrt{7} \times \sqrt{7})R19^\circ$ structure with a coverage of $^3/_7$,[306] which is in good agreement with previous ex situ STM results on emersed electrodes by Heinz and Rabe[307] as well as with S_{ad} coverages determined by chronocoulometry[77,112,306] and quartz microbalance.[77] High-resolution images of the $(\sqrt{7} \times \sqrt{7})R19^\circ$ phase indicated an arrangement of the sulfur atoms in trimers with 2.6 Å spacing between trimer atoms, indicative of a covalent bond, and 4.2 Å between atoms in adjacent trimers.[306] Similar results were obtained for sulfur adlayer structures in UHV. For transition metal surfaces less data exists. On Ni(100) electrodes a $c(2 \times 2)$ sulfur adlayer phase was observed by Suzuki et al. using in situ STM.[308,309] Furthermore, Sung et al.[310] reported for adlayers formed by gradual oxidative removal of preadsorbed sulfide with continuously decreasing coverage a sequence of commensurate structures, specifically a (1×1) phase ($\theta_S = 1$ ML), a $c(2 \times 2)$ phase ($\theta_S = 1/2$ ML), a $(\sqrt{3} \times \sqrt{3})R30^\circ$ phase ($\theta_S = 1/3$ ML), and a $p(2 \times 2)$ phase ($\theta_S = {}^1/_4$ ML). Finally, structurally similar monomer and oligomer adsorbate phases were also found for electrochemically deposited adlayers of the other group VI elements, i.e., Se and Te.[311,312] All these species exhibit a general tendency toward covalent adsorbate−adsorbate interactions, resulting in a complex phase behavior, which is only partially understood up to now.

B. Cyanide and Thiocyanide

The pseudohalides CN and SCN are strongly specific, often irreversibly adsorbing anions, paralleling their great capacity to form metal complexes. In analogy to the geometry of CN metal complexes, the cyanide adsorbate is generally believed to bind through its C-end to the metal surface. CN adsorption on noble and transition metal electrodes has been studied by in situ FTIR spectroscopy [63,313−316] and sum frequency generation,[68−74] indicating predominantly linearly bonded species. On the basis of the less pronounced shift of the bands with potential, a less ionic CN−metal bond for Au, Pt, and Pd than for Cu and Ag was proposed.[63] Indeed, ab initio cluster calculations found a largely ionic bond for CN on Cu(100)[317] but a predominantly covalent bond for CN on Pt(111).[73] A systematic study of crystallographic effects was performed for CN on the three low-index Au surfaces by Tadjeddine and Le Rille,[71] revealing a similar on-top binding geometry for all surface orientations and an increasing CN adsorption strength on the more open (100) and (110) surface.

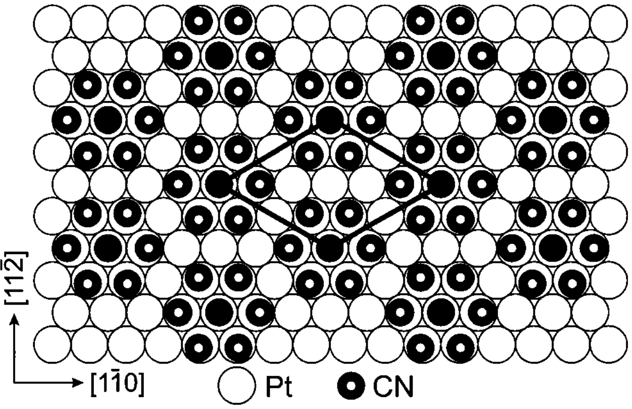

Figure 14. Model of the $(2\sqrt{3} \times 2\sqrt{3})R30^\circ$ CN adlayer phase on Pt(111). (Adapted from refs 313 and 321.)

Structural studies have focused on CN adsorption on the Pt(111) electrode. Ex situ LEED and Auger spectroscopy experiments on CN-covered electrodes emersed at the open circuit potential from solutions containing various cations and of variable pH were performed by the group of Hubbard.[270,318−320] They reported a $(2\sqrt{3} \times 2\sqrt{3})R30^\circ$ structure as well as a pH-dependent coadsorption of the cations. Furthermore, a $(\sqrt{13} \times \sqrt{13})R14^\circ$ structure with slightly lower CN coverage was found after emersion at more negative potentials.[318] The first in situ STM study of an ordered CN adlayer was reported by Stuhlmann et al.,[313,314] who observed the $(2\sqrt{3} \times 2\sqrt{3})R30^\circ$ structure on Pt(111) in sodium-containing electrolyte. Interestingly, a nonuniform packing of the adlayer in the form of ordered hexagonal “clusters” was found. On the basis of parallel in situ FTIR spectroscopy experiments, which indicated a single, linearly bound species, Stuhlmann et al. suggested a model with a CN coverage of $\theta = 0.583$, where CN adsorbed in symmetric top sites is surrounded by six CN adsorbates in a near top-site geometry (Figure 14). An alternative model, based on a comparative in situ STM study of the $(2\sqrt{3} \times 2\sqrt{3})R30^\circ$ phase in solution containing Na^+ and K^+ counterions, was suggested by Kim et al.[321] Here the apparent height of the central spots in the hexagonal “clusters” depended strongly on the tunneling conditions and increased significantly after introducing K^+ ions in the electrolyte, which are known to coadsorb more strongly with CN than Na.[319] These observations were interpreted by assigning the central spot (filled circles in Figure 14) to cations bound by a crown ether-like hexagonal ring of coordinating cyanides. At more negative potentials, a (2×2) phase and a $(\sqrt{7} \times \sqrt{7})R19^\circ$ structure were observed in alkaline solution and in acidic Na-containing electrolyte, respectively.[321] The $(\sqrt{7} \times \sqrt{7})R19^\circ$ phase was explained by a model with four CN adsorbates per unit cell ($\theta = 0.57$). This seems to be at variance with the model proposed in the same work for the $(2\sqrt{3} \times 2\sqrt{3})R30^\circ$ phase, which corresponds to a coverage of $\theta_{CN} = {}^1/_2$, i.e., would require a decrease in the CN surface density with increasing potential. Hence, despite these extensive ex and in situ studies, the adlayer structure in this complex system is still not unambiguously clarified. The formation of ordered structures can be expected also for CN adsorbed on other metal surfaces than Pt but was not reported up to now. The only other indication for an ordered CN adlayer was observed during the anodic dissolution of Au(111) in CN-containing solution; however, the high surface mobility in this case prohibited the determination of the surface structure.[322]

For SCN on Ag, Au, and Pt electrodes, FTIR spectroscopic studies indicate that S− as well as N-bound adsorbates exists, corresponding to the two possible orientations found in metal complexes.[63] This is in agreement with cluster calculations for SCN on Ag by Paccioni et al.,[84,323] where similar adsorption energies were calculated for both orientations. For the N-bound adsorbate, a perpendicular orientation was found, whereas the S-bound species had a relatively flat orientation relative to the surface (Ag−S−C angle ≈ 100°). The dependence of the adsorption energy on the angle between SCN and the surface, however, was rather weak, suggesting that at high coverages the adsorption geometry may be largely determined by the adsorbate−adsorbate interactions.[84,323] In agreement with spectroscopic results, which found a considerably more ionic bond for SCN on Ag than on Au,[143] the calculations indicated a largely ionic bond. In situ STM studies of SCN adlayers on Pt(111) were reported by Yau et al.[324] and Peng and Breen,[325] which both reported a (2×2) structure with $\theta_{SCN} = {}^1/_2$, in agreement with previous ex situ LEED and AES results.[270] These observations were rationalized by models where the molecules were adsorbed in hollow sites[325] or on both top and hollow sites.[324] On Rh(111) Wan et al.[326] observed a $(2 \cdot 2)$ phase in acidic and a $c(2 \times 4)$ phase (denoted as $(2 \times \sqrt{3})$ structure) in alkaline solution using in situ STM, which were both attributed to primitive structures with $\theta_{SCN} = {}^1/_4$ on the basis of the appearance of the STM images. This would imply that the SCN surface densities on Rh and Pt are by a factor of 2 different, which seems questionable. More likely also on Rh, two SCN adsorbates are present in the unit cell, as further supported by the observation of a $c(2 \times 4)$ structure with a coverage of ${}^1/_2$ for sulfur on Rh(111) in UHV.[327] The pH dependence of the SCN adlayer structures on Rh(111) was attributed to the competing effects of H^+ and K^+ coadsorption.[326] In addition, an ordered SCN adlayer with a square ringlike arrangement similar to that of adsorbed sulfide was found on emersed Au(111) in air in the STM study by McCarley et al.[304]

C. Sulfate

Studies of oxyanion adsorption have largely focused on the sulfate/bisulfate ion, the most important representative of this class of anions. Although this anion is less specifically adsorbed than the halides and pseudohalides, it was shown in early studies of Au and Pt single crystal electrodes to considerably affect the shape of the cyclic voltammograms.[20,22,328−330] In particular, characteristic spikes were observed on the (111) surfaces (see Figure 1)—the so-called "butterfly" peak on Pt(111)[20,328,329]—whose nature was strongly debated but which are now recognized as indicators of an order−disorder transition in the sulfate/bisulfate adlayer (see below). More detailed thermodynamic data on the SO_4^{2-}/HSO_4^- adsorption on these metal surfaces were obtained recently via chronocoulometry,[102,331−333] radioactive labeling,[331,334−336] and electrochemical quartz microbalance.[337] In contrast to the results obtained for halide adlayers (see section III.A), these studies indicated maximum surface concentrations that were significantly below those expected for close-packed sulfate adlayers layers.

An extensively used technique in the study of sulfate/bisulfate adsorption on metal electrodes has been in situ infrared spectroscopy. Here we concentrate on more recent FTIR results obtained on single-crystal electrodes; a survey of the older data is given in refs 63 and 65. Several groups have reported FTIR measurements on Pt(111)[63,65,338−342] and Au(111).[66,341−345] Although there is general agreement in the experimental results, the authors disagree on the assignment of the observed bands and the implications for the structure of the adsorbate. Particularly controversially discussed has been the nature of the adsorbed species, i.e., whether the adsorbed species is the sulfate or the bisulfate anion. Under the experimental conditions of most of the studies, bisulfate is the dominant species in the electrolyte. Nevertheless, several groups have proposed sulfate as the adsorbed species, even in strongly acidic solution,[63,66,336,343,345] as also suggested for Au(111) in the chronocoulometric and radiochemical study by Shi et al.[331,332] On the basis of experiments at variable pH, Faguy et al.[339] concluded that the adsorbate on Pt(111) is not the sulfate ion and suggested a bisulfate-like adsorbate, formed by a $SO_4^{2-}-H_3O^+$ ion pair up to pH 3.4. For pH 1, Shingaya and Ito[342] observed clear isotope effects in a recent FTIR study of Au(111) and Pt(111) in deuterated solution, strongly suggesting adsorption of bisulfate or coadsorbed sulfate/hydronium ion pairs. In the same study a HSO_4^- adsorbate was also suggested on Rh(111) and Cu(111), whereas on Ag(111) substantial sulfate adsorption was found both by Shingaya and Ito [342] and by Marinkovic.[346] General agreement exists on the adsorption geometry of the adsorbed species. On (111)-oriented surfaces, a C_{3v} symmetry is usually found, which was rationalized by models where the sulfate/bisulfate binds with three of its oxygen atoms to the metal surface, reflecting the good match in the symmetry of the tetragonal anion and the trigonal substrate lattice. This assignment is in agreement with recent calculations of Patrito et al. [347] on the adsorption of sulfate on Au(111)- and Ag(111)-type clusters. On (100) and (110) surfaces, a C_{2v} symmetry was proposed.[63,65,345]

Ex situ studies of sulfate/bisulfate adsorption have been proven difficult, due to artifacts caused by the emersion of the electrodes from the electrolyte.[30,348] As will be discussed below, keeping the adlayer at room temperature in UHV results in substantial dehydration, which causes pronounced changes in the adlayer structure. Hence, in situ structure-sensitive techniques are essential for the study of this adsor-

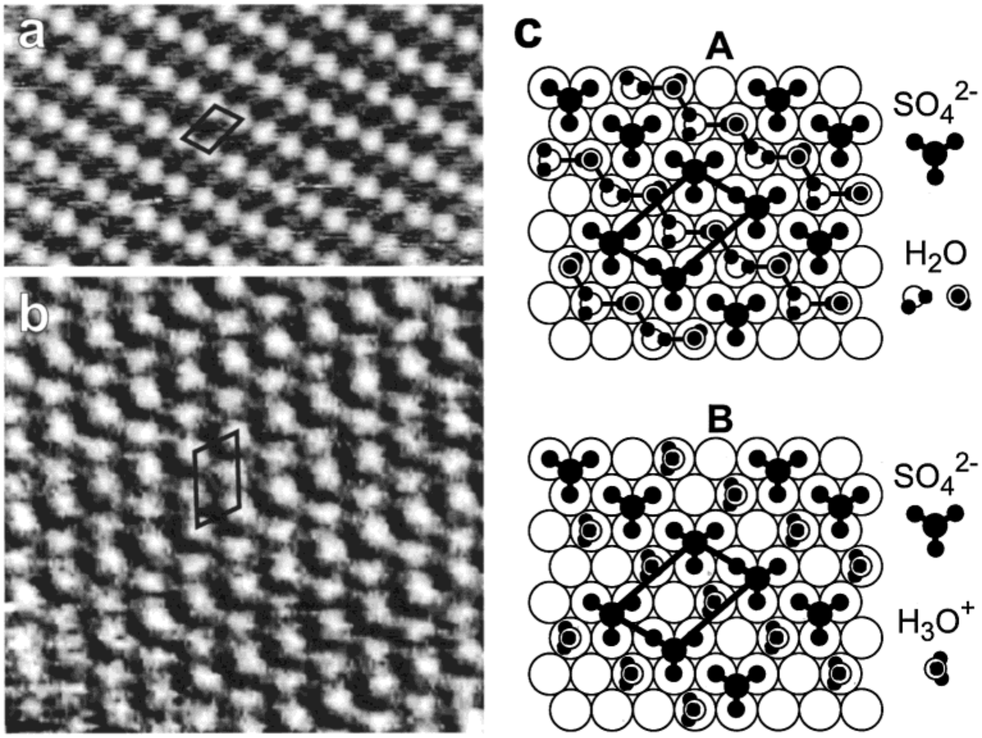

Figure 15. In situ STM images of the ordered sulfate adlayer on Au(111) in 100 mM H_2SO_4 solution (image sizes are (a) 58 × 44 Å^2 and (b) 48 × 48 Å^2). (c) Models of the sulfate adlayer structure as suggested in ref 350 (A) and ref 357 (B).

bate. The first observation of an ordered sulfate/bisulfate was reported on Au(111) by Magnussen et al.[41] Here a commensurate superstructure with an oblique unit cell and unit cell vectors of $\sqrt{3}a_{\mathrm{Au}}$ and $\sqrt{7}a_{\mathrm{Au}}$ in length (Figure 15a,b) was found by in situ STM in the potential regime positive of the sharp spikes (D3/D3′ in Figure 1) in the corresponding voltammogram, which is commonly denoted as a $(\sqrt{3} \times \sqrt{7})$ structure in the literature. The $(\sqrt{3} \times \sqrt{7})$ phase on Au(111) was confirmed by Eden et al. using in situ STM/FTIRS[343] and by Nishizawa et al. using in situ AFM.[349] In addition, the same commensurate structure was found in in situ STM studies of Wan et al. on Rh(111),[350] Ir(111),[351] and Pd(111)[352] and by Funtikov et al. on Pt(111).[353,354] This strongly suggests that the SO_4^{2-}/HSO_4^- adlayer on these metal surfaces is identical in nature, with the molecules occupying the same, well-defined adsorption sites, in agreement with the spectroscopic data. Typically, STM images of the $(\sqrt{3} \times \sqrt{7})$ phase exhibit one pronounced maximum per unit cell and a second, weaker maximum between the two next-nearest neighbor main maxima (Figure 15a). The apparent height and position of the weaker maxima depends strongly on the tunneling conditions (see Figure 15b); in some cases, even two maxima were found.[351,355] Moreover, with decreasing tunnel gap resistance, i.e., decreasing tip−sample separation, a gradual transition from images showing the $(\sqrt{3} \times \sqrt{7})$ lattice to images showing the (1 × 1) substrate lattice was observed for the phase on Au(111).[41]

Various models were suggested to rationalize the observed adlayer structure, in particular the unusual anisotropy in the adsorbate spacings, which cannot be explained by simple packing arguments. In the study by Magnussen et al.,[41] two bisulfate molecules per unit cell ($\theta = 0.4$) were suggested, on the basis of the observation of two types of maxima and on estimates of the anion coverage from early voltammetric data.[22] To account for the more recent chronocoulometric and radiochemical data by Shi et al.[331] (see also Figure 2), Edens et al. proposed a model with a sulfate coverage of 0.2 and the incorporation of hydronium ions between the SO_4^{2-} adsorbates.[343] The latter could stabilize the ordered adlayer by reducing the Coulombic repulsion between the anions. This model was further refined by Wan et al.,[350,351] who explained the anisotropic arrangement of the sulfate molecules by a structure where zigzag chains of hydrogen-bonded water are inserted between the rows of sulfate molecules (Figure 15c, model A), resembling the hexagonal ice bilayer structure. Alternatively, every second water molecule may be replaced by a hydronium ion, resulting in a structure similar to that proposed by Edens et al. The identical adlayer structure on all these metals—despite the different substrate lattice parameters—indicates a strongly localized SO_4^{2-}/HSO_4^- bonding. Apparently, the lateral interactions between the molecules are less dominant, which can be rationalized by these models of a rather open sulfate network, stabilized by hydrogen-bound species. The STM observations are only of limited use for the direct verification of these structural models, since in view of the possible superposition of an adlattice and substrate lattice as well as the general problems in the interpretation of STM images of such complex adlayers (see section II.A) the observed maxima in the STM images cannot unambiguously be assigned to adsorbate species. In particular, the water or hydronium molecules in the proposed models all occupy top sites of the Au lattice and hence would be indistinguishable from the underlying Au surface atoms (see Figure 15c).

Interesting complementary data, which may help to clarify the adlayer structure, were recently reported by Shingaya and Ito,[340,341,356,357] who performed an extensive, comparative study of sulfate/bisulfate adlayers on Pt(111) formed at the electrochemical interface and by SO_3 and H_2O coadsorption under UHV conditions, using FTIR spectroscopy, LEED, and TDS. At 190 K the UHV experiments suggested an adlayer consisting of hydrated HSO_4^- and H_3O^+ coadsorbates and a diffuse $(\sqrt{3} \times \sqrt{7})$ LEED pattern. The FTIR spectra obtained under these conditions strongly resembled those found in the in situ experiments in the potential range of the $(\sqrt{3} \times \sqrt{7})$ phase and indicated an adsorption geometry where the C_3 symmetry axis for the bisulfate was perpendicular and that of the hydronium ion parallel to the metal surface. From these results a model close to that of Edens et al. was derived (Figure 15c, model B), in which the coadsorbed HSO_4^- and H_3O^+ molecules interact via hydrogen bonds and are arranged in a structure similar to that of oxonium hydrogen sulfate.[357] In addition, a stabilization of this structure by hydration water on top of the HSO_4^-/H_3O^+ layer was proposed. At higher temperatures, pronounced dehydration occurred, resulting in the formation of a H_2SO_4 adlayer with a well-defined $(\sqrt{3} \times \sqrt{3})R30°$ structure. The same structure was also observed in ex situ studies of Au(111), Pt(111), and Rh(111) electrodes emersed from sulfate-containing solution.[358−360] The results by Shingaya and Ito seem to be at variance with an adlayer involving a rigid, icelike water structure and suggest a more dynamic interface water, such as that found in the computer simulation studies of halide and alkali ions.[89−95] It should be mentioned, however, that very different conclusions, supportive of the model proposed by Wan et al., were reached in a recent in situ ATR−SEIRS study of Au(111) by Ataka.[66] Here a sulfate adsorbate, stabilized by hydrogen-bound water, and a similar adlayer geometry as in model B were suggested. Due to the surface enhancement, the signal is especially high in these measurements, although the interpretation is not unambiguous, since the nature of this effect is not completely understood. In particular, it is not clear if the enhancement is also active on top of the (111)-oriented Au clusters or if it is restricted to the region of the high electric fields at the edges of the clusters, i.e., to surface areas that most likely are not covered by a well-ordered $(\sqrt{3} \times \sqrt{7})$ phase. The precise nature of this complex structure is therefore still under debate, although hydrogen bonding and screening by coadsorbed hydronium cations both seem to be important for stabilizing this strongly anisotropic anion adlayer phase.

A somewhat different phase behavior was found for sulfate/bisulfate adlayers on Cu(111) and Ag(111) surfaces. For Cu(111) in sulfuric acid solutions, in situ STM observations of an adlayer with similar but not identical structure as the $(\sqrt{3} \times \sqrt{7})$ phase were reported by several groups,[31,42,355,361−365] with the most extensive study being performed by Wandelt and coworkers.[31,42,355,361,362] In this system a sulfate adlattice with similar lattice parameters as in the $(\sqrt{3} \times \sqrt{7})$ phase on Pt(111) is found, which is superimposed by a Moiré pattern. A detailed discussion of this structure, which has been shown to correspond to a sulfate-induced Cu surface reconstruction,[355,361] will be given in section VI.A. A surprising exception in the tendency of sulfate/bisulfate to form ordered $(\sqrt{3} \times \sqrt{7})$ phases is Ag(111), were only the (1×1) substrate lattice was observed in STM studies in sulfate-containing solution.[366,367] This parallels the distinctly different spectroscopic results for Ag(111) as compared to the other metal surfaces, which suggest a sulfate rather than a bisulfate adsorbate.[342,346] In this case the adlayer ordering may be impeded by increased repulsive interactions between the anions. This is supported also by radiochemical measurements by Smolinski, which indicate a maximum sulfate coverage of 0.15, i.e., significantly below that of the $(\sqrt{3} \times \sqrt{7})$ phase.[368]

On (100) and (110) surfaces, electrochemical, radiochemical, and spectroscopic results generally suggest a weaker sulfate/bisulfate adsorption.[63,65,330,345,368,369] An ordered adlayer structure on these types of surfaces was only recently reported in an in situ STM study of Au(100) by Kleinert et al.[370,371] Here an incommensurate adlayer with a rectangular unit cell and molecular spacings of $1.4a_{\mathrm{Au}}$ and $3.6a_{\mathrm{Au}}$ was observed, with the close-packed rows oriented along the [011] and $[0\bar{1}1]$ directions of the Au substrate. Since the appearance of the adlayer resembled that of the $(\sqrt{3} \times \sqrt{7})$ phase, it was attributed to a similar hydrogen-bonded network with a sulfate coverage of 0.2. Interestingly, the adlayer was formed parallel to the anion-induced lifting of the Au(100) surface reconstruction and was stable on the unreconstructed surface down to 0.2 V versus SCE (in 0.1 M H_2SO_4), i.e., at 600 mV more negative potentials than that of the disorder $\leftrightarrow$ $(\sqrt{3} \times \sqrt{7})$ transition on Au(111). This effect can only partially be explained by the lower pzc of the unreconstructed Au(100) surface as compared to Au(111) and suggests a much stronger sulfate adsorption on this surface, as previously anticipated. In voltammograms no current spike could be detected at the potential of the order−disorder phase transition, which was attributed to the low degree of order in this adlayer. Furthermore, in the same study static disordered structures were observed on Au(100) and on Au(111) in neutral sulfate solution, supporting a stabilization of the ordered sulfate adlayer structures by coadsorption of H_3O^+.[371]

Finally, pronounced specific adsorption and indications for ordered adlayer structures were also found in voltammetric studies of other oxyanions.[344,372] Only very recently, however, direct in situ structural results have been published by Cuesta et al. for the case of phosphate adsorption on Au(100).[371] Apart from a lower degree of long-range order, the observed structure seems to be identical to that observed in the same study for sulfate on Au(100).

V. Coadsorption of Anions and Cations

It is known since the early thermodynamic studies on Hg electrodes[1,2,17,18] that specific adsorption involves the coadsorption of counterions to ensure

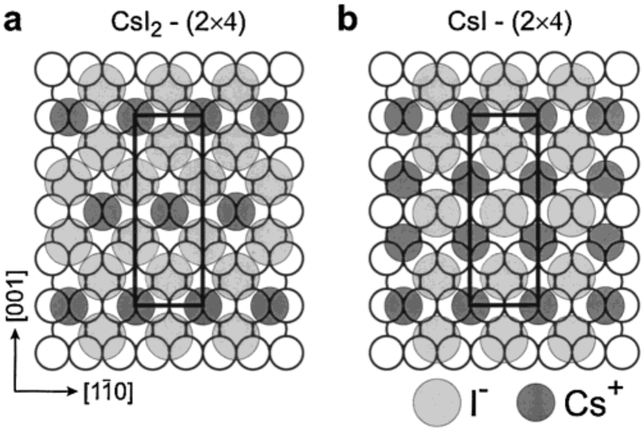

Figure 16. Models of the mixed adlayer structure formed in CsI solution on Au(110) as suggested (a) by Gao et al.[161] and (b) by Wang et al.[166]

charge neutrality. In traditional double layer models it is supposed that these counterions are hydrated and reside in the outer Helmholtz plane, i.e., at a larger distance to the surface as the specifically adsorbed species. Ex situ studies have shown that for strongly adsorbing anion species the surface coverages of both anionic and cathodic species can be substantial.[28,29,270,318−320,373] As already mentioned in the previous sections, in some cases where ordered structures were observed this has been interpreted in terms of a stoichiometric incorporation of cations into the anion adlayer, i.e., the formation of mixed, saltlike adlayers.

A particularly clear example of mixed adlayers is found on Au(110), where ordered structures of coadsorbed iodide and alkali metal ions were observed by Gao et al. using in situ STM[161] and Wang et al. using in situ SXS.[166] In both studies a rectangular (2 × 4) superstructure with a total adsorbate coverage of 0.75 was found in CsI solution. This (2 × 4) phase was observed in a ≈200 mV wide potential range with the most positive potential ≈100 mV more negative then the lower potential limit of the rotated pseudohexagonal iodide adlayer phase (see section III.H). To explain the height modulation in the STM images, Gao et al. proposed a model with a Cs:I stoichiometry of 1:2, i.e., $\theta_I = {}^1/_2$ and $\theta_{Cs} = {}^1/_4$ (Figure 16a). In contrast, Wang et al. suggested a model with a 1:1 stoichiometry and attributed the height modulation to the different adsorption sites (Figure 16b). Although I^- and Cs^+ are isoelectronic and hence cannot be distinguished directly by X-ray diffraction techniques, the measured lattice parameters favor the latter model, as pointed out by Wang et al.[166] The I^- and Cs^+ spacing of 3.96 Å is almost identical to that in bulk CsI (3.95 Å), whereas the neighboring iodine atoms in the model by Gao et al. would require a substantially larger spacing. In fact, the quasi-square structure shown in Figure 16b, which differs strongly from the quasihexagonal structures of the purely anionic iodide adlayers (see section III), is very similar to the atomic arrangement in the (110) plane of CsI. Such unpolar, saltlike structures should be preferred for binary ionic adlayers. The model is further supported by the similarity to the ordered binary adlayers found in the study by Wang et al. in KI, NaI, and LiI solution.[166] In these systems incommensurate (2 × p) phases were observed, which—in contrast to purely anionic, incommensurate adlayers—expanded with increasing potential (i.e., the electrocompression was negative). The CsI adlayer model in Figure 16b can be understood as an incompressible (2 × p) phase with $p = {}^4/_3$. Studies at variable iodide and alkali electrolyte concentrations revealed that the potential range of the binary adlayers only depended on c_I, indicating that the adlayer ordering is induced by the strong chemisorption of the anions, whereas the adlayer spacing depended predominantly on the type and concentration of the cations. These observations were rationalized by an increasing discharge of the chemisorbed anions with increasing potential, resulting in a decreasing screening of the repulsive cation−cation interaction and consequently an increase in the lattice spacing. The fact that the adlattice spacings in the different electrolytes, with the exception of CsI, do not accurately reflect the size of the alkali metal species was attributed to partial hydration of the cations. In addition, the presence of antiphase domain walls in the (2 × p) phases was suggested. Similar mixed alkali−halide adlayers should exist in other systems, as recently verified for Au(110)−Br.[170]

For more strongly bound cation adspecies, such as metal adlayers formed by underpotential deposition (UPD), the formation of ordered binary adlayers due to coadsorption of anions is a well-known phenomenon. A particularly extensively studied example is the underpotential deposition of Cu on Au and Pt single-crystal surfaces in sulfate- and halide-containing solutions. Here the combined results of studies by ex situ methods, in situ STM and AFM, in situ X-ray scattering and spectroscopy, chronocoulometry, quartz crystal microbalance, and radioactive labeling, and statistical models revealed the formation of various ordered superstructures consisting of mixed layers of Cu atoms and anionic adsorbates (see refs 36, 366, and 374−386 and references therein). In these systems the cation is the more strongly bound species and consequently the anions are adsorbed in a plane above the metal adlayer. Very similar results were reported for other UPD systems. A further, illustrative example is Tl and Pb UPD in chloride-, bromide-, and iodide-containing electrolyte, recently studied by Wang and co-workers using in situ SXS.[387−389] In this elegant work, a complex sequence of different ordered phases was observed with decreasing potential, which could be rationalized in terms of a gradual change from a pure halide adlayer via several mixed adlayer phases with Tl−halide stoichiometries of 1:1, 1:2, and 1:3 to a simple, metallic Tl adlayer. The mixed adlayers with 1:2 or 1:3 stoichiometry adopt high-order commensurate, hexagonal structures, whereas the adlayer phases with 1:1 stoichiometry exhibit commensurate or uniaxial-incommensurate structures with a rectangularly or rhomboedrically distorted arrangement of the adsorbates. This structural phase behavior was explained by symmetry and electrostatic considerations in 2D binary ionic crystals. In particular, it was shown that the mixed bilayer structure can differ substantially from that of the corresponding bulk salts. For example, Wang et al.[389] demonstrated via a detailed structural analysis of the SXS data and electrostatic energy calculations that the anions in the hexagonal metal halide layers with 1:1 stoichiometry are located in bridge sites between the metal adatoms rather than in the hollow sites, as proposed earlier on the basis of a comparison with (111)-oriented metal halide salts.

Furthermore, the onset of UPD was shifted to positive potentials in the presence of the specifically adsorbing anions according to these studies. The latter can be explained by recent calculations of Sánchez et al., who suggested that the coadsorbed anions not only determine the adlayer structure but can stabilize the metal ions on the surface and thus expand the potential range of the metal adlayer or even induce UPD.[390,391] In particular, they found for Cu on Au(111) and Au(100) that—contrary to the experimental data—no UPD shift would be expected. Hence, the Cu UPD phases result from a mutual stabilization of anions and metal cations on the Au substrate in a potential regime where both species alone are largely desorbed. This was qualitatively explained by the difference in pzc of the two metals, due to which Au is negatively and Cu strongly positively charged in the UPD range.[390] More general, not only the electrostatic but also the specific, chemical interaction of the anion with the admetal and with the substrate metal may be different. A similar effect can therefore be expected for a large number of systems.

As demonstrated by Stickney and co-workers, this phenomenon can be utilized for the defined layer-by-layer growth of compound semiconductor films [392,393]. In this “electrochemical atomic layer epitaxy” (ECALE) the substrate is alternatingly exposed to electrolytes containing the anionic and cathodic species with the potential being kept in the UPD regime of the corresponding species. Because the adsorption in each electrolyte is limited to a single monolayer, structurally well defined films of II−VI and III−V semiconductors can be formed by this technique.

VI. Influence on Substrate Structure

A. Reconstruction

It is well-known from studies at the metal−vacuum interface that the structure of metal surfaces can be strongly affected by chemisorbed species. In particular, adsorption can either induce the formation or the lifting of metal surface reconstructions, a phenomenon also observed at electrochemical interfaces. The potential-induced lifting of the reconstruction of Au and Pt surfaces in electrochemical environment due to anion adsorption is a thoroughly described phenomenon (for a recent review, see ref 111). Here we discuss the less frequently found effect of anion-induced reconstruction of metal electrodes.

The clearest example for this phenomenon is the ordered structure found by in situ STM on Cu(111) in sulfate solution.[31,42,355,361−365] The STM images exhibit a ($\sqrt{3} \times \sqrt{7}$)-type of adlayer structure on the atomic scale (Figure 17a) as well as a pronounced (quasi)hexagonal modulation (Moiré pattern), which can be recognized also on larger scale images (Figure 17b). The latter clearly indicates an incommensurate structure of the adlayer. This was attributed to the small Cu lattice spacing, due to which a simple ($\sqrt{3} \times \sqrt{7}$) phase would correspond to a highly compressed sulfate adlayer;[355,361] i.e., the loss of registry with the substrate lattice is driven by the repulsive adsorbate−adsorbate interaction in the anion adlayer. The observation of a simple ($\sqrt{3} \times \sqrt{7}$) phase on an underpotentially deposited, pseudomorphic Cu monolayer on Pt(111),[394] where the Cu lattice spacing is 8.6% larger than on Cu(111), supports this idea. Two models could account for the Moiré structure: Either the sulfate adlayer is incommensurate with respect to the (unreconstructed) Cu substrate, similar as in the structures found for halides on Au and Ag surfaces, or the sulfate adsorbate forms a commensurate ($\sqrt{3} \times \sqrt{7}$) superstructure on an Cu surface layer that is expanded relative to the bulk lattice. Wilms et al. demonstrated in a detailed study that the latter model is valid, i.e., that sulfate induces a reconstruction of the Cu(111) surface.[31,42,355,361,362] The first evidence for this model comes from the observation of characteristic morphologic changes during the disorder ↔ order phase transition, which indicate changes in the density of the Cu surface layer. Parallel to the formation of the ordered sulfate adlayer, the growth of the Cu terraces and the formation of monatomically high Cu islands is observed, whereas upon disordering of the adlayer the width of the terraces decreases and holes are formed in the surface layer. These observations can be

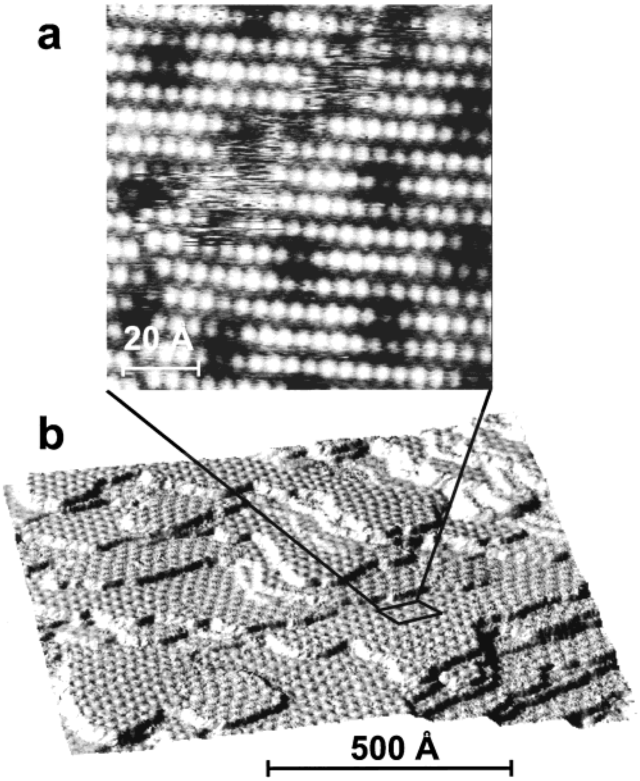

Figure 17. In situ STM images of Cu(111) in sulfuric acid solution showing (a) the atomic-scale structure (100 × 100 Å^2) and (b) the mesoscopic surface morphology (1100 × 1100 Å^2). (Reprinted with permission from ref 43. Copyright 1999 Material Research Society.)

rationalized by a lateral expansion of the topmost Cu layer in the presence of the ordered sulfate adlayer. More recently, Wilms et al. succeeded in directly observing the expanded lattice of the Cu surface atoms by choosing tunneling parameters where the sulfate adsorbate was transparent in the STM image.[42] From these measurements a quasihexagonal Cu surface lattice with unit cell vectors of 2.6 and 2.73 Å in length and at an angle of 56° was determined. The anion-induced reconstruction was attributed to a strong, localized interaction of the sulfate with the Cu surface atoms, favoring a $(\sqrt{3} \times \sqrt{7})$ sulfate adlayer that is commensurate with the underlying reconstructed Cu surface layer.[31,42,355,362] Apparently, the gain in energy associated with the formation of the ordered $(\sqrt{3} \times \sqrt{7})$ adlayer phase exceeds the negative contribution caused by the interface between the first and the second Cu layer. As pointed out by Wilms et al., this is similar to the Cu UPD layers on Au and Pt electrode surfaces, where also expanded Cu adlayers are stabilized by coadsorbing anions.

Although Cu(111)–sulfate is by far the most studied case of surface reconstruction induced by specifically adsorbed anions, evidence for this phenomenon has been found also in a number of other systems. The earliest work in which an adlayer structure was attributed to anion-induced surface reconstruction is the in situ STM study of Cu(110) by LaGraff and Gewirth.[180] Here $(1 \times n)$ structures were observed (see section IV.A), which were attributed to an O- or OH-induced added row reconstruction, in analogy to the structures found in the corresponding UHV system.[395] More recently, Maurice et al.[298] reported a similar hydroxide-induced reconstruction for Cu(111) in NaOH solution. It was proposed that the outmost Cu layer is expanded to a spacing similar as in $Cu_2O(111)$ with a primitive (2×2) lattice (relative to the expanded Cu surface layer) of adsorbed OH on top. Clear indications for halide-induced reconstructions have up to now only been reported on (110) electrode surfaces. Wan et al.[280] proposed that the (4×1) phase they observed for Cu(110)–Cl involves a reconstruction with a Cu coverage of $^1/_2$ in the topmost layer. According to their model, two neighboring Cu rows along the [001] direction are removed in each unit cell with the Cl adlayer forming a roughly hexagonal structure on top. Furthermore, Ocko et al.[396] as well as Gao and Weaver[161,279] found on Au(110) in iodide-containing solution a (1×3) reconstruction, whereas a (defective) (1×2) reconstruction was reported in nonspecifically adsorbing electrolyte. Here the iodide adlayer was disordered, demonstrating that also in this case the chemisorbed species can have pronounced influence on the surface structure.

It is not surprising that observations of well-ordered reconstructed surfaces with a coverage of metal surface atoms different from that of the unreconstructed surface ("reconstructive" surface reconstruction) have been reported exclusively on coinage metals electrodes. Due to the high surface mobilities of these metals at room temperature, the long-range mass transport required for the growth of the reconstructed phase is facile. In contrast, on Pt-group metals, where the mobility of the surface atoms is much lower, the formation of this type of reconstruction may be kinetically hindered, even if it is energetically favorable. It should be noted that this argument is not valid for displacive reconstructions, where no long-range mass transport is necessary; however, this type of reconstruction is usually more difficult to verify by microscopic techniques. Better suited for this are diffraction measurements, which, however, are less commonly used for the study of the electrochemical interface. Indications for displacive reconstructions induced by the formation of ordered anion adlayer phase were found, e.g., for Au(100)–Br, although a detailed structural analysis was not attempted.[164]

B. Restructuring

Specifically adsorbing anions interact not only with the perfect substrate lattice on the terraces but also with surface defects, such as steps, kinks, adatoms, or vacancies, and hence can have a pronounced influence on the electrode surface morphology. Evidence for this has been found in studies by ex situ LEED,[397−400] in situ STM,[401−404] and electrochemical methods,[405,406] where a drastic improvement in the surface order was observed in halide-containing electrolytes. This phenomenon—termed electrochemical annealing—indicates that chemisorbed anions strongly enhance the surface mobility of the metal ions, which can be rationalized by their ability to form metal complexes.

More recently, it was realized that the order in the anion adlayer can directly affect the structure and distribution of surface defects. As an example, the Cu(100) electrode surface in the presence of a disordered and an ordered $c(2 \times 2)$ Cl anion adlayer phase is discussed (Figure 18).[181,186,407,408] In the potential regime where the anion adlayer is disordered and only the (1×1) lattice of the Cu(100) substrate is observed, the steps are almost exclusively of monolayer height, oriented along random directions, and exhibit a characteristic, frizzy appearance (Figure 18a). This type of step morphology is observed for the disordered anion adlayers phases in sulfuric, perchloric, and hydrochloric acid solution, independent of the anion species. Similar frizzy steps were observed by STM on Cu and Ag surfaces in UHV and explained as a result of rapid (in comparison to the time resolution of the STM scans) kink motion along the step edge.[409,410] Hence, under these conditions, the influence of the anion adlayer on the Cu step structure and (qualitative) dynamic behavior is small. Similar observations were reported by Dietterle et al. for Ag(111) electrodes in sulfuric acid solution[367,411,412] and by McHardy et al.[413] and Giesen and Kolb[414] for Au(111) in halide-containing solution. Quantitative analyses[411,412,414−417] revealed that the influence of disordered anion adlayers on the step dynamics as compared to the bare metal surface under UHV conditions is small for weakly adsorbing anions, such as sulfate, or at low anion surface concentrations, but it can be substantial at higher surface concentrations and even change the dominant

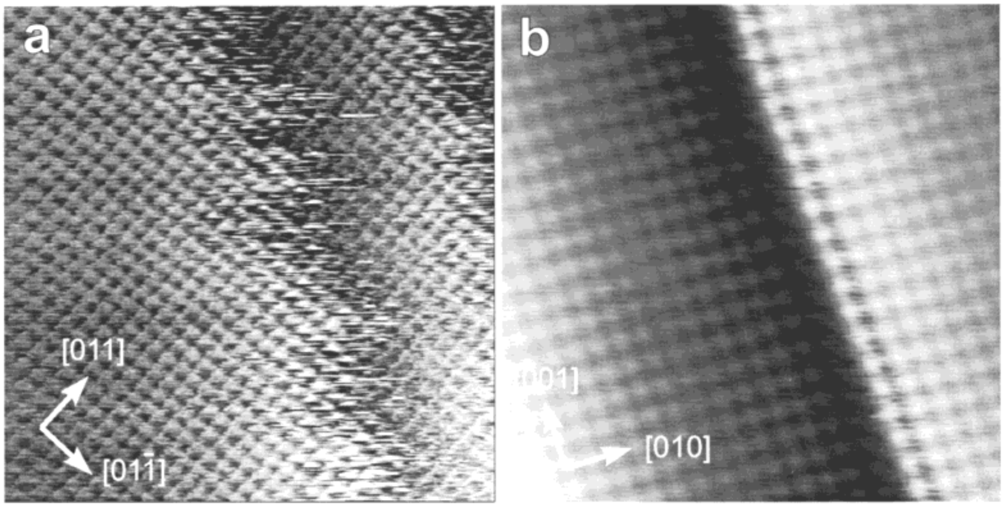

Figure 18. In situ STM images of Cu(100) showing (a) frizzy steps on a surface covered by a disordered adlayer phase (the observed lattice is the (1×1) lattice of the Cu substrate) and (b) the ⟨001⟩-oriented steps in the presence of a $c(2 \times 2)$ Cl adlayer (70×70 Å^2). (Reprinted with permission from ref 408. Copyright 1998 Wiley-VCH.)

mass transport mechanism (for details, see the recent review by Giesen[417]). Of particular interest in the present context is the study of Au(111) in iodide-containing solution by McHardy et al.,[413] where a clear minimum in the magnitude of the step fluctuations was found at the potential of the disorder ↔ $c(p \times \sqrt{3})$ transition, which was attributed to a change from terrace diffusion to step edge diffusion for Au adatoms.

In contrast to disordered adlayers, not only the dynamic behavior but also the surface morphology can be drastically altered in the presence of ordered adlayer phases, as illustrated in Figure 18b for the ordered $c(2 \times 2)$ Cl adlayer on Cu(100). Here a new equilibrium morphology is observed, where the steps are perfectly straight and almost exclusively oriented along the {001} directions, i.e., along the close-packed directions of the Cl adlattice. Furthermore, instead of only monatomic steps, double- and multilayer high steps are predominantly found. The steps are atomically smooth, and the position of the step edge is always localized between the maxima of the $c(2 \times 2)$ lattice, indicating that the structure of the steps is well-defined on the atomic scale. The faceting of the steps along the {001} directions was first observed in studies of Cu(100) corrosion by Suggs and Bard,[179] where it was attributed to the dissolution kinetic, but it was later identified by Vogt et al.[181,186] and by Moffat[183] as an equilibrium morphology, formed by a rearrangement of the surface during the disorder → $c(2 \times 2)$ transition, i.e., at a potential significantly below the onset of Cu dissolution. Hence, the change in step structure directly reflects the structural change in the anion adlayer. The almost perfect step orientation found in the $c(2 \times 2)$ phase indicates a very low kink density, several orders of magnitude smaller than for the randomly oriented steps observed in the presence of a disordered adlayer. Consequently, these {001} oriented steps are, in contrast to kinks at the randomly oriented steps in the regime of the disordered phase, strongly stabilized by the adsorbate, making the introduction of kinks very energy expensive. As pointed out by Wu and Barkey,[418,419] the formation of kinks in the {001} oriented steps implicates a locally lower Cl density, which could account for the associated cost in energy.

The transformation of the randomly oriented steps into {001}-oriented steps and vice versa is completely reversible. In contrast to the fast disorder ↔ $c(2 \times 2)$ transition in the adlayer, however, which occurs within a few seconds on the entire surface, the parallel step faceting/defaceting process requires long-range mass transport of Cu atoms and hence proceeds much more slowly. The mechanisms and dynamics of these surface restructuring processes can be directly observed by STM, as shown in Figure 19a for the formation of the faceted steps.[420] Directly after a potential step into the regime of the $c(2 \times 2)$ phase, microfacets in form of short, alternating [001] and [010] step segments evolve, resulting in a sawtooth-like shape of the steps (Figure 19a, part B). This initial faceting, which apparently occurs on the same time scale as the formation of the ordered adlayer, is followed by a slower ripening process, where some step segments grow at the cost of others, resulting in increasingly longer {001}-oriented segments (Figure 19a, parts C and D). Parallel, bunching of the monatomically high steps to double and multilayer steps occurs. The rate of this coarsening process, which can be quantified by measuring the average length of the {001} step segments, is initially high but decreases continuously (Figure 19b). This behavior is in good agreement with theoretical models of faceting, which find for the evolution of facet width with time a power-law behavior with an exponent β of $^1/_2$, $^1/_3$, or $^1/_4$, depending on the transport mechanism.[421] The best fits to the data in Figure 19b were obtained with $\beta = {}^1/_4$ (dashed line), suggesting that quasi-one-dimensional diffusion along the step edges is the dominant transport mechanism. Changes in the local step positions are observed even after the potential is kept in the range of the $c(2 \times 2)$ phase for several hours; however, the faceting process was then difficult to distinguish from pure equilibrium fluctuations of the step positions. In addition, the rate of the faceting process strongly increases with increasing potential, which can be attributed to the

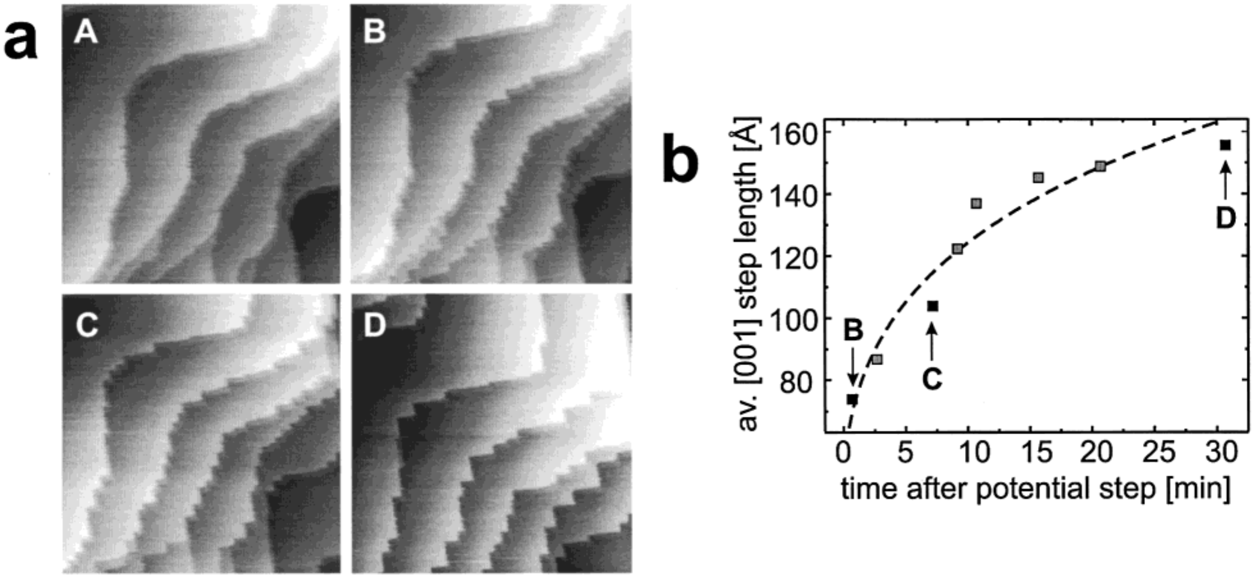

Figure 19. Cl-induced step faceting of Cu(100) in 10 mM HCl. (a) A series of in situ STM images obtained at -0.60 V_{SCE} (A) and at -0.25 V_{SCE} (B−D) showing the progressing faceting process (1000 × 1000 Å^2). (b) Average length of the ⟨001⟩-oriented step segments as a function of time t after the potential step, evaluated from the series of STM images partly shown in part a; the dashed line is the best fit to the power law ct^{β} with $\beta = 1/4$.[420]

increase in Cu surface mobility upon approaching the Cu dissolution range.

Atomic-scale studies reveal that the restructuring process proceeds by subsequent removal or addition of rows consisting of ($\sqrt{2} \times \sqrt{2}$)R45° unit cells (i.e., the primitive unit cells of the $c(2 \times 2)$ adlayer) at the step edge.[181,186] In this process ($\sqrt{2} \times \sqrt{2}$)R45° unit cells are subsequently dissolved or added at the structurally well-defined kink sites at the end of the rows. It is emphasized that these kinks are two Cu atoms in width, i.e., the two outmost rows of Cu atoms, and the row of Cl adsorbates on top of these rows are simultaneous removed or added. In the Cu(100)−Cl system the average rate of these local growth and dissolution processes is on the order of several angstroms per millisecond. Consequently, these events usually manifest in conventional STM images as discontinuous changes of the step position. Very recently, Zitzler et al.[422,423] succeeded in the first direct observation of these fast processes, using a newly developed high-speed STM, which can acquire atomic resolution images at rates of up to 25 images·s^{-1}. As an example, frames of a video sequence are shown in Figure 20 that illustrate the (particularly slow) growth of a single ($\sqrt{2} \times \sqrt{2}$)R45° row along a step of the Cu(100) substrate. Usually, the propagation of single rows is considerably faster and the dissolving or growing rows cross the observed surface area in $\leq 1/10$ s. From such video sequences of images, average growth rates of 1−2 Å ms^{-1} were obtained (see also section VII.A).

A similar mass transport mechanism governs the defaceting process, induced by a potential step from the regime of the $c(2 \times 2)$ phase into that of the disordered adlayer (Figure 21a).[420] Obviously, the process commences via parallel removal/addition of Cu atoms at particularly low/high coordinated sites, i.e., at the outer and inner corners of the Cu terraces, respectively, while the straight {001}-oriented step segments between are initially maintained (Figure 21a, part B). This process, which can be explained by a fast "intralayer" mass transport along the step edges, results in an increasingly rounded shape of the terrace corners. On a longer time scale, the images show a gradual removal of the facets, resulting in isotropic steps whose orientation is determined by the micrometer scale surface morphology (Figure 21a, parts C and D). Simultaneously, a debunching of the multilayer steps to steps of monatomic height is observed, indicating a slower interlayer transport of Cu atoms. The rates of both types of transport processes (i.e., "intralayer" and "interlayer") increase strongly with decreasing potential. As an example, an quantitative analysis of the "intralayer" transport is shown, which can be obtained from the STM images by evaluating the average number of Cu atoms (ΔN) removed per outer terrace corner as a function of time and potential (Figure 21b). The pronounced potential dependence of the defaceting process may be explained by the presence of the (disordered) Cl adlayer, which decreases in density parallel to the increase in the rate of the surface restructuring. Apparently, a transient stabilization of the {001} step orientation by the Cl adsorbate, which hinders the defaceting, is possible even in the disordered phase. This may be related to the second-order nature of the disorder ↔ $c(2 \times 2)$ phase transition (see section III.I), due to which a transient local order should exist even in the disordered phase. A lower surface mobility of Cu adatoms due to the presence of (disordered) Cl adsorbates alone seems less likely in view of the opposite behavior found for Au surfaces. The association of these potential effects with the changes in the anion adlayer rather than the corresponding variation in the electronic surface charge density of the metal is supported by the opposite behavior of Ag(111) in sulfuric acid solution. In the latter system, where the anions are less strongly adsorbed and the changes in the adlayer density are much lower, a potential-independent

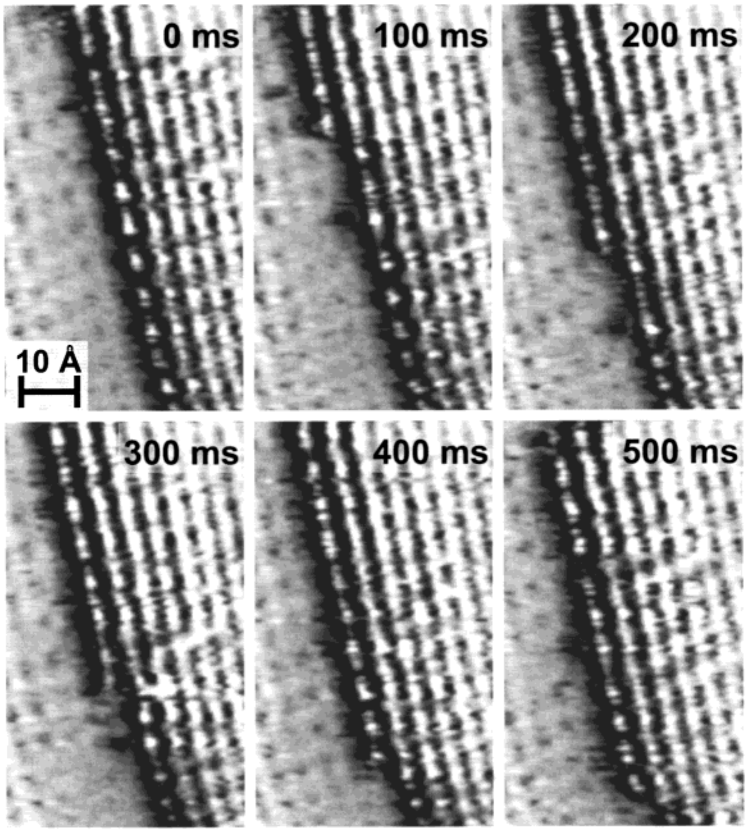

Figure 20. High-speed in situ STM observations of Cu(100) in 10 mM HCl solution at −0.23 V_{SCE} (43 × 47 Å^2; black arrows indicate scan direction). The images were subsequently recorded at a rate of 0.1 s per image and show the local growth of a single ($\sqrt{2} \times \sqrt{2}$)R45° row along the Cu step. (Reprinted with permission from ref 423. Copyright 2001 Elsevier Science Ltd.)

surface mobility was observed over a large fraction of the double layer range.[411] In conclusion, the results for the system Cu(100)−Cl indicate that the rate of both the faceting and the defaceting process increases with increasing overpotential relative to the potential of the disorder ↔ *c*(2 × 2) transition, however, due to very different reasons: While the potential-dependence of the defaceting can be rationalized by a decreasing stability of the {001}-oriented steps, i.e., an increase driving force for the restructuring process, the increasing rate of the faceting process with increasing potential seems to be related predominantly to the increasing Cu surface mobility.

Faceting/defaceting processes that accompany the order−disorder transitions in the anion adlayer seem to be a rather general phenomenon. For example, in situ STM studies of the *c*(2 × 2) phases of Pd(100)−I,[201,202] Ni(100)−S,[308,309] and Ag(100)−I[177] by Itaya and co-workers as well as of Cu(100)−Br by Broekmann et al.[188] also indicated a preferred orientation of the steps along the {001} directions. Furthermore, a similar tendency of the steps to orient parallel to the close-packed directions of the anion adlayer was also found in the systems Cu(111)−Cl,[31,178] Au(110)−I,[278] Ni(111)−I,[204] Cu(110)−Cl,[280] and Au(111)−Br.[169] Although most of these studies observed the formation of the faceted step morphology in the potential regime of metal dissolution or deposition, it seems highly probable that also in these systems the well-defined step orientation corresponds to an equilibrium morphology induced by the ordered adlayer phase rather than a kinetic effect related to the dissolution or growth. It should be noted that on Pt-group metal surfaces the long-range mass transfer is strongly kinetically hindered by the low surface mobility of the metal. The faceting/defaceting process may be therefore more difficult to observe than on Cu. Here the enhanced metal ion exchange with the solution during dissolution/deposition reactions may significantly promote the formation of larger facets. In addition, step faceting is not only found for simple commensurate structures but even for complex, incommensurate phases, such the sulfate adlayer phase on Cu(111). STM observations in the latter system reveal a clear, albeit less pronounced, faceted morphology, where the steps seem to consist of straight segments with preferential orientation along the close-packed directions of the adlayer-induced Moiré pattern.[31,43,355,362,364] A closer look, however, reveals that theses segments are straight only on the nanometer scale and that the atomic structure differs locally. This can be directly attributed to the incommensurate nature of this adlayer structure, which is incompatible with a well-defined local geometry at the steps. Finally, the adsorbate-induced step faceting is not restricted to the electrochemical interface but is also known for chemisorbed adlayers at the metal−vacuum interface. In particular, a faceting along {001} in the presence of a *c*(2 × 2) adlayer phase was found by Kopatzki et al. for Ni(100)−O and by Nakakura and Altman for Cu(100)−Cl and Cu(100)−Br.[231,236−238] This underlines the close relationship of the chemisorbed adlayers in the different environment, noted already in the previous sections.

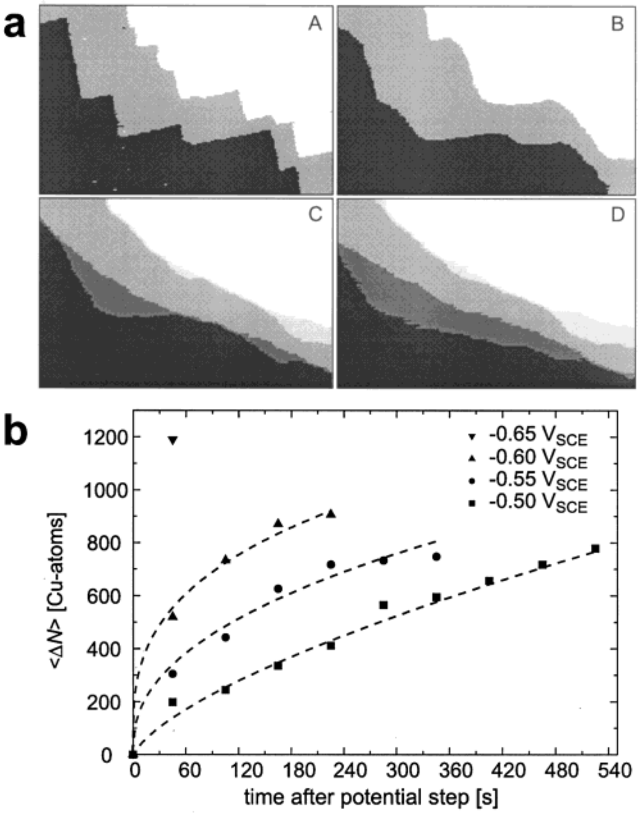

Figure 21. Defaceting of Cu(100) in 10 mM HCl after a potential step from $-0.25\ V_{SCE}$ into the potential range of the disordered adlayer phase. (a) A series of in situ STM images obtained at $-0.25\ V_{SCE}$ (A), 30 s (B), 180 s (C), and 510 s (D) after a step to $-0.65\ V_{SCE}$, showing the mass transport processes (1100×800 Å^2); for clarity, each Cu terrace is colored by a single gray scale. (b) Quantitative evaluation of the mass transport at different potentials from a series of STM images. As a measure of the transported mass, the average number of Cu atoms ΔN removed per outer terrace corner is used.[420]

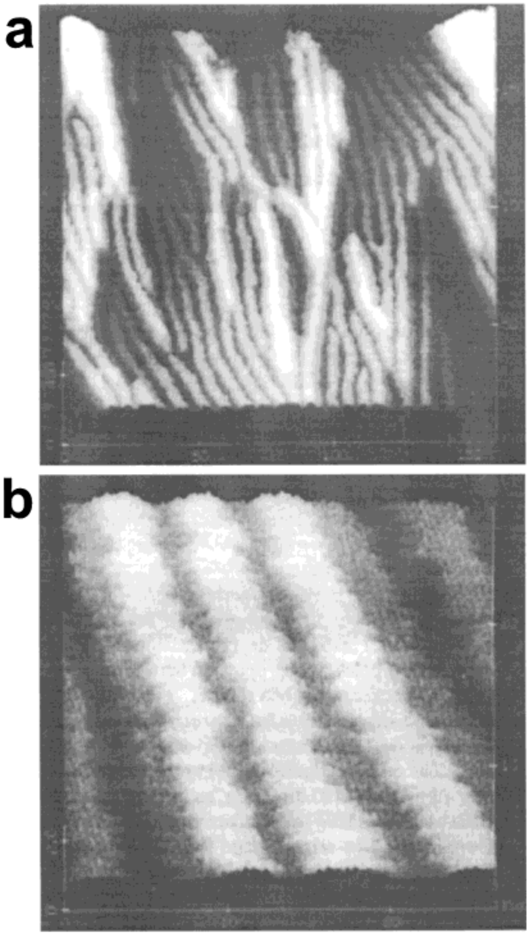

Figure 22. In situ STM images showing the iodide-induced restructuring of Au(110) in 5 mM KI solution (a) on the mesoscopic and (b) on the atomic-scale. (Reprinted with permission from ref 278. Copyright 1994 American Physical Society.)

We conclude this section with a brief discussion of an even more complex restructuring effect, observed by Gao and Weaver on iodide- and bromide-covered Au(110) electrodes.[161,170,278] Here the STM images revealed for Au(110)−I the formation of rather uniform arrays of long, monatomically high Au islands and channels, running parallel to each other and oriented roughly along the $[1\bar{1}0]$ direction, at the upper end of the potential regime of the $c(p \times 2)$ adlayer phase (Figure 22).[161,278] These islands decrease in width with increasing potential and completely disappear again in the negative potential range, indicating a well-defined, reversible dependence of the surface morphology on the potential. A very similar anisotropic restructuring was observed for Au(110)−Br; however, in this case only monatomic islands were formed and the structures were oriented along the [001] rather than the $[1\bar{1}0]$ direction.[170] Gao and Weaver suggested that the restructuring of this rather open surface is caused by a destabilization of the Au atoms in the center of the terraces due to the repulsive dipole−dipole interactions between the halide adsorbates. In this model, islands that are 6−10 atomic rows wide represent a compromise between the electrostatic repulsive and more local cohesive energy contributions. This surface restructuring proceeds predominantly via a mechanism involving local growth and dissolution at the Au steps and may be favored by the anisotropy of the Au(110) substrate and the high Au surface mobility in the presence of the halide adsorbates. The different orientation of the islands for the two halide adsorbate species might be related to the structural differences in the corresponding halide adlayers (see section III.H). Similar morphologies as for Au(110)−Br were also observed on Pt(110) electrode surfaces previously exposed to bromine or iodine vapor, suggesting that the formation of these quasiperiodic nanoscale features is not a singular phenomenon but exist also in other systems.

VII. Influence on Electrochemical Reactivity

A. Metal Growth/Dissolution

Electrochemical dissolution and deposition processes are of fundamental as well as of great practical importance in metal corrosion, etching, plating, and metal refinement processes. As suggested already in the 1920s by Stranski,[424] the dissolution and the reverse deposition reaction is dominated on the microscopic scale by detachment/attachment of atoms at the low coordination kink sites on the crystal

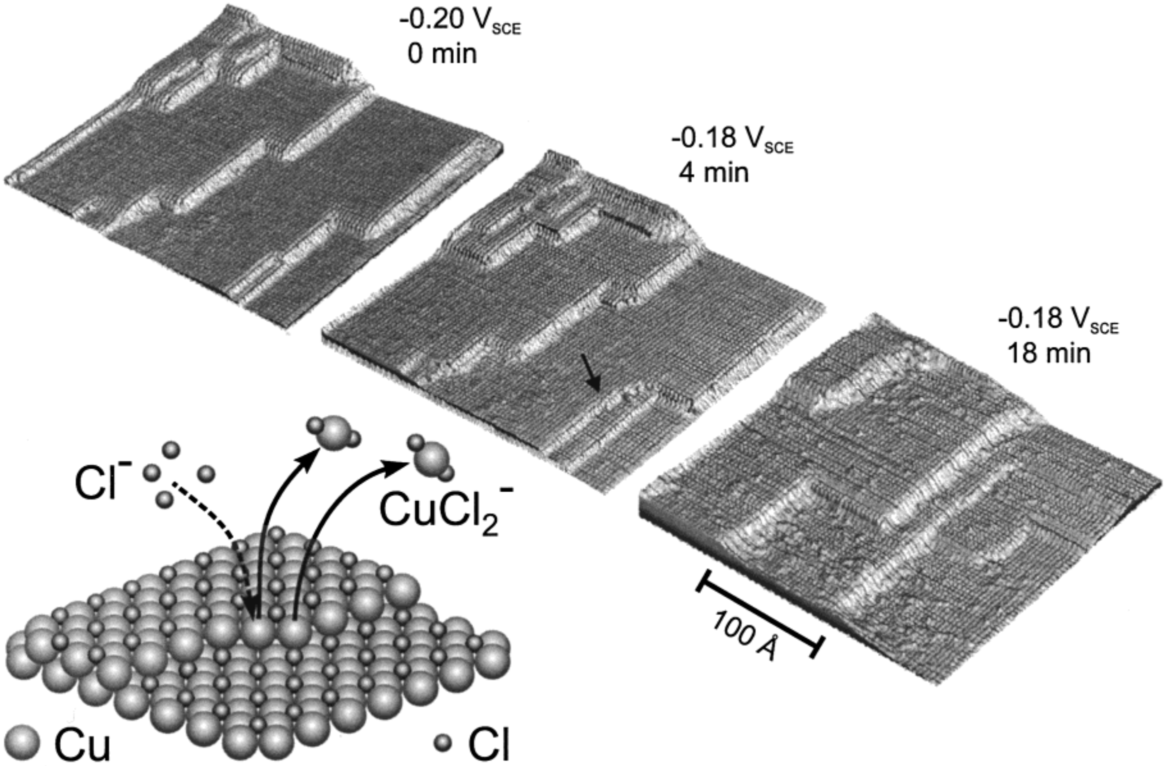

Figure 23. Sequence of high-resolution in situ STM images showing the step flow dissolution via removal at kink sites on the *c*(2 × 2) Cl-covered Cu(100) surface in 1 mM HCl. The model illustrates the elementary steps in the dissolution process. (Reprinted with permission from ref 43. Copyright 1999 Material Research Society.)

surface. These kink sites are preserved during the removal or addition of the basic building blocks of the crystal, e.g., the single metal atoms for simple metal electrodes, and hence can sustain a continuous dissolution or deposition reaction. As shown above, specifically adsorbed anions can strongly alter the type and distribution of defects, such as kinks, on the electrode surface, in particular in the range of the ordered adlayer phases. The pronounced influence of these species on deposition and dissolution processes, well-known from traditional electrochemical and microscopic studies, is therefore not surprising. Detailed high-resolution in situ STM studies on the effect of anion adlayers on these processes have focused primarily on the dissolution in solutions, which are (initially) free of the metal ions and hence exhibit a potential regime where the surface morphology is stable. Similar investigations of homoepitaxial electrodeposition processes are much more difficult, since in this case pronounced exchange of metal ions with the electrolyte occurs in the entire potential range, resulting in a highly dynamic surface morphology. Heteroepitaxial systems—although considerably more studied[425]—are not considered here, since the anion effects are often altered or obscured by the pronounced influence of the foreign metal substrate and in general are less well understood.

As an example of the effect of the anion adlayer structure on the mechanism of metal dissolution, we discuss the dissolution of Cu(100) in sulfuric and hydrochloric acid solution. In situ STM studies, which allow one to directly observe the temporal evolution of the local surface morphology during a slow potential increase in the dissolution regime, show that on clean Cu electrode surfaces in pure H_2SO_4 and HCl solutions the anodic Cu dissolution commences exclusively at the steps.[43,178,179,181,182,186,364] In H_2SO_4 solution the anion adlayer is disordered up to the onset of dissolution and the Cu steps exhibit the characteristic frizzy appearance, indicative of a high kink density and a high Cu mobility along the steps (see section VI.B). As demonstrated by Vogt et al., Cu(100) dissolution proceeds in this electrolyte via isotropic, random removal of Cu along the steps, leading to an increasing roughness of the steps.[186] With higher potential, the rate of this step-roughening process and correspondingly the roughness of the steps increase. Strong statistical fluctuation of the local step positions (up to ±100 Å), which can be directly observed in the STM images, indicate that, in addition to the dominant step Cu dissolution, a significant fraction of the dissolved Cu is locally redeposited at other parts of the steps. These observations can be attributed to the high density of reaction sites for the local dissolution/redeposition processes (i.e., kink sites), due to which material removal/redeposition proceed with approximately equal probability along the steps. A very different dissolution behavior is found in the presence of the *c*(2 × 2) Cl adlayer, where the steps are strongly faceted along the {001} directions. During the dissolution process this predominant orientation of the steps is largely preserved, i.e., step roughening does not occur (Figure 23). Atomic-scale studies reveal that the local dissolution proceeds by the same mechanism as the local dissolution and growth processes observed in the double layer potential regime (see section VI.B), i.e., by the removal of $(\sqrt{2} \times \sqrt{2})R45°$ unit cells at well-defined kink sites (an example is marked by an arrow in Figure 23).[186]

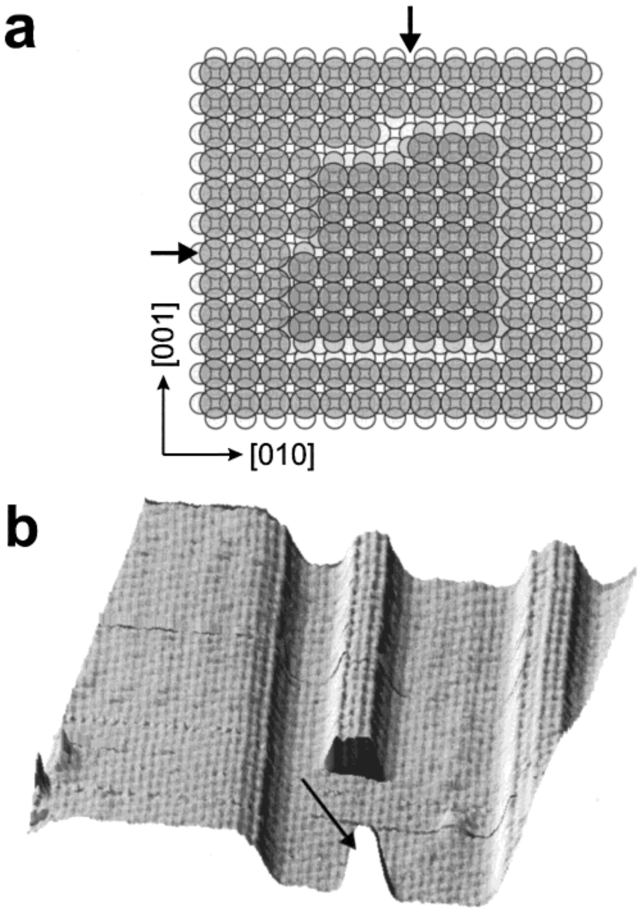

Figure 24. (a) Model showing the structural anisotropy between [010] and [001] oriented steps on $c(2 \times 2)$ Cl-covered Cu(100) (arrows indicate position of kinks). (b) In situ STM observations of Cu(100) during the dissolution at -0.2 V$_{SCE}$ in 10 mM HCl solution (190×110 Å^2). The anisotropic islands were created by pinning impurities (see arrow) and illustrate the different rate of etching at differently oriented steps of the same terrace. (Reprinted with permission from ref 43. Copyright 1999 Material Research Society.)

In this electrolyte Cu is dissolved as CuCl$_2^-$ via a two-step process involving the transient formation of a CuCl adsorbate. The Cu dissolution is therefore probably directly coupled with the dissolution of the Cl adsorbate. For stoichiometric reasons and to regenerate the $c(2 \times 2)$ adlayer on the freshly exposed area of the lower Cu terrace, the elementary step of this process, i.e., the dissolution of one $(\sqrt{2} \times \sqrt{2})$R45° unit cell, requires the (temporary) uptake of four additional Cl$^-$ ions from the electrolyte (see the model in Figure 23). A reverse mechanism can be expected for the Cu deposition reaction on Cu(100) in Cl-containing electrolyte at sufficiently low deposition rates.

As a direct geometric consequence of the $c(2 \times 2)$ adlayer structure, two types of steps with different local structure exist, depending on the phase relationship of the $c(2 \times 2)$ adlattices on the lower and upper Cu terrace (Figure 24a). Due to the antiphase shift of the adlattices on both terraces, the edges of the horizontal and vertical running steps, as well as at kinks in these steps, are of different structure, resulting in a corresponding different stability with respect to Cu dissolution. This effect is independent of the precise structure at the step edge, which may differ from that chosen in the model in Figure 24a (see, for example, ref 237). The adsorbate-induced anisotropy is directly observed in the STM experiments, where a predominant dissolution of the Cu terraces along one of the two {001} directions is found.[186] It can be particularly noticed on surfaces contaminated with trace impurities, which can locally stabilize small parts of the more reactive steps ("step pinning") and thus block them from dissolution.[43,186] As a result of this blocking behavior, strongly anisotropic peninsulas and islands are formed on the Cu surface. An example is presented in Figure 24b, which shows a long, anisotropic island of only a few $(\sqrt{2} \times \sqrt{2})$R45° unit cells in width. After having scanned two-thirds of the imaged area (the slow scan direction is from top to bottom), the island was apparently detached from the stabilizing impurity (see arrow in Figure 24b), which resulted in its rapid dissolution. An analysis of the adlattice phase relationship in such images revealed that the vertical running, [001]-oriented steps in the model in Figure 24a correspond to the more reactive step orientation. Recently, this anisotropy in the dissolution behavior could be directly verified by "real-time" observations using video-STM.[423] As shown in the sequence of images in Figure 25, recorded after a potential step into the Cu dissolution regime, the dissolution of the observed terrace proceeds predominantly via sequential removal of $(\sqrt{2} \times \sqrt{2})$R45° rows at the reactive step (indicated by solid white line). Dissolution along the stable steps (dashed white line) occurs only via (temporary) nucleation and "collective" removal of a larger terrace segment (at 200 ms), i.e., a mechanism involving solely nucleation, propagation, and condensation of kinks in reactive steps. The different reactivity of kinks in the two types of steps was tentatively explained by a different coordination of Cu kink atoms with neighboring Cl adsorbates.[423]

These results demonstrate that the structure of the ordered adlayer determines the structure of the reaction site(s) and hence the microscopic kinetics of the dissolution/deposition reaction. Since the reactive kink sites on the $c(2 \times 2)$ Cl-covered surface are of well-defined structure and—due to the very low kink density—sufficiently separated along the steps, Cu(100)−Cl is an ideal system for a detailed, quantitative study of the dissolution dynamics at individual kinks. Determining the rates of these atomic-scale processes, which cannot be measured by macroscopic electrochemical techniques due to problems in establishing the absolute number of kink sites, is of fundamental importance for a detailed understanding of metal dissolution/deposition, in particular if complemented with modern quantum chemical theories of this ion transfer reaction. Unfortunately, the direct observation of kink motion by in situ STM is generally hampered by the high rate of this process, which exceeds the maximum image acquisition rate of conventional STMs (typically a few seconds) by orders of magnitude even at the very onset of Cu dissolution[186] and only recently became possible by video-STM (see above). To directly measure the kink migration velocity, Magnussen and Vogt

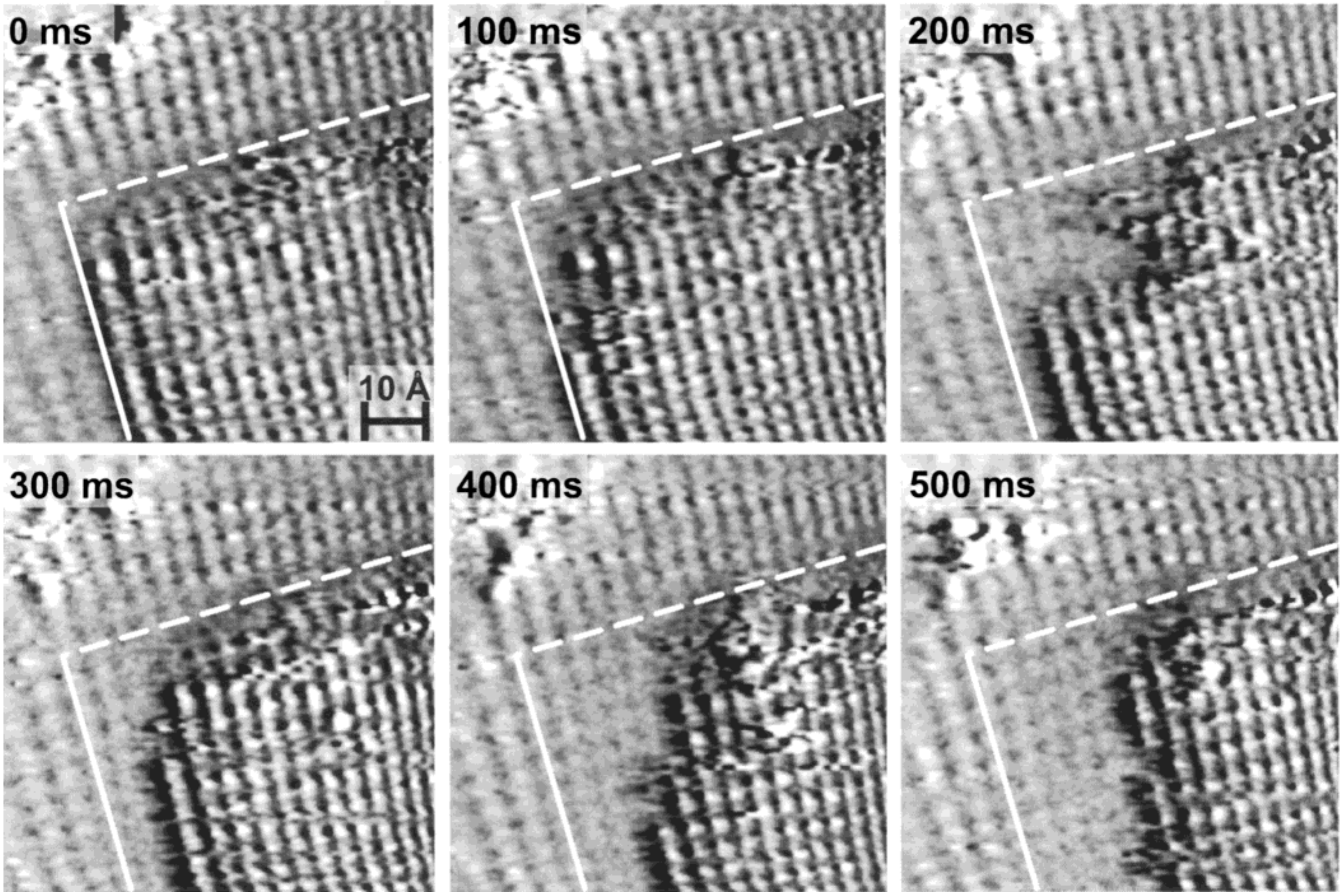

Figure 25. A series of in situ high-speed STM images recorded on Cu(100) in 10 mM HCl after a potential step from −0.23 to −0.17 V_{SCE} (65 × 65 $Å^2$). The images show the progressive dissolution of a Cu terrace, starting at the outer terrace corner, and illustrate the anisotropy in the etching behavior at the active and the stable step (initial positions indicated by solid and dashed lines, respectively) of the terrace. (Reprinted with permission from ref 423. Copyright 2001 Elsevier Science Ltd.)

developed a novel technique, called time-of-walk (TOW) measurements, which is illustrated in Figure 26a,b.[426] In this technique STM scan lines are recorded across an approximately perpendicular running step alternately at two locations (y_1 and y_2), separated by a distance Δy. At each location the passing of a kink manifests as a distinct change in the step position along x by one or two (see below) ($\sqrt{2} \times \sqrt{2}$)R45° unit cell widths. The time difference Δt between the positional changes at y_1 and y_2 then corresponds to the propagation time of the kink from y_1 to y_2. From a statistical analysis of these experiments, the normalized distribution of the kink propagation times for the dissolution of a single ($\sqrt{2} \times \sqrt{2}$)R45° row is obtained, which is presented in Figure 26c for two potentials in the regime of low dissolution rates. The shape of these distributions strongly indicates pronounced positional fluctuations of the kinks along the steps caused by competing dissolution and redeposition processes. Such parallel dissolution and growth are expected from macroscopic electrochemical measurements and can be directly observed in the video-STM experiments (see Figure 25). They are the microscopic basis for the exchange current density, one of the central kinetic parameters of electrochemical reactions. According to fits (shown in Figure 26c) of the data by a simple quantitative model, where the kink migration is described as a one-dimensional random walk with slightly different probabilities for steps in the two directions, the reaction rate at kinks ($\bar{k}$) is about 2 orders of magnitude larger than the average rate of kink propagation (Δk), i.e., the rates of dissolution and redeposition differ by less than 1%.[426] These results directly demonstrate that each kink simultaneously acts as active site both for the dissolution and the reverse deposition reaction. The average kink propagation rates were in good agreement with direct observation by video-STM[423] and estimates obtained from macroscopic electrochemical measurements on the same Cu(100) sample.[426] In addition, the experiments suggest a second, less frequent dissolution mechanism involving the collective removal of two ($\sqrt{2} \times \sqrt{2}$)R45° parallel rows, which was not conceived in previous models of crystal dissolution. Future studies by this method, where the temporal resolution is improved by utilizing a high-speed STM, should provide detailed quantitative data on the dynamics of the dissolution/deposition reaction.

The same dissolution mechanism, i.e., the removal of ($\sqrt{2} \times \sqrt{2}$)R45° unit cells at kink sites, was found by Nakakura and Altman for the reactive etching of Cu(100) by Cl_2 and Br_2 under UHV conditions,[231,236−238,427] demonstrating the domination of these processes by the chemisorbed adlayer and its influence on the structure of surface defects, independent of the environment. Furthermore, this mechanism of metal dissolution is not unique to

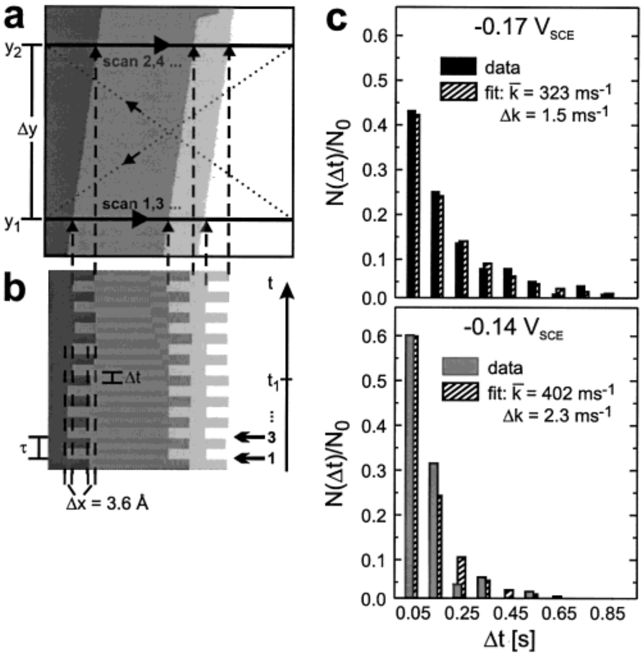

Figure 26. Quantitative measurements of kink propagation velocities during Cu(100) dissolution in 10 mM HCl by the TOW method. (a) Path of the scanning tip, superimposed on an STM image (170×450 Å^2) recorded at -0.25 V_{SCE} prior to Cu dissolution. (b) Small part of the TOW data, recorded after a potential step to -0.14 V_{SCE} at positions y_1 and y_2 ($\Delta y = 306$ Å; time per TOW cycle $\tau = 0.1$ s). At time t_1, a kink in the leftmost step with a width of 3.6 Å, i.e., one $(\sqrt{2} \times \sqrt{2})$R45° unit, passes through y_1 and y_2. (c) Normalized distribution $N(\Delta t)/N_0$ of the kink propagation times Δt for -0.17 and -0.14 V_{SCE} (data columns correspond to $i = 0-8$ TOW cycles passed in the interval Δt). The striped columns are results of fits to the statistical model. (Adapted from ref 426.)

Cu(100) but also governs the dissolution of other $c(2 \times 2)$ covered surfaces. As shown by Itaya and coworkers it is found for Pd(100)−I,[201,202] Ni(100)−S,[308,309] and Ag(100)−I,[177] although the length of the ⟨001⟩-oriented step segments was usually shorter than on Cu(100). Interestingly, the anion adlayer was preadsorbed prior to immersion in these systems, i.e., not present as a solution species. Nevertheless, the ordered adlayer phase was maintained on the surface, even after prolonged metal dissolution, which was interpreted in a model where the removal of metal atoms at the kink sites is accompanied by a step down of the anion at the kink from the upper to the lower terrace.[177,201,202,308,309] Hence, in these systems the adlayer does not participate directly in the reaction as for Cu(100)−Cl but solely acts as a surface-confined species (“surfactant”), which determines the structure of the active sites of the dissolution/deposition reaction.

Also during the dissolution of (111)- and (110)-oriented metal electrodes surfaces, a particular stability of steps running along close-packed directions of the ordered anion adlayer was observed, indicating an analogous influence of the adlayer on the dissolution process as for (100) surfaces. Examples include the systems Cu(111)−Cl,[31,178] Au(111)−Cl,[428] and Ni(111)−I,[204] where a preference for ⟨211⟩-oriented steps was found, as well as Cu(110)−Cl,[280] where steps along [001] were preferred. Interestingly, a dissolution mechanism involving the anion-induced stabilization of certain step orientations is even found in the presence of high-order commensurate or incommensurate adlayer phases, where the structure of the step edge is less well defined as for simple commensurate adlayers. As already mentioned in section VI.B, the oriented step segments in this case often seem to be straight only on the nanometer scale and the atomic structure differs locally. An even more complex behavior is observed in the presence of anisotropic adlayer phases, as shown by Polewska et al. for the sulfate adlayer on Cu(111).[364] Here the Cu steps are oriented approximately parallel to the Moiré pattern in the double layer potential range, i.e., run along one of the three close-packed directions of the underlying, reconstructed Cu surface layer (Figure 27a).[31,43,355,362,364] At potentials close to the onset of Cu dissolution, a step flow mechanism is found, where an apparently disordered phase emerges on the freshly exposed Cu terraces below the dissolving step (Figure 27b−d). This phase can be attributed to a disordered sulfate adlayer on top of an unreconstructed or an only locally ordered, reconstructed Cu lattice.[364] Due to the anisotropy of the $(\sqrt{3} \times \sqrt{7})$ structure, three different orientations of the sulfate adlayer relative to the step direction are possible, resulting in a corresponding anisotropy in the initial step dissolution rate. As shown by the STM observations (Figure 27b−d), steps running perpendicular to the close-packed direction of the sulfate adlayer (“$\sqrt{3}$”-direction) on the lower terrace side (white arrows) are more stable than those running at a 30° angle to this direction (black arrows).[364] This can be correlated with the sulfate packing density along the step direction, which is highest for steps oriented perpendicular to the “$\sqrt{3}$”-direction (see Figure 15). Furthermore, these observations indicate that the step is stabilized by the adlayer on the lower terrace rather than by the adlayer on the upper, dissolving terrace. Although this experimental differentiation is only possible for anisotropic adlayer structures, a stabilization of the step from the lower terrace side may be relevant also for other systems.

B. Molecular Adsorption and Electrocatalytic Reactions

Obviously, the presence of specifically adsorbed anions, in particular of high-density, ordered adlayer phases, may strongly affect the adsorption of other species as well as chemical reactions between those coadsorbates. As recognized even before detailed structural data on anion adlayers became available, this should significantly influence the kinetics of electrocatalytic reactions, such as oxygen reduction or hydrogen evolution/oxidation. Since these reactions are of considerable relevance for established and emerging electrochemical technologies, e.g., fuel cells, the relationship between anion adlayer structure and electrocatalytic properties is currently a very active field of research. In the following, some recent studies on well-defined, single crystalline electrodes are described, for which the influence of the anion adlayer structure was explicitly investigated.

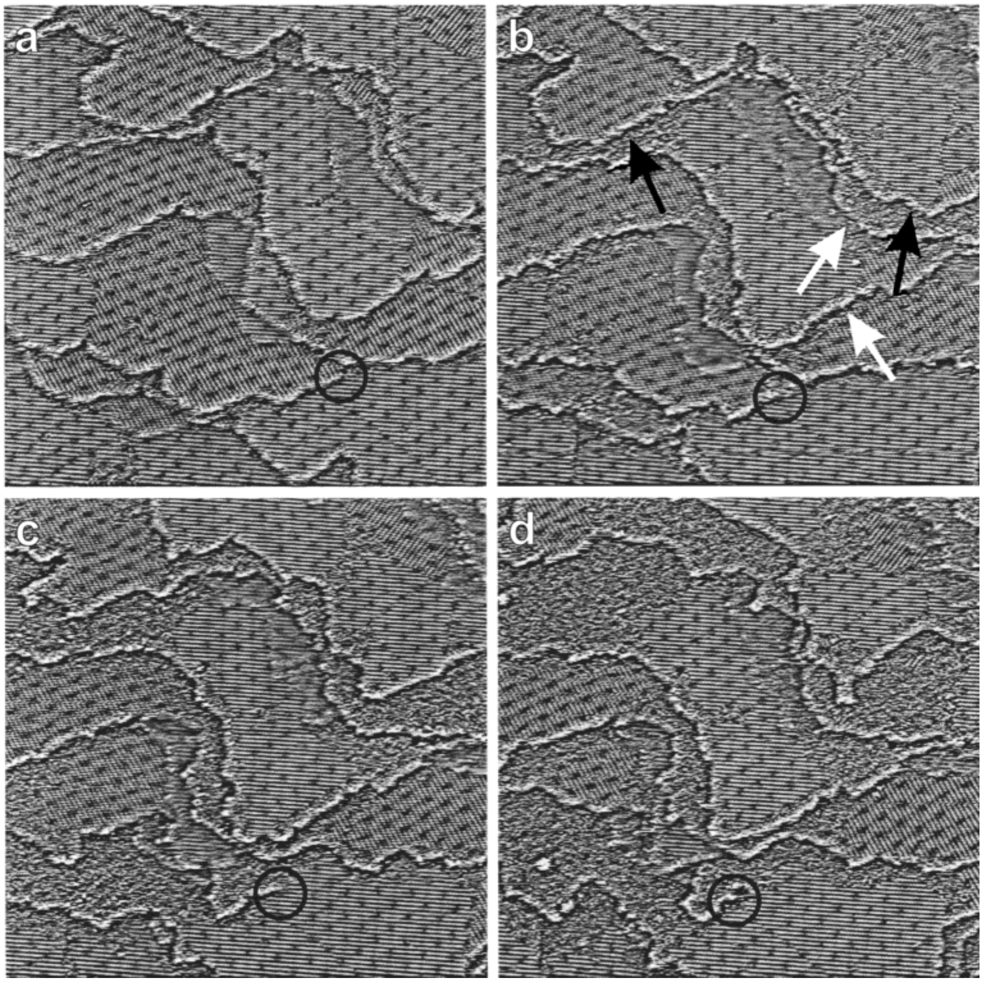

Figure 27. A series of STM images showing the initial stages of Cu(111) dissolution in 10 M H_2SO_4 (700 · 780 Å^2). The images are recorded at (a) −0.30 V (0 min), (b) −0.13 V (7 min), (c) −0.13 V (10 min), and (d) −0.13 V (12.5 min). For better visibility of the sulfate adlayer structure, each of the Cu terraces is colored by a separate gray scale (arrows are described in the text). The circle indicates a screw dislocation, which marks identical surface locations in the images. (Reprinted with permission from ref 364. Copyright 1999 American Chemical Society.)

We first discuss the effect of anion adlayers on the oxygen reduction and the hydrogen evolution reaction. To demonstrate that this effect can be substantial, even for anions that are commonly regarded as only moderately strong specifically adsorbed, Cu(111) in sulfate-containing solution again is chosen as an explicit example. In recent rotating ring-disk measurements, Brisard et al.[429] observed strong inhibition of both reactions on this electrode in the presence of the ($\sqrt{3} \times \sqrt{7}$) sulfate adlayer. Their data for Cu(111) in oxygen-saturated sulfuric and perchloric acid solution are reproduced in Figure 28. Obviously, the oxygen reduction current on Cu in H_2SO_4 solution (Figure 28a, dotted line) is completely blocked at potentials positive of −0.35 V_{SCE}, i.e., in the potential range of the ordered sulfate adlayer. At more negative potentials, where the sulfate adlayer is disordered, the oxygen reduction current is comparable to that in $HClO_4$ solution (Figure 28a, solid line). The ring currents in the two electrolytes (Figure 28b), however, differ also in this potential regime. Contrary to the near-zero current in $HClO_4$ solution, a substantial current is measured in H_2SO_4 solution, indicating a high rate of H_2O_2 production below −0.40 V_{SCE}. This implies a change in reaction mechanism from a four-electron ($HClO_4$ solution) to a two-electron process (H_2SO_4 solution). Apparently, even the disordered sulfate adlayer can block the second step of the oxygen reduction reaction. This was tentatively attributed to changes in the anion adsorption geometry or competition of hydrogen intermediates.[429] Similar inhibition effects were found for the hydrogen evolution reaction.[364,429]

In a similar way, detailed kinetic data on the oxygen reduction reaction on Pt(*hkl*) ring-disk electrodes in perchloric acid, sulfuric acid, and KOH solution were obtained by Markovic et al.[9−11] It was found that the activity of the Pt(111) electrode, which is the most active crystal face in $HClO_4$ and KOH solution, is reduced by about 3 orders of magnitude in H_2SO_4 solution, whereas the activities of Pt(100) and Pt(110) in H_2SO_4 are almost identical to those in KOH and only slightly lower than those in $HClO_4$ solution. As indicated by FTIR spectroscopy,[63,65,338,339,341,342] radiotracer,[335] and in situ STM[353,354] measurements (see section IV.C), sulfate/bisulfate adsorbs much more strongly and at considerably higher coverages on Pt(111) than on Pt(100) and Pt(110) and, moreover, forms a ($\sqrt{3} \times \sqrt{7}$) phase on the (111) surface in the potential range where the O_2-reduction is under combined kinetic-diffusion control. Hence, the pronounced differences in the

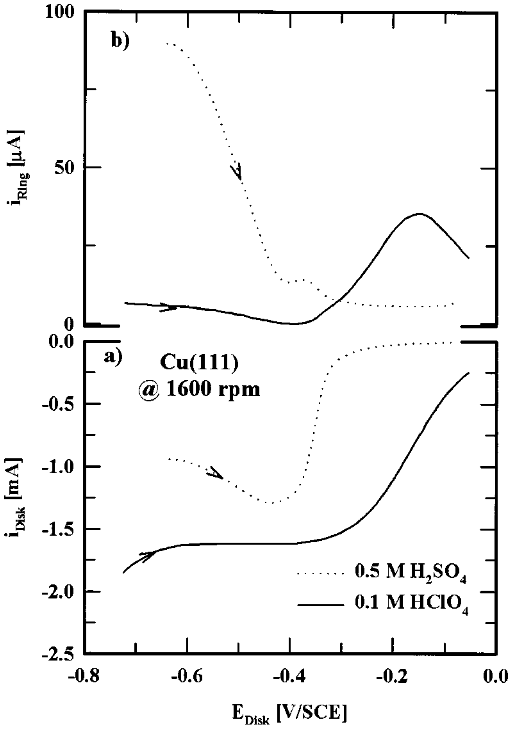

Figure 28. Rotating ring-disk measurements of oxygen reduction on Cu(111) in H_2SO_4 and $HClO_4$ solution (1600 rpm, 10 mV/s), illustrating the effect of the sulfate adlayer on the electrocatalytic reactivity. (a) Cu(111) disk current, (b) detection of H_2O_2 oxidation on the Pt ring ($E_r = 0.95$ V_{SCE}) during the positive potential scanReprinted with permission. (Reprinted with permission from ref 429. Copyright 2000 Elsevier Science Ltd.)

activity of Pt(111) can be attributed to the blocking of active sites for O_2 adsorption by the ordered sulfate adlayer.[9,11] More recently, Wang et al.[14,15] and Markovic et al.[12,13] studied for Pt(111) the effect of Br^- and Cl^- anions on this reaction and found a similar but even stronger inhibition effect, which again can be rationalized by the presence of the close-packed halide adlayers. In addition, both observed the quantitative production of peroxide, indicating that in the presence of adsorbed Br anions the O_2-reduction reaction does not proceed entirely through a four-electron pathway as in $HClO_4$, KOH, and H_2SO_4 solution. It was proposed that the blocking of sites by the Br adsorbate suppresses both the adsorption as well as the dissociation of the O_2 molecules on the electrode surface.[12,15] In situ SXS measurements during the course of oxygen reduction revealed that the (3×3) Br is destabilized by O_2 at potentials negative of 0.55 V_{NHE}, probably due to competitive adsorption/coadsorption of oxygen species.[15] Furthermore, similar combined SXS and rotating-disk measurements were performed by Wang et al.[14,15] on Au(100) and Ag(100) electrodes in Br-containing solution. According to these data, O_2 reduction on Au(100) is completely inhibited by the ordered $c(\sqrt{2} \times 2\sqrt{2})$R45° and $c(\sqrt{2} \times p)$R45° adlayer phases and only takes place in the potential range where the Br adlayer is disordered. On Ag(100) only partial blocking of this reaction was found in the presence of the $c(2 \times 2)$ Br phase, which was explained by O_2 adsorption through the holes of this more open Br lattice in an end-on configuration.[15]

Second, the effect of specifically adsorbed anions on the adsorption of larger molecules is considered, where competitive as well as cooperative effects of anions are found. In a combined in situ STM, FTIR spectroscopy, and electrochemical study, Vogt et al. demonstrated that the organic corrosion inhibitor benzotriazole forms a dense adlayer on Cu(100) and Cu(111) in H_2SO_4 solution but is completely displaced from the electrode surface by the anion adlayer in Cl-containing solution.[364,430−432] Also in this case the molecular adsorption was inhibited predominantly in the range of the ordered adlayer phases, whereas in the potential range of the disordered adlayer phase the benzotriazole adlayer was stable. These observations provide a direct microscopic explanation of the pronounced influence of chloride on the benzotriazole inhibition efficiency. On the other hand, metal electrodes covered by ordered, chemisorbed anion adlayers may constitute an ideal substrate for the formation of well-ordered adlayers of various organic molecules via self-assembly, as demonstrated in detailed in situ STM studies of iodide-covered Au, Ag, and Pt electrodes by the group of Itaya.[36,433−438] In contrast to bare metal surfaces, where the ordering of these molecular adlayers is hindered by the low surface mobility of the strongly chemisorbed molecules, the much weaker van der Waals interactions between these species and the close-packed iodide adlayer underneath and the resulting lower corrugation potential of the iodide-covered surface seem to facilitate organization into structures determined by the lateral intermolecular interactions (for details, see ref 36). These results demonstrate that ordered anion adlayers offer exciting new opportunities for the defined tailoring of the physical and chemical properties of electrode surfaces.

C. Outer-Sphere Reactions

Finally, anion adlayers may also influence outer-sphere electron-transfer reactions, i.e., electrochemical reactions that do not involve adsorption on the electrode surface. This phenomenon was very recently studied by Wakabayashi et al.,[439] using redox reactions of cobalt complexes on Pt(111), Pt(100), and Pt(110) single-crystal electrodes as an example. It was found that these reactions were retarded by chloride, bromide, and iodide adlayers, but accelerated by CN and SCN adlayers. These effects may be caused by anion-induced changes in the potential of zero charge of the electrodes and/or modifications of the electron transfer by the adlayers. In the latter model, the retardation of the reaction in the presence of halide adsorbates could be ascribed to an increase in the effective electron tunneling distance, caused by the outward shift in the plane of closest approach of the Co complexes. The acceleration observed on CN- and SCN-covered electrodes might be explained by electron transfer via intermediate states of the adsorbate (“resonant tunneling”).[439] Also for this type of reaction, the behavior found at the electrochemical interface qualitatively resembles that observed in the corresponding gas phase systems, as shown recently by Casagrande et al.[440] In their study of the electron capture of fluorine atoms on chlorine-covered Ag(111) under UHV conditions, a strong decrease in the electron-transfer rate was found in the presence of a close-packed Cl adlayer that could not be explained by changes in the metal work function alone (corresponding to the changes in *pzc* in the electrochemical system) but had to be attributed to modifications of the local electronic structure by the adsorbate. Although such studies of electron-transfer phenomena at electrochemical and metal–vacuum interfaces are still scarce, they again underline the close relationship between the effect of these adlayer phases on the surface reactivity in both environments.

VIII. Conclusions and Outlook

Over the past decade a detailed microscopic picture of specific anion adsorption at the electrochemical interface has emerged. Significant new insights into the complex interface structure and the atomic-scale mechanisms of reactions at this interface were obtained that considerably broadened the classical, largely thermodynamic double layer models. Although we here have focused on the results of in situ structure-sensitive techniques, it should be emphasized that these achievements were only made possible by the complementary data of a multitude of experimental and theoretical methods. Among the most surprising results is the rich potential-dependent phase behavior, found even for adlayers of simple, atomic anions. Not only disordered phases, as expected from the early electrochemical studies on the (particularly weakly adsorbing) Hg electrode, but also densely packed, ordered adlayers with commensurate as well as compressible, incommensurate structures are formed, which can be rationalized by the competing lateral adsorbate–adsorbate and adsorbate–substrate interactions. In particular, on noble metal electrodes potential-dependent sequences of different ordered phases can be observed, which closely resemble those found in classical quasi-two-dimensional systems. Also for molecular anions ordered adlayer structures are found, which are determined by the more complex interactions between these adsorbates, such as covalent or hydrogen bonding. Furthermore, clear evidence for effects such as coadsorption of cations or solvent molecules as well as for a pronounced influence of anions on the structure and morphology of the metal substrate exists. These structural phenomena can explain the well-known, significant influence of specifically adsorbed anions on the electrochemical reactivity. The precise relationship between anion adlayer structure and electrode reactivity was already explicitly demonstrated in a few well-studied systems.

Despite this progress, considerable challenges in clarifying the structure and dynamics of anion adlayers as well as their influence on the electrochemical reactivity exist. For example, the structure of adlayers formed by larger molecular anions is mostly unknown or—as in the case of sulfate—still under debate. In particular, the incorporation of water or hydronium ions into these adlayers and the role of these species in stabilizing ordered structures are not fully understood. Furthermore, almost no in situ structural data exist for anion adlayers on more reactive metals, such as Fe, Co, Ni, or Al, despite the high technological relevance of the electrochemical behavior of these systems, e.g., in corrosion science. Also, the microscopic mechanisms of reactions at anion-covered electrodes are studied only rudimentarily and on a qualitative level at present. As illustrated for the case of metal dissolution, quantitative measurements of the nanometer scale reactivity in these systems can give access to otherwise unobtainable data and, in the long run, should help to bridge the gap between traditional macroscopic kinetic data and modern theories of ion transfer reactions. Here, improvements in the time resolution of structure-sensitive in situ techniques should offer significant new opportunities. These experimental advances might also allow studies of the largely unknown adsorbate dynamics in anion adlayers. Finally, true insights into the physiochemical nature of these systems will be only possible if these experimental approaches are accompanied by advanced theoretical treatments of the anion adlayer structure (e.g., via density functional calculations in slab geometry) of the potential-dependent phase behavior and—most ambitious—of the mechanisms of electrochemical reactions at these interfaces. In view of the almost ubiquitous presence of specifically adsorbing anions in natural and technological environments, these studies should contribute significantly to the understanding of the structure and reactivity of electrochemical interfaces.

IX. Acknowledgments

The author acknowledges a fellowship and financial support by the Deutsche Forschungsgemeinschaft. In addition, I very much like to thank J. X. Wang, B. O. Ocko, R. Adzic, and T. Wandlowski for the pleasant and fruitful cooperation during my stay at Brookhaven National Laboratory, for extensive discussions, and for their permission to use some of our (partly unpublished) data. I am also deeply indebted to my collaborators in the group in Ulm, namely, F. Möller, M. R. Vogt, A. Lachenwitzer, J. Scherer, W. Polewska, S. Morin, S. Lauterborn, S. Strbac, F. Maroun, B., Gleich, and L. Zitzler; results of their experimental work are partly incorporated in this review. Furthermore, I gratefully acknowledge J. Lipkowski, K. Itaya, M. J. Weaver, and G. Brisard for their permission to reprint some of their STM data and Y. Shingaya, W. Schmickler, and E. Spohr for interesting discussions. Finally, I like to thank R. J. Behm for his ongoing support and stimulating discussions.

X. References

(1) Gouy, H. *Ann. Chim. Phys.* **1903**, [7] *29*, 145.
(2) Gouy, H. *Ann. Chim. Phys.* **1906**, [8] *9*, 75.
(3) Despic, A. R. In *Kinetics and mechanisms of electrode processes*; Conway, B. E., Bockris, J. O'M., Yeager, E., Khan, S. U. M., White, R. E., Eds.; Plenum Press: New York, 1993; pp 451–528.
(4) McBride, J. R.; Soriaga, M. P. *J. Electroanal. Chem.* **1989**, *303*.
(5) Schimpf, J. A.; McBride, J. R.; Soriaga, M. P. *J. Phys. Chem.* **1993**, *97*, 8.
(6) Schimpf, J. A.; Abreu, J. B.; Carrasquillo, A.; Soriaga, M. P. *Surf. Sci.* **1994**, *314*, L909.

(7) Lorenz, W. J.; Yamaoka, H.; Fischer, H. *Ber. Bunsen-Ges. Phys. Chem.* **1963**, *67*, 932.
(8) Eichkorn, G.; Lorenz, W. J.; Albert, L.; Fischer, H. *Electrochim. Acta* **1968**, *13*, 183.
(9) Markovic, N.; Gasteiger, H. A.; Ross, P. N. *J. Phys. Chem.* **1995**, *99*, 3411.
(10) Markovic, N.; Gasteiger, H. A.; Ross, P. N. *J. Phys. Chem.* **1996**, *100*, 6715.
(11) Markovic, N.; Gasteiger, H.; Ross, P. N. *J. Electrochem. Soc.* **1997**, *144*, 1591.
(12) Markovic, N. M.; Gasteiger, H. A.; Grgur, B. N.; Ross, P. N. *J. Electroanal. Chem.* **1999**, *467*, 157.
(13) Stamenkovic, V.; Markovic, N. M.; Ross, P. N. *J. Electroanal. Chem.* **2001**, *500*, 44.
(14) Wang, J. X.; Marinkovic, N. S.; Adzic, R. R. *Colloid Surf. A* **1998**, *134*, 165.
(15) Adzic, R. R.; Wang, J. X. *Electrochim. Acta* **2000**, *45*, 4203.
(16) Frumkin, A. N. *Z. Phys. Chem.* **1933**, *164A*, 121.
(17) Grahame, D. C. *Chem. Rev.* **1947**, *41*, 441.
(18) Habib, M. A. In *Comprehensive treatise of electrochemistry*; Bockris, J. O'M., Conway, B. E., Yeager, E., Eds.; Plenum Press: New York, 1980; Vol. 1, pp 135−220.
(19) Hamelin, A.; Vitanov, T.; Sevastyanov, E.; Popov, A. *J. Electroanal. Chem.* **1983**, *145*, 225.
(20) Scherson, D. A.; Kolb, D. M. *J. Electroanal. Chem.* **1984**, *176*, 353.
(21) Al Jaaf-Golze, K.; Kolb, D. M.; Scherson, D. A. *J. Electroanal. Chem.* **1986**, *200*, 353.
(22) Angerstein-Kozlowska, H.; Conway, B. E. *J. Electroanal. Chem.* **1987**, *228*, 429.
(23) *Comprehensive treatise of electrochemistry*; Bockris, J. O'M., Conway, B. E., Yeager, E., Eds.; Plenum Press: New York, 1980; Vol. 1.
(24) *Trends in interfacial electrochemistry*; Silva, A. F., Ed.; D. Reidel: Dordrecht, 1986.
(25) Schmickler, W. *Chem. Rev.* **1996**, *96*, 3177.
(26) Ross, P. N.; Wagner, F. T. In *Advances in electrochemistry and electrochemical engineering*; Gerischer, H., Tobias, C., Eds.; Wiley: New York, 1984; Vol. 13, pp 69−112.
(27) Kolb, D. M. *J. Vac. Sci. Technol. A* **1986**, *4*, 1294.
(28) Kolb, D. M. *Z. Phys. Chem., N.F.* **1987**, *154*, 179.
(29) Hubbard, A. T. *Chem. Rev.* **1988**, *88*, 633.
(30) Kolb, D. M.; Lehmpfuhl, G.; Zei, M. S. In *Spectroscopic and diffraction techniques in interfacial electrochemistry. NATO ASI Series C*; Gutiérrez, C., Melendres, C., Eds.; Kluwer: Dordrecht, 1990; pp 361−382.
(31) Broekmann, P.; Wilms, M.; Kruft, M.; Stuhlmann, C.; Wandelt, K. *J. Electroanal. Chem.* **1999**, *467*, 307.
(32) Siegenthaler, H.; Christoph, R. In *Scanning tunneling microscopy and related methods, NATO ASI Series E*; Behm, R. J., Garcia, N., Rohrer, H., Eds.; Kluwer: Dordrecht, 1990; Vol. 184, pp 315−334.
(33) Siegenthaler, H. In *Springer series in surface sciences. Vol 28. Scanning tunneling microscopy I*; Güntherodt, H.-J., Wiesendanger, R., Eds.; Springer: Berlin-Heidelberg, 1992; pp 7−49.
(34) *Nanoscale probes of the solid/Liquid interface*; Gewirth, A. A., Siegenthaler, H., Eds.; Kluwer Academic Publishers: Dordrecht-Boston-London, 1995.
(35) Gewirth, A. A.; Niece, B. K. *Chem. Rev.* **1997**, *97*, 1129.
(36) Itaya, K. *Prog. Surf. Sci.* **1998**, *58*, 121.
(37) Yau, S.-L.; Vitus, C. M.; Schardt, B. C. *J. Am. Chem. Soc.* **1990**, *112*, 3677.
(38) Gao, X.; Weaver, M. J. *J. Am. Chem. Soc.* **1992**, *114*, 8544.
(39) Gao, X.; Weaver, M. J. *Ber. Bunsen-Ges. Phys. Chem.* **1993**, *97*, 507.
(40) Tao, N. J.; Lindsay, S. M. *J. Phys. Chem.* **1992**, *96*, 5213.
(41) Magnussen, O. M.; Hageböck, J.; Hotlos, J.; Behm, R. J. *Faraday Discuss.* **1992**, *94*, 329.
(42) Broekmann, P.; Wilms, M.; Wandelt, K. *Surf. Rev. Lett.* **1999**, *6*, 907.
(43) Magnussen, O. M.; Behm, R. J. *Mater. Res. Bull.* **1999**, *24*, 16.
(44) Müller, U.; Carnal, D.; Siegenthaler, H.; Schmidt, E.; Lorenz, W. J.; Obretenov, W.; Schmidt, U.; Staikov, G.; Budevski, E. *Phys. Rev. B* **1992**, *46*, 12899.
(45) Batina, N.; Yamada, T.; Itaya, K. *Langmuir* **1995**, *11*, 4568.
(46) Magnussen, O. M.; Wang, J. X.; Adzic, R. R.; Ocko, B. M. *J. Phys. Chem.* **1996**, *100*, 5500.
(47) Schardt, B. C.; Yau, S. L.; Rinaldi, F. *Science* **1989**, *243*, 1050.
(48) Vogel, R.; Baltruschat, H. *Ultramicroscopy* **1992**, *42−44*, 562.
(49) Wintterlin, J.; Behm, R. J. In *Springer Series in Surfaces Sciences, Vol 20. Scanning Tunneling Microscopy I*; Güntherodt, H.-J., Wiesendanger, R., Eds.; Springer: Berlin-Heidelberg, 1992; pp 40−78.
(50) Sautet, P. *Chem. Rev.* **1997**, *97*, 1097.
(51) *Synchrotron techniques in interfacial electrochemistry*; Melendres, C. A., Tadjeddine, A., Eds.; Kluwer Academic Publishers: Dordrecht-Boston-London, 1993.
(52) Toney, M. F.; Ocko, B. M. *Synchroton Radiat. News* **1993**, *6*, 28.
(53) Toney, M. F.; McBreen, J. *Interface* **1993**, *2*, 22.
(54) Wang, J. X.; Adzic, R. R.; Ocko, B. M. In *Interfacial Electrochemistry*; Wieckowski, A., Ed.; Marcel Dekker: New York, 1999; pp 175−186.
(55) Magnussen, O. M.; Ocko, B. M.; Adzic, R. R.; Wang, J. *Phys. Rev. B* **1995**, *51*, 5510.
(56) Magnussen, O. M.; Ocko, B. M.; Wang, J. X.; Adzic, R. R. Unpublished results.
(57) Tadjeddine, A.; Tourillon, G. *Elektrokhimiya* **1992**, *29*, 63.
(58) White, J. H. In *Electrochemical interfaces. Modern techniques for in-situ interface characterization*; Abruña, H. D., Ed.; VCH: New York, 1991; pp 131−192.
(59) Endo, O.; Kiguchi, M.; Yokoyama, T.; Ito, M.; Ohta, T. *J. Electroanal. Chem.* **1999**, *473*, 19.
(60) Blum, L.; Abruña, H. D.; White, J. H.; Gordon, J. G.; Borges, G. L.; Samant, M. G.; Melroy, O. R. *J. Chem. Phys.* **1986**, *85*, 6732.
(61) Tadjeddine, A.; Guay, D.; Ladouceur, M.; Tourillon, G. *Phys. Rev. Lett.* **1991**, *66*, 2235.
(62) Yee, D.; Abruña, H. D. *Langmuir* **1993**, *9*, 2460.
(63) Iwasita, T.; Nart, E. C. In *Advances in electrochemical science and engineering*; Gerischer, H., Tobias, C. W., Eds.; VCH: New York, 1995; pp 126−215.
(64) Ashley, K.; Pons, S. *Chem. Rev.* **1988**, *88*, 673.
(65) Nichols, R. J. In *Adsorption of molecules at metal electrodes*; Lipkowski, J., Ross, R. N., Eds.; VCH: Weinheim-New York, 1992; pp 347−389.
(66) Ataka, K.-I.; Osawa, M. *Langmuir* **1998**, *14*, 951.
(67) Richmond, G. L. In *Electrochemical interfaces. Modern techniques for in-situ interface characterization*; Abruña, H. D., Ed.; VCH: New York, 1991; pp 265−337.
(68) Guyot-Sionnest, P.; Tadjeddine, A. *Chem. Phys. Lett.* **1990**, *172*, 341.
(69) LeRille, A.; Tadjeddine, A.; Peremans, A.; Zheng, W. Q. *Chem. Phys. Lett.* **1997**, *271*, 95.
(70) Tadjeddine, A.; Pluchery, O.; LeRille, A.; Humbert, C.; Buck, M.; Peremans, A.; Zheng, W. Q. *J. Electroanal. Chem.* **1999**, *473*, 25.
(71) Tadjeddine, A.; Le Rille, A. *Electrochim. Acta* **1999**, *45*, 601.
(72) Friedrich, K. A.; Daum, W.; Klünker, C.; Knabben, D.; Stimming, U.; Ibach, H. *Surf. Sci.* **1995**, *335*, 315.
(73) Daum, W.; Dederichs, F.; Müller, J. E. *Phys. Rev. Lett.* **1998**, *80*, 766.
(74) Matranga, C.; Guyot-Sionnest, P. *J. Chem. Phys.* **2000**, *112*, 7615.
(75) Zelenay, P.; Wieckowski, A. In *Electrochemical interfaces. Modern techniques for in-situ interface characterization*; Abruña, H. D., Ed.; VCH: New York, 1991; pp 481−527.
(76) Deakin, M. R.; Li, T. T.; Melroy, O. R. *J. Electroanal. Chem.* **1988**, *243*, 343.
(77) Hatchett, D. W.; Gao, X.; Catron, S. W.; White, H. S. *J. Phys. Chem.* **1996**, *100*, 331.
(78) Lei, H.-W.; Uchida, H.; Watanabe, M. *Langmuir* **1997**, *13*, 5312.
(79) Sass, J. K.; Bange, K. In *Electrochemical surface science*; Soriaga, M. P., Ed.; American Chemical Society: Washington, 1988; pp 54−64.
(80) Sass, J. K.; Lackey, D.; Schott, J.; Straehler, B. *Surf. Sci.* **1991**, *247*, 239.
(81) Stuve, E. M.; Bange, K.; Sass, J. K. In *Trends in interfacial electrochemistry, Vol C 179, NATO ASI Series*; Silva, A. F., Ed.; D. Reidel: Dordrecht, 1986; pp 255−280.
(82) Wagner, F. T. In *Frontiers in Electrochemistry, Vol 2: Structure of electrified interfaces*; Lipkowski, J., Ross, R. N., Eds.; VCH: New York, 1993; pp 310−400.
(83) Pacchioni, G.; Bagus, P. S.; Philpott, M. R. *Z. Phys. D* **1989**, *12*, 543.
(84) Pacchioni, G.; Bagus, P. S.; Philpott, M. R.; Nelin, C. J. *Int. J. Quantum Chem.* **1990**, *38*, 675.
(85) Rubio, J.; Ricart, J. M.; Casanovas, J.; Blanco, M.; Illas, F. *J. Electroanal. Chem.* **1993**, *359*, 105.
(86) Ignaczak, A.; Gomes, J. A. N. F. *J. Electroanal. Chem.* **1997**, *420*, 71.
(87) Koper, M. T. M.; van Santen, R. A. *Surf. Sci.* **1999**, *422*, 118.
(88) Schmickler, W. *Annu. Rep. Prog. Chem., Sect. C.* **1999**, *95*, 117.
(89) Glosli, J. N.; Philpott, M. R. *J. Chem. Phys.* **1992**, *99*, 6962.
(90) Glosli, J. N.; Philpott, M. R. *J. Chem. Phys.* **1993**, *98*, 9995.
(91) Philpott, M. R.; Glosli, J. N.; Zhu, S.-B. *Surf. Sci.* **1995**, *335*, 422.
(92) Philpott, M. R.; Glosli, J. N. *J. Electrochem. Soc.* **1995**, *142*, L25.
(93) Philpott, M. R.; Glosli, J. N. *J. Electroanal. Chem.* **1996**, *409*, 65.
(94) Spohr, E. *Chem. Phys. Lett.* **1993**, *207*, 214.
(95) Spohr, E. *Electrochim. Acta* **1999**, *44*, 1697.
(96) Benjamin, I. *Chem. Rev.* **1995**, *96*, 1449.
(97) Huckaby, D. A.; Blum, L. *J. Electroanal. Chem.* **1991**, *315*, 255.
(98) Blum, L.; Huckaby, D. A. *J. Electroanal. Chem.* **1994**, *379*, 35.
(99) Brown, G.; Rikvold, P. A.; Novotny, M. A.; Wieckowski, A. *J. Electrochem. Soc.* **1999**, *146*, 1035.
(100) Rikvold, P. A.; Wieckowski, A.; Ramos, R. A. *Mater. Res. Soc. Symp. Proc.* **1997**, *451*, 69.
(101) Koper, M. T. M. *J. Electroanal. Chem.* **1998**, *450*, 189.

(102) Lipkowski, J.; Shi, Z.; Chen, A.; Pettinger, B.; Bilger, Ch. *Electrochim. Acta* **1998**, *43*, 2875.
(103) Kolb, D. M.; Schneider, J. *Electrochim. Acta* **1986**, *31*, 929.
(104) Zei, M. S.; Lehmpfuhl, G.; Kolb, D. M. *Surf. Sci.* **1989**, *221*, 23.
(105) Friedrich, A.; Shannon, C.; Pettinger, B. *Surf. Sci.* **1991**, *251/252*, 587.
(106) Wang, J.; Davenport, A. J.; Isaacs, H. S.; Ocko, B. M. *Science* **1991**, *255*, 1416.
(107) Tao, N. J.; Lindsay, S. M. *Surf. Sci.* **1992**, *274*, L546.
(108) Wang, J.; Ocko, B. M.; Davenport, A. J.; Isaacs, H. S. *Phys. Rev. B* **1992**, *46*, 10321.
(109) Kolb, D. M. In *Frontiers in Electrochemistry, Vol. 2: Structure of electrified interfaces*; Lipkowski, J., Ross, R. N., Eds.; VCH: New York, 1993; pp 65−102.
(110) Ocko, B. M.; Magnussen, O. M.; Adzic, R. R.; Wang, J.; Shi, Z.; Lipkowski, J. *J. Electroanal. Chem.* **1994**, *376*, 35.
(111) Kolb, D. M. *Prog. Surf. Sci.* **1996**, *51*, 109.
(112) Foresti, M. L.; Innocenti, M.; Forni, F.; Guidelli, R. *Langmuir* **1998**, *14*, 7008.
(113) Wandlowski, Th.; Wang, J. X.; Ocko, B. M. *J. Electroanal. Chem.* **2001**, *500*, 418.
(114) Li, N.; Lipkowski, J. *J. Electroanal. Chem.* **2000**, *491*, 95.
(115) Lorenz, W. J.; Salié, G. *Z. Phys. Chem.* **1963**, *218*, 259.
(116) Schmickler, W. *Interfacial electrochemistry*; Oxford University Press: New York-Oxford, 1996.
(117) Vetter, K. J.; Schultze, J. W. *Ber. Bunsen-Ges. Phys. Chem.* **1972**, *76*, 920.
(118) Lorenz, W. J. *J. Electroanal. Chem.* **1985**, *191*, 31.
(119) Schultze, J. W.; Rolle, D. *Can. J. Chem.* **1997**, *75*, 1750.
(120) Schultze, J. W.; Koppitz, F. D. *Electrochim. Acta* **1976**, *21*, 327.
(121) Chen, A.; Shi, Z.; Bizzoto, D.; Lipkowski, J.; Pettinger, B.; Bilger, Ch. *J. Electroanal. Chem.* **1999**, *467*, 342.
(122) Ocko, B. M.; Watson, G. M.; Wang, J. *J. Phys. Chem.* **1994**, *98*, 897.
(123) Ocko, B. M.; Magnussen, O. M.; Wang, J. X.; Adzic, R. R. *Physica B* **1996**, *221*, 238.
(124) Kastanas, G. N.; Koel, B. E. *Appl. Surf. Sci.* **1993**, *64*, 235.
(125) Bertel, E.; Netzer, F. P. *Surf. Sci.* **1980**, *97*, 409.
(126) Forstmann, F.; Berndt, W.; Büttner, P. *Phys. Rev. Lett.* **1973**, *30*, 17.
(127) Head, J. D.; Mitchell, K. A. R.; Noodleman, L. *Surf. Sci.* **1976**, *61*, 661.
(128) Citrin, P. H.; Eisenberger, P.; Hewitt, R. C. *Phys. Rev. Lett.* **1978**, *41*, 309.
(129) Maglietta, M.; Zanazzi, E.; Bardi, U.; Sondericker, D.; Jona, F.; Marcus, P. M. *Surf. Sci.* **1982**, *123*, 141.
(130) Lamble, G. M.; Brooks, R. S.; Ferrer, S.; King, D. A.; Norman, D. *Phys. Rev. B* **1986**, *34*, 2975.
(131) Crapper, M. D.; Riley, C. E.; Sweeney, P. J. J.; McConville, C. F.; Woodruff, D. P.; Jones, R. G. *Surf. Sci.* **1987**, *182*, 213.
(132) Woodruff, D. P.; Seymour, D. L.; McConville, C. F.; Riley, C. E.; Crapper, M. D.; Prince, N. P.; Jones, R. G. *Phys. Rev. Lett.* **1987**, *58*, 1460.
(133) Wang, L.-Q.; Hussain, Z.; Huang, Z. Q.; Schach von Wittenau, A. E.; Lindle, D. W.; Hirley, D. A. *Phys. Rev. B* **1991**, *44*, 13711.
(134) Funabashi, M.; Yokoyama, T.; Takata, Y.; Ohta, T.; Kitajima, Y.; Kuroda, H. *Surf. Sci.* **1991**, *242*, 59.
(135) Takata, Y.; Sato, H.; Yagi, S.; Yokoyama, T.; Ohta, T.; Kitajima, Y. *Surf. Sci.* **1992**, *265*, 111.
(136) Barnes, C. J.; Wander, A.; King, D. A. *Surf. Sci.* **1993**, *281*, 33.
(137) Shard, A. G.; Dhanak, V. R.; Santoni, A. *Surf. Sci.* **1999**, *429*, 279.
(138) Endo, O.; Kondoh, H.; Yonamoto, Y.; Yokoyama, T.; Ohta, T. *Surf. Sci.* **2000**, *463*, 135.
(139) Shard, A. G.; Dhanak, V. R.; Santoni, A. *Surf. Sci.* **2001**, *445*, 309.
(140) Lucas, C. A.; Markovic, N.; Ross, P. N. *Surf. Sci.* **1995**, *340*, L949.
(141) Markovic, N. M.; Lucas, C. A.; Gasteiger, H. A.; Ross, P. N. *Surf. Sci.* **1996**, *365*, 229.
(142) Lucas, C. A.; Markovic, N. M.; Ross, P. N. *Phys. Rev. B* **1997**, *55*, 7964.
(143) Gao, X.; Weaver, M. J. *J. Phys. Chem.* **1986**, *90*, 4057.
(144) Franke, C.; Piazza, G.; Kolb, D. M. *Electrochim. Acta* **1989**, *34*, 67.
(145) Kolb, D. M.; Franke, C. *Appl. Phys.* **1989**, *A49*, 379.
(146) Pettinger, B.; Bilger, Ch. *Chem. Phys. Lett.* **1998**, *286*, 355.
(147) Dowben, P. A. *CRC Crit. Rev. Solid State Mater. Sci.* **1987**, *13*, 191.
(148) Bagus, P. S.; Pacchioni, G.; Philpott, M. R. *J. Chem. Phys.* **1989**, *90*, 4287.
(149) Tang, H.-R.; Wang, W.-N.; Li, Z.-H.; Dai, W.-L.; Fan, K.-N.; Deng, J.-F. *Surf. Sci.* **2000**, *450*, 133.
(150) Sellers, H.; Patrito, E. M.; Paredes Olivera, P. *Surf. Sci.* **1996**, *356*, 222.
(151) Kramar, T.; Vogtenhuber, D.; Podloucky, R.; Neckel, A. *Electrochim. Acta* **1995**, *40*, 43.
(152) Kairys, V.; Head, J. D. *Surf. Sci.* **1999**, *440*, 169.
(153) Pecina, O.; Schmickler, W.; Spohr, E. *J. Electroanal. Chem.* **1995**, *394*, 29.
(154) Pecina, O.; Schmickler, W.; Spohr, E. *J. Electroanal. Chem.* **1996**, *405*, 239.
(155) Pecina, O.; Schmickler, W. *J. Electroanal. Chem.* **1998**, *450*, 303.
(156) Ignaczak, A.; Gomes, J. A. N. F.; Romanowski, S. *J. Electroanal. Chem.* **1998**, *450*, 175.
(157) Spohr, E. In *Advances in electrochemical science and engineering*; Alkire, R. C., Kolb, D. M., Eds.; VCH: Weinheim, 1999; Vol. 6, pp 1−76.
(158) Haiss, W.; Sass, J. K.; Gao, X.; Weaver, M. J. *Surf. Sci.* **1992**, *274*, L593.
(159) Sugita, S.; Abe, T.; Itaya, K. *J. Phys. Chem.* **1993**, *97*, 8780.
(160) Gao, X.; Edens, G. J.; Liu, F.-C.; Hamelin, A.; Weaver, M. J. *J. Phys. Chem.* **1994**, *98*, 8086.
(161) Gao, X.; Edens, G. J.; Weaver, M. J. *J. Phys. Chem.* **1994**, *98*, 8074.
(162) Yamada, T.; Batina, N.; Itaya, K. *J. Phys. Chem.* **1995**, *99*, 8817.
(163) Yamada, T.; Batina, N.; Itaya, K. *Surf. Sci.* **1995**, *335*, 204.
(164) Ocko, B. M.; Magnussen, O. M.; Wang, J. X.; Wandlowski, T. *Phys. Rev. B* **1996**, *53*, R7654.
(165) Wandlowski, T.; Wang, J. X.; Magnussen, O. M.; Ocko, B. M. *J. Phys. Chem.* **1996**, *100*, 10277.
(166) Wang, J. X.; Watson, G. M.; Ocko, B. M. *J. Phys. Chem.* **1996**, *100*, 6672.
(167) Wang, J.; Watson, G. M.; Ocko, B. M. Unpublished results.
(168) Wang, J. X.; Adzic, R. R.; Wandlowski, T.; Magnussen, O. M.; Ocko, B. M. Unpublished results.
(169) Cuesta, A.; Kolb, D. M. *Surf. Sci.* **2000**, *465*, 310.
(170) Zou, S.; Gao, X.; Weaver, M. J. *Surf. Sci.* **2000**, *452*, 44.
(171) Aloisi, G.; Funtikov, A. M.; Will, T. *J. Electroanal. Chem.* **1994**, *370*, 297.
(172) Foresti, M. L.; Aloisi, G.; Innocenti, M.; Kobayashi, H.; Guidelli, R. *Surf. Sci.* **1995**, *335*, 241.
(173) Sneddon, D.; Gewirth, A. A. *Surf. Sci.* **1995**, *343*, 185.
(174) Yamada, T.; Ogaki, K.; Okubo, S.; Itaya, K. *Surf. Sci.* **1996**, *369*, 321.
(175) Ocko, B. M.; Wang, J. X.; Wandlowski, T. *Phys. Rev. Lett.* **1997**, *79*, 1511.
(176) Ocko, B. M.; Wandlowski, T. *Mater. Res. Soc. Symp. Proc.* **1997**, *451*, 55.
(177) Teshima, T.; Ogaki, K.; Itaya, K. *J. Phys. Chem. B* **1997**, *101*, 2046.
(178) Suggs, D. W.; Bard, A. J. *J. Am. Chem. Soc.* **1994**, *116*, 10725.
(179) Suggs, D. W.; Bard, A. J. *J. Phys. Chem.* **1995**, *99*, 8349.
(180) LaGraff, J. R.; Gewirth, A. A. *Surf. Sci.* **1995**, *326*, L461.
(181) Vogt, M. R.; Möller, F.; Schilz, C. M.; Magnussen, O. M.; Behm, R. J. *Surf. Sci.* **1996**, *367*, L33.
(182) Moffat, T. P. *Mater. Res. Soc. Symp. Proc.* **1996**, *404*, 3.
(183) Moffat, T. P. *Mater. Res. Soc. Symp. Proc.* **1997**, *451*, 75.
(184) Kruft, M.; Wohlmann, B.; Stuhlmann, C.; Wandelt, K. *Surf. Sci.* **1997**, *377−379*, 601.
(185) Inukai, J.; Osawa, Y.; Itaya, K. *J. Phys. Chem. B* **1998**, *102*, 10034.
(186) Vogt, M. R.; Lachenwitzer, A.; Magnussen, O. M.; Behm, R. J. *Surf. Sci.* **1998**, *399*, 49.
(187) Moffat, T. P. *J. Phys. Chem. B* **1998**, *102*, 10020.
(188) Broekmann, P.; Anastasescu, M.; Spaenig, A.; Lisowski, W.; Wandelt, K. *J. Electroanal. Chem.* **2001**, *500*, 241.
(189) Vitus, C. M.; Chang, S.-C.; Schardt, B. C.; Weaver, M. J. *J. Phys. Chem.* **1991**, *95*, 7559.
(190) Vogel, R.; Baltruschat, H. *Surf. Sci.* **1991**, *259*, L739.
(191) Vogel, R.; Kamphausen, I.; Baltruschat, H. *Ber. Bunsen-Ges. Phys. Chem.* **1992**, *96*, 525.
(192) Baltruschat, H.; Bringemeiner, U.; Vogel, R. *Faraday Discuss.* **1992**, *94*, 317.
(193) Shinotsuka, N.; Sashikata, K.; Itaya, K. *Surf. Sci.* **1995**, *335*, 75.
(194) Bittner, A. M.; Wintterlin, J.; Beran, B.; Ertl, G. *Surf. Sci.* **1995**, *335*, 291.
(195) Bittner, A. M.; Wintterlin, J.; Ertl, G. *J. Electroanal. Chem.* **1995**, *388*, 225.
(196) DeSimone, W. L.; Breen, J. J. *Langmuir* **1995**, *11*, 4428.
(197) Tanaka, S.; Yau, S.-L.; Itaya, K. *J. Electroanal. Chem.* **1996**, *396*, 125.
(198) Itaya, K. In *Electrochemical Nanotechnology*; Lorenz, W. J., Plieth, W., Eds.; Wiley-VCH: Weinheim, 1997; pp 137−148.
(199) Inukai, J.; Osawa, Y.; Wakisaka, M.; Sashikata, K.; Kim, Y.-G.; Itaya, K. *J. Phys. Chem. B* **1998**, *102*, 3498.
(200) Orts, J. M.; Gómez, R.; Feliu, J. M. *J. Electroanal. Chem.* **1999**, *467*, 11.
(201) Sashikata, K.; Matsui, Y.; Itaya, K.; Soriaga, M. P. *J. Phys. Chem.* **1996**, *100*, 20027.
(202) Schimpf, J. A.; Abreu, J. B.; Soriaga, M.; Sashikata, K.; Itaya, K. In *Sixth International Symposium on Electrode Processes*; Wieckowski, A., Itaya, K., Eds.; The Electrochemical Society: Pennington, 1996; *Proc. Electrochem. Soc.* 96−8, pp 180−188.
(203) Wan, L.-J.; Yau, S.-L.; Swain, G. M.; Itaya, K. *J. Electroanal. Chem.* **1995**, *381*, 105.
(204) Müller, P.; Ando, S.; Yamada, T.; Itaya, K. *J. Electroanal. Chem.* **1999**, *467*, 282.

(205) Shi, Z.; Lipkowski, J. *J. Electroanal. Chem.* **1994**, *369*, 283.
(206) Wu, S.; Shi, Z.; Lipkowski, J.; Hitchcock, A. P.; Tyliszczak, T. *J. Phys. Chem.* **1997**, *101*, 10310.
(207) Shi, Z.; Lipkowski, J. *J. Phys. Chem.* **1995**, *99*, 4170.
(208) Bondi, A. *J. Phys. Chem.* **1964**, *68*, 441.
(209) Schott, J. H.; White, H. S. *J. Phys. Chem.* **1994**, *98*, 291.
(210) Schott, J.; White, H. S. *J. Phys. Chem.* **1994**, *98*, 297.
(211) Farrell, H. H. In *The chemical physics of solid surfaces and heterogeneous catalysis*; King, D. A., Woodruff, D. P., Eds.; Elsevier: New York, 1984; pp 226−266.
(212) Erley, W.; Wagner, H. *Surf. Sci.* **1977**, *66*, 371.
(213) Goddard, P. J.; Lambert, R. M. *Surf. Sci.* **1977**, *67*, 180.
(214) Goddard, P. J.; Schwaha, K.; Lambert, R. M. *Surf. Sci.* **1978**, *71*, 351.
(215) Westphal, D.; Goldmann, A. *Solid State Commun.* **1980**, *35*, 437.
(216) Cochran, S. A.; Farrell, H. H. *Surf. Sci.* **1980**, *95*, 359.
(217) Farrell, H. H.; Traum, M. M.; Smith, N. V.; Royer, W. A.; Woodruff, D. P.; Johnson, P. D. *Surf. Sci.* **1981**, *102*, 527.
(218) Westphal, D.; Goldmann, A.; Jona, F.; Marcus, P. M. *Solid State Commun.* **1982**, *44*, 685.
(219) Westphal, D.; Goldmann, A. *Surf. Sci.* **1983**, *131*, 113.
(220) Taylor, D. E.; Williams, E. D.; Park, R. L.; Bartelt, N. C.; Einstein, T. L. *Phys. Rev. B* **1985**, *32*, 4653.
(221) Winters, H. F. *J. Vac. Sci. Technol. B* **1985**, *3*, 1376.
(222) Hwang, R. Q.; Williams, E. D.; Bartelt, N. C.; Park, R. L. *Phys. Rev. B* **1988**, *37*, 5870.
(223) Tysoe, W. T.; Lambert, R. M. *Surf. Sci.* **1988**, *199*, 1.
(224) Andryushechkin, B. V.; Eltsov, K. N. *Surf. Sci.* **1992**, *265*, L245.
(225) Motai, K.; Hashizume, T.; Lu, H.; Jeon, D.; Sakurai, T. *Appl. Surf. Sci.* **1993**, *67*, 246.
(226) Eltsov, K. N.; Klimov, A. N.; Yurov, V. Yu.; Shevlyuga, V. M.; Prokhorov, A. M.; Bardi, U.; Galeotti, M. *JETP Lett.* **1995**, *62*, 444.
(227) Kadodwala, M. F.; Davis, A. A.; Scragg, G.; Cowie, B. C. C.; Kerkar, M.; Woodruff, D. P.; Jones, R. G. *Surf. Sci.* **1995**, *324*, 122.
(228) Galeotti, M.; Cortigiani, B.; Torrini, M.; Bardi, U.; Andryushechkin, B. V.; Klimov, A. N.; Eltsov, K. *Surf. Sci.* **1996**, *349*, L164.
(229) Jones, R. G.; Kadodwala, M. *Surf. Sci.* **1997**, *370*, L219.
(230) Kiguchi, M.; Yokoyama, T.; Terada, S.; Sakano, M.; Okamoto, Y.; Ohta, T.; Kitajima, Y.; Kuroda, H. *Phys. Rev. B* **1997**, *56*, 1561.
(231) Nakakura, C. Y.; Phanse, V. M.; Zheng, G.; Altman, E. I. *Mater. Res. Soc. Symp. Proc.* **1997**, *451*, 81.
(232) Nakakura, C. Y.; Phanse, V. M.; Altman, E. I. *Surf. Sci.* **1997**, *370*, L149.
(233) Schennach, R.; Bechthold, E. *Surf. Sci.* **1997**, *380*, 9.
(234) Andryushechkin, B. V.; Eltsov, K.; Shevlyuga, V. M.; Yurov, V. Yu. *Surf. Sci.* **1998**, *407*, L633.
(235) Hu, H.; Yuro, R.; Harrison, I. *Surf. Sci.* **1998**, *411*, 303.
(236) Nakakura, C. Y.; Altman, E. I. *Surf. Sci.* **1998**, *424*, 244.
(237) Nakakura, C. Y.; Altman, E. I. *Surf. Sci.* **1998**, *398*, 281.
(238) Nakakura, C. Y.; Zheng, G.; Altman, E. I. *Surf. Sci.* **1998**, *401*, 173.
(239) Fishlock, T. W.; Pethica, J. B.; Oral, A.; Edgell, R. G.; Jones, F. H. *Surf. Sci.* **1999**, *426*, 212.
(240) Andryushechkin, B. V.; Eltsov, K. N.; Shevlyuga, V. M. *Surf. Sci.* **2000**, *470*, L63.
(241) Andryushechkin, B. V.; Eltsov, K. N.; Shevlyuga, V. M. *Surf. Sci.* **2001**, *472*, 80.
(242) Fukushima, T.; Song, M.-B.; Ito, M. *Surf. Sci.* **2000**, *464*, 193.
(243) Felter, T. E.; Hubbard, A. T. *J. Electroanal. Chem.* **1980**, *100*, 473.
(244) Abraham, F. F. *Phys. Rep.* **1981**, *80*, 339.
(245) Strandburg, K. J. *Rev. Mod. Phys.* **1988**, *60*, 161.
(246) Kern, K.; Comsa, G. In *Chemistry and physics of solid surfaces*; Vanselow, R., Howe, R., Eds.; Springer: Berlin, 1988; pp 65−108.
(247) Persson, B. N. J. *Surf. Sci. Rep.* **1992**, *15*, 1.
(248) Bak, P.; Paczuski, M. In *The chemical physics of solid surfaces*; King, D. A., Woodruff, D. P., Eds.; Elsevier: Amsterdam-London-New York-Tokyo, 1994; pp 1−34.
(249) Frenkel, Y. I.; Kontorowa, T. *Zh. Eksp. Teor. Fiz.* **1938**, *8*, 1340.
(250) Frank, F. C.; van der Merwe, J. H. *Proc. R. Soc. London* **1949**, *198*, 205.
(251) Bak, P.; Mukamel, D.; Villain, J.; Wentowska, K. *Phys. Rev. B* **1979**, *19*, 1610.
(252) Barth, J. V.; Brune, H.; Ertl, G.; Behm, R. J. *Phys. Rev. B* **1990**, *42*, 9307.
(253) Gao, X.; Edens, G. J.; Weaver, M. J. *J. Electroanal. Chem.* **1994**, *376*, 21.
(254) Huang, L.; Zeppenfeld, P.; Horch, S.; Comsa, G. *J. Chem. Phys.* **1997**, *107*, 585.
(255) Fenter, P.; Lu, T. M. *Surf. Sci.* **1985**, *154*, 15.
(256) Kardar, M.; Berker, A. N. *Phys. Rev. Lett.* **1982**, *48*, 1552.
(257) Orts, J. M.; Gómez, R.; Feliu, J. M.; Aldaz, A.; Clavilier, J. *J. Phys. Chem.* **1996**, *100*, 2334.
(258) Naumovets, A. G. In *Phase Transitions and Adsorbate Restructuring at Metal Surfaces*; King, D. A., Woodruff, D. P., Eds.; Elsevier: Amsterdam, 1994; pp 163-213.
(259) Bauer, E.; van der Merwe, J. H. *Phys. Rev. B* **1985**, *33*, 3657.
(260) Novaco, A. D.; McTague, J. P. *Phys. Rev. Lett.* **1977**, *38*, 1286.
(261) McTague, J. P.; Novaco, A. D. *Phys. Rev. B* **1979**, *19*, 5299.
(262) Grey, F.; Bohr, J. *Europhys. Lett.* **1992**, *18*, 717.
(263) Unguris, J.; Bruch, L. W.; Moog, E. R.; Webb, M. B. *Surf. Sci.* **1979**, *87*, 415.
(264) Unguris, J.; Bruch, L. W.; Moog, E. R.; Webb, M. B. *Surf. Sci.* **1981**, *109*, 522.
(265) Kern, K.; David, R.; Palmer, R. L.; Comsa, G. *Phys. Rev. Lett.* **1986**, *56*, 620.
(266) Melroy, O. R.; Toney, M. F.; Borges, G. L.; Samant, M. G.; Kortright, J. B.; Ross, P. N.; Blum, L. *Phys. Rev. B* **1988**, *38*, 10962.
(267) Samant, M. G.; Toney, M. F.; Borges, G. L.; Blum, L.; Melroy, O. R. *J. Chem. Phys.* **1988**, *92*, 220.
(268) Toney, M. F.; Gordon, J. G.; Samant, M. G.; Borges, G. L.; Melroy, O. R.; Yee, D.; Sorensen, L. B. *Phys. Rev. B* **1992**, *45*, 9362.
(269) Wang, X.; Chen, R.; Wang, Y.; He, T.; Liu, F.-C. *J. Phys. Chem. B* **1998**, *102*, 7568.
(270) Stickney, J. L.; Rosasco, S. D.; Salaita, G. N.; Hubbard, A. T. *Langmuir* **1985**, *1*, 66.
(271) Frank, D. G.; Chyan, O. M. R.; Golden, T.; Hubbard, A. T. *J. Phys. Chem.* **1993**, *97*, 3829.
(272) Binder, K.; Landau, D. P. *Surf. Sci.* **1976**, *61*, 577.
(273) Mitchell, S. J.; Brown, G.; Rikvold, P. A. *Surf. Sci.* **2001**, *471*, 125.
(274) Wieckowski, A.; Rosasco, S. D.; Schardt, B. C.; Stickney, J. L.; Hubbard, A. T. *Inorg. Chem.* **1984**, *23*, 565.
(275) Lu, F.; Salaita, G. N.; Baltruschat, H.; Hubbard, A. T. *J. Electroanal. Chem.* **1987**, *227*, 259.
(276) Albers, J.; Baltruschat, H.; Kamphausen, I. *J. Electroanal. Chem.* **1995**, *395*, 99.
(277) Orts, J. M.; Gómez, R.; Feliu, J. M.; Aldaz, A.; Clavilier, J. *Langmuir* **1997**, *13*, 3016.
(278) Gao, X.; Weaver, M. J. *Phys. Rev. Lett.* **1994**, *73*, 846.
(279) Gao, X.; Weaver, M. J. *Surf. Sci.* **1994**, *313*, L775.
(280) Wan, L.-J.; Itaya, K. *J. Electroanal. Chem.* **1999**, *473*, 10.
(281) Li, W. H.; Wang, Y.; Ye, J. H.; Li, S. F. Y. *J. Phys. Chem. B* **2001**, *105*, 1829.
(282) Kosterlitz, J. M.; Thouless, D. J. *J. Phys. C* **1973**, *6*, 1181.
(283) Hanewinkel, C.; Otto, A.; Wandlowski, T. *Surf. Sci.* **1999**, *429*, 255.
(284) Wood, D. W.; Goldfinch, J. *J. Phys. A.: Math. Gen.* **1980**, *13*, 2781.
(285) Kinzel, W.; Schick, M. *Phys. Rev. B* **1981**, *24*, 324.
(286) Mitchell, S. J.; Brown, G.; Rikvold, P. A. *J. Electroanal. Chem.* **2000**, *493*, 68.
(287) Pokrofsky, V. L.; Talapov, A. L. *Phys. Rev. Lett.* **1979**, *42*, 66.
(288) Emery, V. J.; Axe, J. D. *Phys. Rev. Lett.* **1978**, *40*, 1507.
(289) Innocenti, M.; Foresti, M. L.; Fernandez, A.; Forni, F.; Guinet, G. *J. Phys. Chem. B* **1998**, *102*, 9667.
(290) *Kinetics and mechanisms of electrode processes*; Conway, B. E., Bockris, J. O'M., Yeager, E., Khan, S. U. M., White, R. E., Eds.; Plenum Press: New York, 1993.
(291) Strbac, S.; Adzic, R. R. *J. Electroanal. Chem.* **1996**, *403*, 169.
(292) Chen, A.; Lipkowski, J. *J. Phys. Chem. B* **1999**, *103*, 682.
(293) Härtinger, S.; Pettinger, B.; Doblhofer, K. *J. Electrochem. Soc.* **1995**, *397*, 335.
(294) Koper, M. T. M.; van Santen, R. A. *J. Electroanal. Chem.* **1999**, *472*, 126.
(295) Cruickshank, B. J.; Sneddon, D.; Gewirth, A. A. *Surf. Sci.* **1993**, *281*, L308.
(296) LaGraff, J. R.; Gewirth, A. A. In *Nanoscale probes of the solid/liquid interface*; Gewirth, A. A., Siegenthaler, H., Eds.; Kluwer Academic Publishers: Boston, 1995; pp 83−101.
(297) Coulman, D.; Wintterlin, J.; Behm, R. J.; Ertl, G. *Phys. Rev. Lett.* **1990**, *64*, 1761.
(298) Maurice, V.; Strehblow, H.-H.; Marcus, P. *Surf. Sci.* **2000**, *458*, 185.
(299) Bedürftig, K.; Völkening, S.; Wang, Y.; Wintterlin, J.; Jacobi, K.; Ertl, G. *J. Chem. Phys.* **1999**, *111*, 11147.
(300) Völkening, S.; Bedürftig, K.; Jacobi, K.; Wintterlin, J.; Ertl, G. *Phys. Rev. Lett.* **1999**, *83*, 2672.
(301) Gao, X.; Zhang, Y.; Weaver, M. J. *Langmuir* **1992**, *8*, 668.
(302) Sellers, H.; Ulman, A.; Shnidman, Y.; Eilers, J. E. *J. Am. Chem. Soc.* **1993**, *115*, 9389−9401.
(303) Gao, X.; Zhang, X. G.; Weaver, M. J. *J. Phys. Chem.* **1992**, *96*, 4156.
(304) McCarley, R. L.; Kim, Y.-T.; Bard, A. J. *J. Phys. Chem.* **1993**, *97*, 211.
(305) Andreasen, G.; Vericat, C.; Vela, M. E.; Salvarezza, R. C. *J. Chem. Phys.* **1999**, *111*, 9457.
(306) Aloisi, G. D.; Cavallini, M.; Innocenti, M.; Foresti, M. L.; Pezzatini, G.; Guidelli, R. *J. Phys. Chem. B* **1997**, *101*, 4774.
(307) Heinz, R.; Rabe, J. P. *Langmuir* **1995**, *11*, 506.
(308) Suzuki, T.; Yamada, T.; Itaya, K. *J. Phys. Chem.* **1996**, *100*, 8954.

(309) Ando, S.; Suzuki, T.; Itaya, K. *J. Electroanal. Chem.* **1996**, *412*, 139.
(310) Sung, Y.-E.; Chrzanowski, W.; Wieckowski, A.; Zolfaghari, A.; Blais, S.; Jerkiewicz, G. *Electrochim. Acta* **1998**, *44*, 1019.
(311) Sorenson, T. A.; Lister, T. E.; Huang, B. M.; Stickney, J. L. *J. Electrochem. Soc.* **1999**, *146*, 1019.
(312) Lister, T. E.; Stickney, J. L. *J. Phys. Chem.* **1996**, *100*, 19568.
(313) Stuhlmann, Ch.; Villegas, I.; Weaver, M. J. *Chem. Phys. Lett.* **1994**, *219*, 319.
(314) Stuhlmann, C. *Surf. Sci.* **1995**, *335*, 221.
(315) Inukai, J.; Morioka, Y.; Kim, Y.-G.; Yau, S.-L.; Itaya, K. *Bull. Chem. Soc. Jpn.* **1997**, *70*, 1787.
(316) Kitamura, F.; Takahashi, M.; Ito, M. *Chem. Phys. Lett.* **1986**, *130*, 181.
(317) Bagus, P. S.; Nelin, C. J.; Müller, W.; Philpott, M. R.; Seki, H. *Phys. Rev. Lett.* **1987**, *58*, 559.
(318) Frank, D. G.; Katekura, J. Y.; Rosasco, S. D.; Salaita, G. N.; Schardt, B. C.; Soriaga, M. P.; Stern, D. A.; Stickney, J. L.; Hubbard, A. T. *Langmuir* **1985**, *1*, 587.
(319) Rosasco, S. D.; Stickney, J. L.; Salaita, G. N.; Frank, D. G.; Katekura, J. Y.; Schardt, B. C.; Soriaga, M.; Stern, D. A.; Hubbard, A. T. *J. Electroanal. Chem.* **1985**, *188*, 95.
(320) Soriaga, M. *Chem. Rev.* **1990**, *90*, 771.
(321) Kim, Y.-G.; Yau, S.-L.; Itaya, K. *J. Am. Chem. Soc.* **1996**, *118*, 393.
(322) McCarley, R. L.; Bard, A. J. *J. Phys. Chem.* **1992**, *96*, 7410.
(323) Pacchioni, G.; Illas, F.; Philpott, M. R.; Bagus, P. S. *J. Chem. Phys.* **1991**, *95*, 4678.
(324) Yau, S.-L.; Kim, Y.-G.; Itaya, K. *J. Kor. Soc. Anal. Sci.* **1995**, *8*, 723.
(325) Peng, Q.; Breen, J. J. *Electrochim. Acta* **1998**, *43*, 2619.
(326) Wan, L.-J.; Yau, S.-L.; Itaya, K. *J. Solid State Electrochem.* **1997**, *1*, 45.
(327) Foord, J. S.; Reynolds, A. E. *Surf. Sci.* **1985**, *164*, 640.
(328) Clavilier, J.; Faure, R.; Guinet, G.; Durand, R. *J. Electroanal. Chem.* **1980**, *107*, 205.
(329) Clavilier, J. *J. Electroanal. Chem.* **1980**, *107*, 211.
(330) Angerstein-Kozlowska, H.; Conway, B. E. *Electrochim. Acta* **1986**, *31*, 1051.
(331) Shi, Z.; Lipkowski, J.; Gamboa, M.; Zelenay, P.; Wieckowski, A. *J. Electroanal. Chem.* **1994**, *366*, 317.
(332) Shi, Z.; Lipkowski, J.; Mirwald, S.; Pettinger, B. *J. Electroanal. Chem.* **1995**, *396*, 115.
(333) Savich, W.; Sun, S.-G.; Lipkowski, J.; Wieckowski, A. *J. Electroanal. Chem.* **1995**, *388*, 233.
(334) Zelenay, P.; Rice-Jackson, L. M.; Wieckowski, A. *J. Electroanal. Chem.* **1990**, *283*, 389.
(335) Gamboa-Aldeco, M.; Herrero, E.; Zelenay, P.; Wieckowski, A. *J. Electroanal. Chem.* **1993**, *348*, 451.
(336) Kolics, A.; Wieckowski, A. *J. Phys. Chem. B* **2001**, *105*, 2588.
(337) Uchida, H.; Ikeda, N.; Watanabe, M. *J. Electroanal. Chem.* **1997**, *424*, 5.
(338) Faguy, P. W.; Markovic, N.; Adzic, R. R.; Fierro, C. A.; Yaeger, E. B. *J. Electroanal. Chem.* **1990**, *289*, 245.
(339) Faguy, P. W.; Marinkovic, N. S.; Adzic, R. R. *Langmuir* **1996**, *12*, 243.
(340) Shingaya, Y.; Hirota, K.; Ogasawara, H.; Ito, M. *J. Electroanal. Chem.* **1996**, *409*, 103.
(341) Shingaya, Y.; Ito, M. *Electrochim. Acta* **1998**, *44*, 745.
(342) Shingaya, Y.; Ito, M. *J. Electrochem. Soc.* **1999**, *467*, 299.
(343) Edens, G. J.; Gao, X.; Weaver, M. J. *J. Electroanal. Chem.* **1994**, *375*, 357.
(344) Silva, F.; Martins, A. *J. Electroanal. Chem.* **1999**, *467*, 335.
(345) de Moraes, I. R.; Nart, F. C. *J. Electroanal. Chem.* **1999**, *461*, 110.
(346) Marinkovic, N. S.; Marinkovic, J. S.; Adzic, R. R. *J. Electroanal. Chem.* **1999**, *467*, 291.
(347) Patrito, E. M.; Paredes Olivera, P.; Sellers, H. *Surf. Sci.* **1997**, *380*, 264.
(348) Zei, M. S.; Scherson, D. A.; Lehmpfuhl, G.; Kolb, D. M. *J. Electroanal. Chem.* **1987**, *229*, 99.
(349) Nishizawa, T.; Nakaka, T.; Kinoshita, Y.; Miyashita, S.; Sazaki, G.; Komatsu, H. *Surf. Sci.* **1996**, *367*, L73.
(350) Wan, L.-J.; Yau, S.-L.; Itaya, K. *J. Phys. Chem.* **1995**, *99*, 9507.
(351) Wan, L.-J.; Hara, M.; Inukai, J.; Itaya, K. *J. Phys. Chem. B* **1999**, *103*, 6978.
(352) Wan, L.-J.; Suzuki, T.; Sashikata, K.; Okada, J.; Inukai, J.; Itaya, K. *J. Electroanal. Chem.* **2000**, *484*, 189.
(353) Funtikov, A. M.; Linke, U.; Stimming, U.; Vogel, R. *Surf. Sci.* **1995**, *324*, L343.
(354) Funtikov, A. M.; Stimming, U.; Vogel, R. *J. Electroanal. Chem.* **1997**, *428*, 147.
(355) Wilms, M.; Broekmann, P.; Stuhlmann, C.; Wandelt, K. *Surf. Sci.* **1998**, *416*, 121.
(356) Shingaya, Y.; Ito, M. *Chem. Phys. Lett.* **1996**, *256*, 438.
(357) Shingaya, Y.; Ito, M. In *Interfacial electrochemistry*; Wieckowski, A., Ed.; Marcel Dekker: New York, 1999; pp 287−300.
(358) Mrozek, P.; Han, M.; Sung, Y.-E.; Wieckowski, A. *Surf. Sci.* **1994**, *319*, 21.
(359) Thomas, S.; Sung, Y.-E.; Kim, H. S.; Wieckowski, A. *J. Phys. Chem.* **1996**, *100*, 11726.
(360) Sung, Y.-E.; Thomas, S.; Wieckowski, A. *J. Phys. Chem.* **1995**, *99*, 13513.
(361) Wilms, M.; Broekmann, P.; Kruft, M.; Park, Z.; Stuhlmann, C.; Wandelt, K. *Surf. Sci.* **1998**, *404−404*, 83.
(362) Lennartz, M.; Broekmann, P.; Arenz, M.; Stuhlmann, C.; Wandelt, K. *Surf. Sci.* **1999**, *442*, 215.
(363) Li, W.-H.; Nichols, R. J. *J. Electroanal. Chem.* **1998**, *456*, 153.
(364) Polewska, W.; Vogt, M. R.; Magnussen, O. M.; Behm, R. J. *J. Phys. Chem. B* **1999**, *103*, 10440.
(365) Randler, R. J.; Kolb, D. M., unpublished.
(366) Will, T.; Dietterle, M.; Kolb, D. M. In *Nanoscale probes of the solid/liquid interface*; Gewirth, A. A., Siegenthaler, H., Eds.; Kluwer Academic Publishers: Boston, 1995; pp 137−162.
(367) Dietterle, M.; Will, T.; Kolb, D. M. *Surf. Sci.* **1995**, *327*, L495.
(368) Smolínski, S.; Zelenay, P.; Sobkowski, J. *J. Electroanal. Chem.* **1998**, *442*, 41.
(369) Smolínski, S.; Sobkowski, J. *J. Electroanal. Chem.* **1999**, *463*, 1.
(370) Kleinert, M.; Cuesta, A.; Kibler, L. A.; Kolb, D. M. *Surf. Sci.* **1999**, *430*, L521.
(371) Cuesta, A.; Kleinert, M.; Kolb, D. M. *Phys. Chem. Chem. Phys.* **2000**, *2*, 5690.
(372) Stevenson, K. J.; Gao, X.; Hatchett, D. W.; White, H. S. *J. Electroanal. Chem.* **1998**, *447*, 43.
(373) Kolb, D. M.; Rath, D. L.; Wille, R.; Hansen, W. N. *Ber. Bunsen-Ges. Phys. Chem.* **1983**, *87*, 1108.
(374) Kolb, D. M. *Schering Lecture Vol. 2. The initial stages of metal deposition: an atomistic view*; Schering: Berlin 1991.
(375) Markovic, N.; Ross, P. N. *Langmuir* **1993**, *9*, 580.
(376) Tidswell, I. M.; Lucas, C. A.; Markovic, N.; Ross, P. N. *Phys. Rev. B* **1995**, *51*, 10205.
(377) Markovic, N.; Gasteiger, H. A.; Lucas, C. A.; Tidswell, I. M.; Ross, P. N. *Surf. Sci.* **1995**, *335*, 91.
(378) Matsumoto, H.; Oda, I.; Inukai, J.; Ito, M. *J. Electroanal. Chem.* **1993**, *356*, 275.
(379) Shi, Z.; Wu, S.; Lipkowski, J. *Electrochim. Acta* **1995**, *40*, 9.
(380) Hotlos, J.; Magnussen, O. M.; Behm, R. J. *Surf. Sci.* **1995**, *335*, 129.
(381) Möller, F.; Magnussen, O. M.; Behm, R. J. *Electrochim. Acta* **1995**, *40*, 1259.
(382) Möller, F.; Magnussen, O. M.; Behm, R. J. *Phys. Rev. B* **1995**, *51*, 2484.
(383) Magnussen, O. M.; Behm, R. J. *J. Electroanal. Chem.* **1998**, *467*, 258.
(384) Toney, M. F.; Howard, J. N.; Richer, J.; Borges, G. L.; Gordon, J. G.; Melroy, O. R. *Phys. Rev. Lett.* **1995**, *75*, 4472.
(385) Abruña, H. D.; Feliu, J. M.; Brock, J. D.; Buller, L. J.; Herrero, E.; Li, J.; Gómez, R.; Finnefrock, A. *Electrochim. Acta* **1998**, *43*, 2899.
(386) Martínez-Ruiz, A.; Valenzuela-Benavides, J.; Morales de la Garza, L.; Batina, N. *Surf. Sci.* **2001**, *476*, 139.
(387) Adzic, R. R.; Wang, J. X. *J. Phys. Chem. B* **1998**, *102*, 6305.
(388) Wang, J. X.; Robinson, I. K.; Adzic, R. R. *Surf. Sci.* **1998**, *412/413*, 374.
(389) Wang, J. X.; Robinson, I. K.; DeVilbiss, J. E.; Adzic, R. R. *J. Phys. Chem. B* **2000**, *104*, 7951.
(390) Sánchez, C. G.; Del Pópolo, M. G.; Leiva, E. P. M. *Surf. Sci.* **1999**, *421*, 59.
(391) Sánchez, C.; Leiva, E. P. M. *Electrochim. Acta* **1999**, *45*, 691.
(392) Gregory, B. W.; Stickney, J. L. *J. Electroanal. Chem.* **1991**, *300*, 543.
(393) Huang, B. M.; Colletti, L. P.; Gregory, B. W.; Anderson, J. L.; Stickney, J. L. *J. Electrochem. Soc.* **1995**, *142*, 3007.
(394) Oda, I.; Shingaya, Y.; Matsumoto, H.; Ito, M. *J. Electroanal. Chem.* **1996**, *409*, 95.
(395) Wintterlin, J.; Schuster, R.; Coulman, D.; Ertl, G.; Behm, R. J. *J. Vac. Sci. Technol. B* **1991**, *9*, 902.
(396) Ocko, B. M.; Helgesen, G.; Schardt, B. C.; Wang, J. *Phys. Rev. Lett.* **1992**, *69*, 3350.
(397) Stickney, J. L.; Villegas, I.; Ehlers, C. B. *J. Am. Chem. Soc.* **1989**, *111*, 6473.
(398) Villegas, I.; Ehlers, C. B.; Stickney, J. L. *J. Electrochem. Soc.* **1990**, *137*, 3143.
(399) Bothwell, M. E.; Cali, G. J.; Berry, G. M.; Soriaga, M. P. *Surf. Sci. Lett.* **1991**, *249*, L322.
(400) Abreu, J. B.; Barriga, R. J.; Temesghen, W.; Schimpf, J. A.; Soriaga, M. P. *J. Electroanal. Chem.* **1995**, *381*, 239.
(401) Trevor, D. J.; Chidsey, Ch. E. D.; Loiacono, S. N. *Phys. Rev. Lett.* **1989**, *62*, 929.
(402) Trevor, D. J.; Chidsey, Ch. E. D. *J. Vac. Sci. Technol. B* **1991**, *2*, 964.
(403) Nichols, R. J.; Magnussen, O. M.; Hotlos, J.; Twomey, T.; Behm, R. J.; Kolb, D. M. *J. Electroanal. Chem.* **1990**, *290*, 21.
(404) Honbo, J.; Sugawara, S.; Itaya, K. *Anal. Chem.* **1990**, *62*, 2424.
(405) Alonso, C.; Salvarezza, R. C.; Vara, J. M.; Arvia, A. J. *Electrochim. Acta* **1990**, *35*, 1331.

(406) Alonso, C.; Salvarezza, R. C.; Vara, J. M.; Arvia, A. J.; Vázquez, L.; Bartolome, A.; Baró, A. M. *J. Electrochem. Soc.* **1990**, *137*, 2161.
(407) Magnussen, O. M.; Vogt, M. R.; Scherer, J.; Behm, R. J. *Appl. Phys. A* **1998**, *66*, S447.
(408) Magnussen, O. M.; Vogt, M. R.; Scherer, J.; Lachenwitzer, A.; Behm, R. J. *Werkstoffe Korrosion* **1998**, *49*, 169.
(409) Poensgen, M.; Wolf, J. F.; Frohn, J.; Giesen, M.; Ibach, H. *Surf. Sci.* **1992**, *274*, 430.
(410) Giesen-Seibert, M.; Schmitz, F.; Jentjens, R.; Ibach, H. *Surf. Sci.* **1995**, *329*, 47.
(411) Giesen, M.; Dietterle, M.; Stapel, D.; Ibach, H.; Kolb, D. M. *Surf. Sci.* **1997**, *384*, 168.
(412) Giesen, M.; Dietterle, M.; Stapel, D.; Ibach, H.; Kolb, D. M. *Mater. Res. Soc. Symp. Proc.* **1997**, *451*, 9.
(413) McHardy, R.; Haiss, W. H.; Nichols, R. J. *Phys. Chem. Chem. Phys.* **2000**, *2*, 1439.
(414) Giesen, M.; Kolb, D. M. *Surf. Sci.* **2001**, *468*, 149.
(415) Baier, S.; Giesen, M. *Phys. Chem. Chem. Phys.* **2000**, *2*, 3675.
(416) Baiers, S.; Giesen, M. *Phys. Chem. Chem. Phys.* **2000**, *2*, 3675.
(417) Giesen, M. *Prog. Surf. Sci.* **2001**, 68, 1.
(418) Wu, Q., Barkey, D. In *Electrochemical Processing in ULSI Fabrication and Semiconductor/Metal Deposition II.*; Andricacos, P. C., Searson, P. C., Reidsema-Simpson, C., Allongue, P., Stickney, J. L., OleszeK, G. M., Eds.; The Electrochemical Society: Pennington, 1999; *Proc. Electrochem. Soc.* 99−9, pp 134−148.
(419) Wu, Q.; Barkey, D. *J. Electrochem. Soc.* **2000**, *147*, 1038.
(420) Vogt, M. R. Ph.D. Thesis, University Ulm, 1998.
(421) King, R. T.; Mullins, W. W. *Acta Metallurgica* **1962**, *10*, 601.
(422) Zitzler, L.; Gleich, B.; Magnussen, O. M.; Behm, R. J. In *Localized In Situ Methods for Investigating Electrochemical Interfaces*; Hillier, A. C., Seo, M., Taylor, S. R., Eds.; The Electrochemical Society: Pennnigton, 2000; *Proc. Electrochem. Soc.* 99−28, p 38.
(423) Magnussen, O. M.; Zitzler, L.; Gleich, B.; Vogt, M. R.; Behm, R. J. *Electrochim. Acta* **2001**, *46*, 3725.
(424) Stranski, I. N. *Z. phys. Chem.* **1928**, *136*, 259.
(425) Budevski, E.; Staikov, G.; Lorenz, W. J. *Electrochemical phase formation and growth*; VCH: Weinheim, 1996.
(426) Magnussen, O. M.; Vogt, M. R. *Phys. Rev. Lett.* **2000**, *84*, 357.
(427) Nakakura, C. Y.; Altman, E. I. *J. Vac. Sci. Technol. A* **1998**, *16*, 1566.
(428) Ye, S.; Ishibashi, C.; Uosaki, K. *Langmuir* **1999**, *15*, 807.
(429) Brisard, G.; Betrand, N.; Ross, P. N.; Markovic, N. M. *J. Electroanal. Chem.* **2000**, *480*, 219.
(430) Vogt, M. R.; Polewska, W.; Magnussen, O. M.; Behm, R. J. *J. Electrochem. Soc.* **1997**, *144*, L113.
(431) Vogt, M. R.; Nichols, R. J.; Magnussen, O. M.; Behm, R. J. *J. Phys. Chem. B* **1998**, *102*, 5859.
(432) Vogt, M. R.; Magnussen, O. M.; Behm, R. J. In *Critical factors in localized corrosion III.*; Kelly, R. G., Frankel, G. S., Natishan, P. M., Newman, R. C., Eds.; The Electrochemical Society: Pennington, 1999; *Proc. Electrochem. Soc.* 98−17, pp 591−618.
(433) Kunitake, M.; Batina, N.; Itaya, K. *Langmuir* **1995**, *11*, 2337.
(434) Batina, N.; Kunitake, M.; Itaya, K. *J. Electroanal. Chem.* **1996**, *405*, 245.
(435) Ogaki, K.; Batina, N.; Kunitake, M.; Itaya, K. *J. Phys. Chem.* **1996**, *100*, 7185.
(436) Itaya, K.; Batina, N.; Kunitake, M.; Ogaki, K.; Kim, Y.-G.; Wan, L.-J.; Yamada, T. In *Solid−Liquid Electrochemical Interfaces*; Jerkiewicz, G., Wieckowski, A., Uosaki, K., Soriaga, M., Eds.; American Chemical Society: Washington, DC, 1997; pp 171−188.
(437) Kunitake, M.; Akiba, U.; Batina, N.; Itaya, K. *Langmuir* **1997**, *13*, 1607.
(438) Sashikata, K.; Sugata, T.; Sugimasa, M.; Itaya, K. *Langmuir* **1998**, *14*, 2896.
(439) Wakabayashi, N.; Kitamura, F.; Ohsaka, T.; Tokuda, K. *J. Electroanal. Chem.* **2001**, *499*, 161.
(440) Casagrande, M.; Lacombe, S.; Guillemot, L.; Esaulov, V. A. *Surf. Sci.* **2000**, *445*, L29.

CR000069P